eXPRESS Polymer Letters Vol.6, No.6 (2012) 437
Available online at www.expresspolymlett.com
DOI: 10.3144/expresspolymlett.2012.46

Editorial corner – a personal view

Graphene and its derivatives: Novel materials for forming functional polymer nanocomposites

S. C. Tjong[*]

Department of Physics and Materials Science, City University of Hong Kong, Tat Chee Avenue, Kowloon, Hong Kong

Expanded graphite (EG) and graphite nanoplatelets (GNPs) have been widely used as nanofillers to enhance electrical conductivity and mechanical properties of polymers. EGs with a thickness of ~50 to 400 nm were synthesized from graphite intercalation compounds followed by rapid heating. However, the graphene sheets of EGs are partially separated. EGs can be exfoliated to GNPs with a thickness of less than 10 nm under sonication in solvents. The EG/polymer and GNP/polymer nanocomposites show potential applications as the structural components of fuel cells, electromagnetic interference shielding materials, conducting materials for chemical sensors, etc. The physical and mechanical performances of polymers can be further improved by adding very low loading level of graphene of large aspect ratios.

Graphene, a single atomic layer of carbon atoms that are covalently bonded in a honeycomb crystal lattice, is widely known as a basic building block for carbonaceous materials. The remarkable achievement of graphene monolayer through mechanical exfoliation of graphite by Geim and Novoselov in 2004 has sparked tremendous research interest relating to its properties and applications. Because of its extraordinary electrical, mechanical, optical and thermal characteristics, graphene is an ideal filler material for the polymers to form functional nanocomposites. However, the yield of mechanically exfoliated graphene is very low, and can only be used for general property characterization. The successful synthesis of graphene oxide (GO) via chemical oxidation of graphite opens up new opportunities for fabricating high performance-polymer nanocomposites with excellent biological, mechanical and physical properties. GO is an electrical insulator since it contains oxygenated functional groups. To resume its electrical conductivity, chemical reducing agent addition or thermal treatment is needed to remove such functional groups. Enhanced electrical conductivity can be achieved in thermoplastics by adding ultra-low reduced graphene oxide of ~0.07–0.1 vol%. Thermally reduced graphene oxides with wrinkled morphology, high aspect ratio, and extraordinary high strength are more effective than carbon nanotubes to reinforce and toughen epoxy and glassy polymers. Finally, graphene and its derivatives have been reported to exhibit good biocompatibility with human cells. Carbon nanotubes generally contain metal catalysts that may induce cytotoxicity and inflammation. Metal catalysts are not needed for the synthesis of graphene, thereby avoiding cytoxicity and inflammation issues.

Prof. Dr. Sie Chin Tjong
Member of International Advisory Board

---

[*] Corresponding author, e-mail: APTJONG@cityu.edu.hk

eXPRESS Polymer Letters Vol.6, No.6 (2012) 438–453
Available online at www.expresspolymlett.com
DOI: 10.3144/expresspolymlett.2012.47

Superposition approach for description of electrical conductivity in sheared MWNT/polycarbonate melts

M. Saphiannikova[1*], T. Skipa[2], D. Lellinger[2], I. Alig[2], G. Heinrich[1,3]

[1]Leibniz-Institut für Polymerforschung Dresden e.V., Hohe Straße 6, D-01069 Dresden, Germany
[2]Deutsches Kunststoff Institut, Schlossgartenstraße 6, D-64289 Darmstadt, Germany
[3]Technische Universität Dresden, Institut für Werkstoffwissenschaft, Helmholtzstrasse 7, D-01069 Dresden, Germany

Received 10 October 2011; accepted in revised form 20 December 2011

Abstract. The theoretical description of electrical properties of polymer melts, filled with attractively interacting conductive particles, represents a great challenge. Such filler particles tend to build a network-like structure which is very fragile and can be easily broken in a shear flow with shear rates of about 1 s^{-1}. In this study, measured shear-induced changes in electrical conductivity of polymer composites are described using a superposition approach, in which the filler particles are separated into a highly conductive percolating and low conductive non-percolating phases. The latter is represented by separated well-dispersed filler particles. It is assumed that these phases determine the effective electrical properties of composites through a type of mixing rule involving the phase volume fractions. The conductivity of the percolating phase is described with the help of classical percolation theory, while the conductivity of non-percolating phase is given by the matrix conductivity enhanced by the presence of separate filler particles. The percolation theory is coupled with a kinetic equation for a scalar structural parameter which describes the current state of filler network under particular flow conditions. The superposition approach is applied to transient shear experiments carried out on polycarbonate composites filled with multi-wall carbon nanotubes.

Keywords: *nanocomposites, multi-wall carbon nanotubes, electrical conductivity, shear flow, modeling*

---

1. Introduction

Polymer nanocomposites, filled with attractively interacting conductive anisometric particles such as carbon nanotubes (CNT), graphite nano-platelets or graphenes, are not only in the focus of industrial interest due to numerous possible applications but also draw serious attention from academic research as new functional materials having unique physical properties. So, it is well-known that a minute amount of CNT additive can turn an electrically insulating polymer material into a conductive composite [1–4]. On the other hand, addition of CNT fillers can lead to a noticeable mechanical reinforcement [5, 6]. The high conductivity in CNT-based composite materials can be ascribed to the formation of the percolation network of interconnected filler particles which may transfer electric current, as well as mechanical stress [7–9]. As discussed in literature [10, 11] very small inter-particle distances (~few nm) are needed for low contact resistance and efficient electron transport through the conductive filler network. Therefore, it is not surprising that the percolation network is found to be very fragile, as it can be easily broken under steady shear flow with shear rates of about 1 s^{-1} [12, 13]. The shear-induced rupture of filler network represents currently a main obstacle to the widespread introduction of CNT-based polymer nanocomposite products into everyday life. This is because the dominating industrial process for their production is the melt processing

---

[*]Corresponding author, e-mail: grenzer@ipfdd.de

of polymers via extrusion or injection moulding, both processes being characterized by extremely high shear rates. To overcome this impediment, it is necessary to understand and to learn to predict transient electric properties of the sheared polymer nanocomposites. This task is important for industrial applications and very interesting and challenging from the theoretical point of view.

Electrical properties of polymer nanocomposites, filled with attractively interacting conductive anisometric particles, strongly depend on the morphology of filler network [14, 15] as well as on the orientation state of individual particles [16, 17]. Therefore, one finds in literature two different approaches for the modelling of the electric properties of those composites. The first approach considers composites in which anisometric conductive particles are randomly distributed in a slightly conducting matrix. Assuming that filler particles do not interact with each other, it is possible to derive the effective electrical conductivity tensor if the second order orientation tensor is known [18]. One of the advantages of this approach is that it naturally accounts for the time evolution of anisotropic conductivity if the time dependence of orientation tensor can be determined (for example by the Folgar-Tucker equation [19, 20]).

The second approach considers composites in which conductive fillers are randomly distributed (and randomly oriented if anisometric) in a non-conducting matrix. The insulator-to-conductor transition in such systems is induced by the formation of a percolation path, once the filler content has reached a threshold critical value [21, 22]. Several percolation models generally applicable to isotropic conductive systems have been elaborated: the Swiss Cheese (random void) model and its extensions [23–25], the nodes-links-blobs model [26, 27], Stinchcombe theory on a Bethe lattice [28]. As percolation models are static ones, they are only applicable to homogeneous systems with statistically distributed filler in the equilibrium state. An anisotropic generalization of the Stinchcombe's approach [28], proposed recently by Semeriyanov *et al*. [29], aims at the description of percolation networks with anisotropic local conductivity represented by resistors with direction-dependent electrical conductivity. Such anisotropy may arise for example from strong shearing of the filler network built from elongated conductive particles. Similar to other percolation theories, this newest approach lacks information on time – and shear-dependence of resistor conductivity.

A very promising numerical approach to the electrical conductivity of static and sheared CNT/polymer suspensions has been reported recently by Eken *et al*. [30, 31]. Composite microstructures were generated using a fiber-level simulation method, in which monodisperse fibers (carbon nanotubes) are modeled as a sequence of connected rigid cylinders. The values of electrical conductivity can be determined from generated microstructures using a resistor network algorithm. It has been shown that if a weak shear flow is applied to a viscous fiber suspension, the electric percolation threshold decreases due to shear-induced formation of conductive aggregates [30]. Increasing shear rate has a negative effect on conductive network formation: when shear rate exceeds a critical value the electrical conductivity was found to decrease to the matrix conductivity [31]. For lack of transient percolation theories, we proposed recently a phenomenological approach, in which time and shear-dependence of electrical conductivity is accounted for by coupling percolation theory with an appropriate kinetic equation for build-up and destruction of conductive agglomerates [12, 13]. To our knowledge, agglomeration of nanoparticles in a polymer matrix was first discussed by Schueler *et al.* [32, 33] for carbon black in uncured epoxy. Heinrich *et al.* [34] proposed agglomeration of layered nanofillers in a thermoplastic or rubber matrix along with a kinetic equation for description of the time evolution of the shear modulus. In our first simplified approach [12, 13] we assumed, that the 'percolation' path is formed by sphere-like conductive agglomerates, containing loosely packed CNTs. These agglomerates can be formed or destroyed in shear flow [35, 36]. For steady shear conditions constant values for the electrical conductivity and the dynamic shear modulus were found, indicating a stationary state of the filler network due to the competition of shear-induced build up and destruction [35, 36]. In the quiescent state of melt the destroyed agglomerates were found earlier to be rebuilt in the process of quiescent agglomeration [12–15]. As stated already in [36], for a more realistic description of the filler network and its dependence on the thermo-rheological history a 'superstructure' has to be taken into account, e.g. a distribution of agglomerate sizes or a spinodal-type superstructure. In particular, for description of the time-dependent electrical conductivity a hierarchical model [36] assuming different types of agglomerated has been used to fit the experimental data. In the previous studies [36–38] the coupling approach has been tested using either the classical percolation theory [39] or the Generalized Effective Medium (GEM) approximation [40].

Here we present a different superposition approach in which the filler particles are assumed to be separated into percolating and non-percolating phases. In terms of our previous works, the percolating phase can be understood as an 'agglomerate-rich' or as a conductive phase in 'spinodal decomposition'. The conductivity of the percolating phase is described with the help of a coupling approach based on the classic percolation theory. Additionally, we take into account the enhancement of matrix conductivity by the presence of separate filler particles composing the non-percolating phase. For the sake of simplicity, it is assumed that the particles are oriented randomly. This is valid at least for moderate shear rates, less than 10^3 s^{-1} (see e.g. [12, 13, 41]). The superposition approach is tested on polycarbonate composites filled with multi-walled CNTs at different temperatures. Filler amounts are chosen to be quite close to the percolation threshold, where the effect of shear-induced rupture of filler network is well pronounced [37].

2. Experimental

Polycarbonate, Macrolon® type 2600, was produced by Bayer Material Science AG, Germany. The polymer is of linear structure and amorphous according to the manufacturer specification. The multi-walled carbon nanotubes used in this study were Baytubes® from Bayer Material Science AG with max. 5% inorganic impurities. The mean outer diameter is of about 13–16 nm and the tube length varies between 1 and 10 μm.

The MWNT-polycarbonate samples [37] were provided by Bayer Technology Sevice GmbH Leverkusen, Germany. The compounds were produced by melt-mixing in a twin screw extruder (ZSK 26 MC from Coperion Werner & Pfleiderer, Stuttgart, Germany) in one processing step. Both, the polycarbonate and the MWNTs were fed into the main feeder of the extruder. After compounding, the MWNT-polycarbonate composites were cooled down in a water bath and were finally granulated with a pelletizer. The granulates were used to prepare disk-shaped CNT-polycarbonate plates with a diameter of 80 mm and a thickness of 2 mm by injection molding technique at the Thermoplastic Testing Center of Bayer Material Science AG, Leverkusen, Germany. During the injection molding the melt temperature was held at 340°C, the mold temperature was held at 120°C. The flow rate during the filling process was set to approximately 5 cm^3/s.

For the conductivity measurements round samples of 25 mm diameter and of 2 mm thickness were cut from the mould injected plates. The time-dependent dielectric measurements were performed using a Novocontrol impedance analyser coupled with a laboratory rheometer (Ares, Rheometric Scientific), in which the rheometer plates are equipped with ring electrodes (inner diameter 19 mm, outer diameter 25 mm) [12, 13, 35, 36]. The setup with ring electrodes ensures a relatively narrow distribution of the shear rates in the relevant region of electrical field during steady rotation. In the present study a tangential steady shear was applied to the melt by rotating the lower rheometer plate. The electrical conductivity was measured perpendicular to the direction of applied shear. This allowed monitoring of the electrical conductivity in the volume between the two ring electrodes. The conductivity measurements were performed at a single frequency of 1 kHz, which is considered to be representative for the DC conductivity [12]. The rheometer is equipped with an oven which maintained stable temperature of the composite melt during the measurements.

3. Model description

3.1. Electrical conductivity

To describe shear-induced changes in the electrical conductivity of a polymer melt filled with attractively interacting conductive particles, we propose to use a superposition approach similar to that applied by us recently for description of viscoelastic properties of the same nanocomposite system [42]. In the framework of superposition approach we assume that the filler particles can be divided into the percolating and non-percolating phases (see Figure 1).

The percolating phase (network) consists of a group of clusters that are not very far from each other.

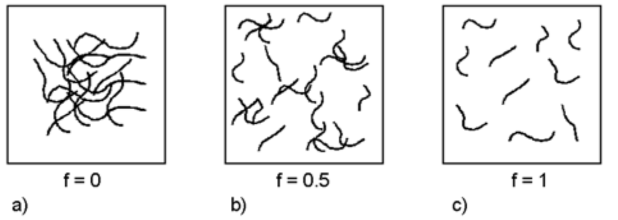

Figure 1. Schematic representation of the time-evolution of filler structure in strong shear flow: (a) initial undestroyed state; (b) intermediate two-phase state, in which the percolating phase is represented by the connected filler clusters and the non-percolating phase by separate well-dispersed particles; (c) final destroyed state, in which all particles are well-dispersed and not connected with one another. Also are shown corresponding values of the parameter *f*, describing the fraction of free nanotubes.

Shear reduces the number of nanotubes in the percolating phase by rupture of nanotubes from the clusters, breaking large clusters into smaller ones and by distributing the clusters evenly in space. All these processes are effectively reducing the fraction of nanotubes that belong to the clusters initially forming a conducting path. The total electrical conductivity, σ, can be then represented as a sum of two terms (Equation (1)):

$$\sigma = X(f)\sigma_{\mathrm{M}}(T) + \sigma_{\mathrm{Net}}(T,f) \tag{1}$$

where $\sigma_{\mathrm{M}}(T)$ is the temperature-dependent matrix conductivity and $\sigma_{\mathrm{Net}}(T, f)$ is the conductivity of percolating phase (network); it is equal to zero, if the system is below the electric percolation threshold. A parallel connection of the matrix and percolating network conductivities as described by Equation (1) insures high values of nanocomposite conductivity σ above the percolation threshold. Contrary, a connection 'in series' would result in very low values of σ comparable with the value of matrix conductivity σ_{M}. In Equation (1) f is the fraction of free nanotubes, i.e. of nanotubes not belonging to the percolating phase, and, correspondingly, $1-f$ describes the fraction of nanotubes in the percolating phase.

A quite similar superposition approach to the electrical conductivity of CNT/polymer composites has been proposed in the studies of Bruck and co-workers [43, 44]. The total electrical conductivity of MWNT/polystyrene composites in these studies was represented as a sum of two terms: the temperature-independent polystyrene conductivity and the conductivity of percolating phase described by a conventional power-law relationship. To model the conductivity increase due to thermal annealing [44], the authors assumed that the effective volume fraction of percolated particles increases with annealing time according to a stretched exponential law, in which the characteristic relaxation time is assumed to obey the Arrhenius temperature dependence. The main difference between the approach of Bruck and co-workers [43, 44] and our approach is that the first approach neglects the contribution of non-percolating particles to the total composite conductivity, while we take this contribution explicitly into account by considering a reinforced matrix conductivity described by the first term on the right side of Equation (1). Besides, there is no shear dependence of the effective volume fraction of percolated particles in the first superposition approach, as the authors have only considered the effect of thermal annealing on the composite conductivity [44]. In our study the time evolution of the fraction of percolated nanotubes due to shearing is taken explicitly into account by introducing an appropriate kinetic equation (see section 3.2).

The electric enhancement factor, X, in Equation (1) can be calculated for the case of strong contrast, i.e. when the particle conductivity is considerably larger than the polymer conductivity, according to the Equation (2) [18]:

$$X(f) = 1 + \frac{1+3L}{3L(1-L)} f\varphi \tag{2}$$

Here φ is the volume fraction of particles (here CNTs), $f\varphi$ is the volume fraction of free particles and $L = \ln r/r^2$ is the depolarization factor defined by the aspect ratio of rigid conductive particle, r. Equation (2) has been obtained from a general expression for the effective electrical conductivity tensor (see Equation (12) in ref. [18]) of composites with rod-like conductive inclusions in a slightly conductive matrix. This expression is valid at sufficiently low volume fractions of nanoparticles, when they do not yet percolate. In the case of random orientation distribution of rod-like inclusions one obtains the isotropic conductivity of composite which is proportional to the isotropic matrix conductivity with the coefficient of proportionality given by Equation (2).

Fitting the viscoelastic data for the same MWNT-polycarbonate composite, we found that the average aspect ratio of the multi-wall carbon nanotubes is about 40 [42]. This value roughly corresponds to the ratio of the Kuhn segment length, reported for the carbon nanotubes to be about 1 μm [45], to the nanotube diameter (13–16 nm). This gives the depolarization factor $L = 2\cdot10^{-3} \ll 1$, and thus Equation (2) can be reduced to Equation (3):

$$X(f) = 1 + \frac{1}{3L} f \varphi \tag{3}$$

The electrical conductivity of polycarbonate matrix is an ionic type of conductivity and thus strongly increases with temperature. We found that it obeys the Arrhenius law in the region of melt temperatures between 200 and 260°C (see Figure 2a) (Equation (4)):

$$\sigma_\mathrm{M}(T) = \sigma_\mathrm{M}^0 \exp\left(-\frac{E_\mathrm{a}}{k_\mathrm{B}T}\right) \tag{4}$$

with $\sigma_\mathrm{M}^0 = 5.78\cdot10^2$ S/m and $E_\mathrm{a} = 1.88\cdot10^{-19}$ J. In Equation (4) T is the absolute temperature, $k_\mathrm{B} = 1.381\cdot10^{-23}$ J/K is the Boltzmann constant. This gives $\sigma_\mathrm{M} = 10^{-9}$ S/m at 230°C and $\sigma_\mathrm{M} = 1.29\cdot10^{-7}$ S/m at 340°C.

The conductivity of percolating network (phase) in Equation (1) is described by a classical percolation equation (Equation (5)):

$$\sigma_\mathrm{Net} = \begin{cases} 0 & p \le p_\mathrm{c} \\ \sigma_\mathrm{f}(T)\left(\dfrac{p - p_\mathrm{c}}{1 - p_\mathrm{c}}\right)^\mathrm{t} & p > p_\mathrm{c} \end{cases} \tag{5}$$

where p is the probability of bond occupation by electrical resistors and p_c is the percolation threshold, at which a cluster (connected group of occupied bonds) spans the whole system. The percolation threshold is a nonuniversal quantity that depends on the space dimension, lattice structure and other microscopic details, e.g. interactions [46, 47]. The conductivity critical exponent t is taken to be equal 2 which is a typical value for three dimensional systems [39]. This value has been found for melt processed MWNT-polycarbonate composites [2]. The conductivity of perfect network, σ_f, i.e. the value of σ_Net at $p = 1$ in Equation (5), has been extracted from the equilibrium values of electrical conductivity (i.e. in the absence of shear) for a series of samples with the weight fraction of carbon nanotubes $\Phi = 1$ wt%. It has been found that σ_f is temperature-dependent and obeying as well an Arrhenius law in the region of melt temperatures between 200 and 295°C (see Figure 2b) (Equation (6)):

$$\sigma_\mathrm{f}(T) = \sigma_\mathrm{f}^0(T) \exp\left(-\frac{E_\mathrm{a}}{k_\mathrm{B}T}\right) \tag{6}$$

with $E_\mathrm{a} = 6.76\cdot10^{-20}$ J and $\sigma_\mathrm{f}^0 = 5.53\cdot10^7$ S/m. This gives $\sigma_\mathrm{f} = 3.25\cdot10^3$ S/m at 230°C and $\sigma_\mathrm{f} = 1.87\cdot10^4$ S/m at 340°C. Arrhenius dependence in Equation (6) points on hopping mechanism of electric conductivity.

3.2. Kinetic equation

It is assumed that the percolating structure is stabilized by a number of physical bonds that can be broken (or built up) by shearing in a nonlinear regime and can be again re-built during the quiescent time. In our case these physical bonds represent effective attractive interactions between the multi-wall carbon nanotubes. As the total number

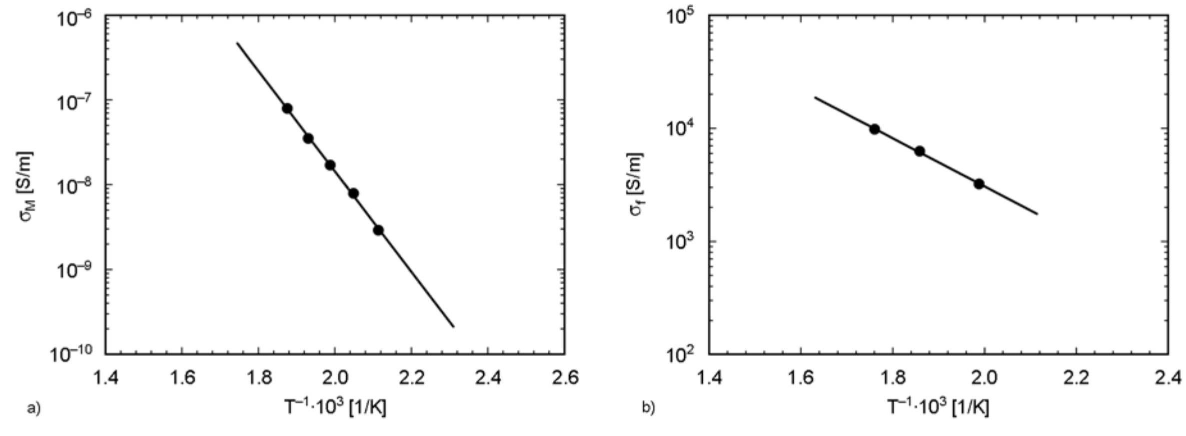

Figure 2. Temperature dependence of the matrix conductivity σ_M (a), of the conductivity of perfect network σ_f (b).

of particles – bound ones in the percolating phase and free ones in the non-percolating phase – is not changing, a usual kinetic equation can be written for the change of the fraction of free nanotubes f (Equation (7a)):

$$\frac{\mathrm{d}f}{\mathrm{d}t} = a\eta(T,\dot{\gamma}_0)\,\dot{\gamma}_0^{\mathrm{m}}(1-f) - b_1\dot{\gamma}_0^{\mathrm{n}}f - b_2 f, \quad 0 \le f \le 1 \tag{7a}$$

The first (breakage) term on the right side of this equation describes the breakdown of percolation network in a flow with the shear rate $\dot{\gamma}_0$, while the second (shear-induced build-up) term takes into account possible shear-induced agglomeration effects [48]. The last (recovery) term in Equation (7a) describes a structure build-up driven by attractive interactions between the multi-wall carbon nanotubes in the absence of shear flow. If originally the nanotubes were well dispersed in the polymer matrix, the process of agglomeration in the absence of shear takes a very long time with the rate constant $b_2 \sim 10^{-6}$ s^{-1} [35, 36]. The presence of steady shear deformation, as it was found recently by us [35, 36], facilitates the structure build-up considerably. For shear rates of $\dot{\gamma}_0 \le 0.01$ s^{-1} the values of $b = b_1\dot{\gamma}_0^{\mathrm{n}} + b_2 \sim 10^{-3}$ s^{-1} were found. Equation (7a) has been tried first to fit the data on stationary and transient electrical conductivity at shear rates up to 1 s^{-1}. It has been found that good fits can be already obtained, if the value b is taken to be shear-rate independent $b \neq b(\dot{\gamma}_0)$. Therefore, in our further considerations we will refer to a simplified version of the kinetic Equation (7a) (Equation (7b)):

$$\frac{\mathrm{d}f}{\mathrm{d}t} = a\eta(T,\dot{\gamma}_0)\,\dot{\gamma}_0^{\mathrm{m}}(1-f) - bf, \quad 0 \le f \le 1 \tag{7b}$$

keeping in mind that the effective rate constant b in Equation (7b) describes a joint action of the shear flow and of the attractive interactions between carbon nanotubes on their agglomeration.

Electrical conductivity of the sheared MWNT/polycarbonate melts, as will be shown below, depends strongly on the experimental temperature. This agrees with other studies, in which higher conductivity values have been found for processes involving high temperatures [15, 44, 49]. These correspond to smaller values of the polymer viscosity and thus smaller values of the shear forces acting on the particle aggregates. Assuming the Arrhenius dependence of the zero-shear polyurethane (TPU) viscosity, Bilotti *et al.* [49] managed to transform time dependences of the CNT/TPU composite conductivities measured at temperatures well above the glass transition temperature on a kind of master curve at times larger than 10 s. The rate of conductivity change was assumed to be inverse proportional to the viscosity of polymer.

To account for the temperature effect in the present study, we propose to introduce into the breakage term on the right side of Equation (7b) a temperature- and shear-dependent matrix viscosity $\eta(T,\dot{\gamma}_0)$ described by the Carreau-WLF model [50] (Equation (8)):

$$\eta(T,\dot{\gamma}_0) = \eta_0\frac{c_{\mathrm{T}}}{(1 + c_{\mathrm{T}}t_1\dot{\gamma}_0)^{\mathrm{n}}} \tag{8}$$

The polycarbonate F used in this study has $\eta =$ 548 Pa·s, $t_1 = 8.8\cdot10^{-4}$ s, the shear-thinning exponent $n = 0.79$ and the temperature-dependent parameter c_{T} given by the Equation (9):

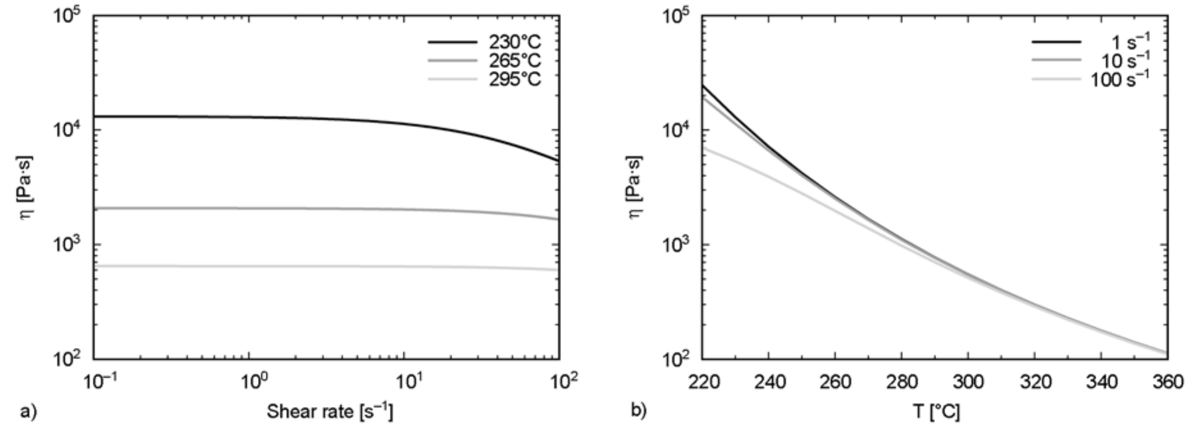

Figure 3. a) Shear dependence of the polycarbonate viscosity at three different temperatures. b) Temperature dependences of the polycarbonate viscosity at three different shear rates.

$$\log_{10} c_T = \frac{c_1(T_b - T_s)}{c_2 + (T_b - T_s)} - \frac{c_1(T - T_s)}{c_2 + (T - T_s)} \tag{9}$$

where $T_b = 300°C$, $T_s = 150°C$, $c_1 = 8.86$ and $c_2 = 101.6°C$. As can be seen from Figure 3a, the shear viscosity of the polycarbonate melt as described by Equation (8) stays nearly constant for shear rates less than $\dot{\gamma}_{cr} \sim 10\ s^{-1}$. This means that at the laboratory conditions, when shear rates do not exceed 1 s^{-1}, one can neglect the shear-thinning effect, $\eta(T,\dot{\gamma}_0) = \eta(T)$. Upon heating the sample from 220 till 320°C the polycarbonate viscosity decreases by nearly two orders of magnitude for shear rates below $\dot{\gamma}_{cr}$ (Figure 3b). At higher shear rates decrease of the viscosity is smaller due to the shear-thinning effect.

3.3. Coupling part

To introduce the time and shear dependence into Equation (5) for the electrical conductivity of percolating network, one needs to correlate the occupation probability of network bonds p and the percolation threshold p_c with such material parameters as the fraction of (all) particles and the fraction of free particles. It is clear that in the absence of shear flow the initial occupation probability, p_{in}, should be correlated with the weight fraction of carbon nanotubes, Φ. In our previous rescaling approach, based on the idea of percolation of sphere-like nanotube agglomerates [35–37], the weight fraction of nanotubes has been rescaled to the initial percolation probability, p_A, of the agglomerates. In the present study we assume two phases, where the 'conductive phase' undergoes an intrinsic percolation threshold, whereas the non-percolating phase composed from separate nanotubes slightly enhances the matrix conductivity. In terms of our previous works, the percolating phase can be considered as a conductive superstructure formed by the agglomerates (e.g. hierarchy of different agglomerates sizes or 'spinodal structure'). For the sake of simplicity, we will restrict here from the use of rescaling approach assuming instead that the initial occupation probability is equal to the volume fraction of carbon nanotubes, φ. It can be calculated from the weight fraction Φ as (Equation (10)):

$$p_{in} \equiv \varphi = \frac{\rho_{PC}\Phi}{\rho_{PC}\Phi + \rho_{NT}(1 - \Phi)} \tag{10}$$

In Equation (10) $\rho_{PC} = 1.2\ g/cm^3$ is the density of polycarbonate and $\rho_{NT} = 2.0\ g/cm^3$ is the MWNT density. This gives $p_{in} = 0.006$ for $\Phi = 1$ wt%. This sample as well as the sample with $p_{in} = 0.004$ ($\Phi = 0.75$ wt%) are still highly conductive in the absence of shear. Hence, the percolation threshold for the system under study should lie below 0.004. If one remembers that the carbon nanotubes are similar to semi-flexible chains, then the percolation threshold can be estimated using the Equation (11) [45]:

$$p_c \equiv \varphi_c \sim d^{7/5} \cdot l_p^{-3/5} \cdot L^{-4/5} \tag{11}$$

where $d \approx 15$ nm is the nanotube diameter, $l_p \sim 0.5\ \mu m$ and $L = 5\ \mu m$ are nanotube persistence and contour length, correspondingly. Equation (11) provides an estimate of $p_c \sim 0.001$ which will be used in the following.

Now, we are able to couple the electrical conductivity of the percolating phase described by Equation (5) and the kinetic changes in the fraction of free nanotubes given by Equation (7b). Let us first consider the case when the percolating phase is totally destroyed by strong shearing and all nanotubes become free (unconnected). This case corresponds to the values of occupation probability $p = p_c$ and fraction of free particles $f = 1$. Contrary, in the case of fully recovered sample all nanotubes belong to the percolating phase: $p = p_{in}$ and $f = 0$. To describe the time- and shear- dependent transition between these two cases, it is natural to introduce a new variable $\Delta p = p - p_c$, that defines a distance from the percolation threshold:

$$\Delta p = \Delta p_{max}(1 - f) \quad \text{with} \quad \Delta p_{max} = p_{in} - p_c. \tag{12}$$

Equation (12) together with Equations (1) and (2) implies that initially, in the absence of shear when $f = 0$, all carbon nanotubes are in the percolating phase. Hence, the total nanocomposite conductivity is mainly defined by the conductivity of percolating network as in this case the matrix conductivity has a negligible contribution into the total conductivity. Contrary, in the presence of very strong shear when $f \to 1$ all carbon nanotubes are well dispersed in a polymer matrix and the nanocomposite conductivity is defined by the matrix conductivity slightly enhanced by the presence of conductive particles.

Using Equation (12), we can rewrite Equation (5) in terms of the shear- or process-dependent parameter f (Equation (13)):

$$\sigma_{\mathrm{Net}} = \sigma_{\mathrm{f}}(T)\,\Delta p_{\mathrm{max}}^{2}\left(\frac{1-f}{1-p_{\mathrm{c}}}\right)^{2} \tag{13}$$

Equations (12) and (13) presume that the percolation concentration is proportional to the fraction of 'unfree' $1-f$ particles given by the kinetic Equation (7b). Hence, the percolation probability is not anymore constant but depends on the history of shear application. Other hidden presumptions of present approach are that the particles in the percolation phase are statistically distributed and randomly oriented. The latter presumption is justified by the transmission electron microscopy investigations showing that CNTs agglomerate in the thermoplastic matrix into the sphere-like clusters [13, 15] which can be hardly oriented by the flow. Thus, strong shear first causes destruction of the filler agglomerates which can be possibly followed by an orientation of the individual anisometric filler particles [16]; the latter process is not considered here.

4. Results and discussion

In order to investigate how the shear flow affects the electrical conductivity, a number of similar samples were cut out from mould injected plates. All samples were first pre-treated thermo-mechanically (by the procedure reported in [36]) to obtain a well-defined initial state with a high level of electrical conductivity. This initial state corresponds to 'well-agglomerated' multi-wall carbon nanotubes, i.e. the initial value of fraction of free nanotubes, f_0, is about zero. Different shear rates varying from 0.02 to 1 rad/s were applied to pre-treated samples. Figure 4a shows typical results measured at $T = 265°\mathrm{C}$ for a series of samples with $\Phi = 0.75$ wt%. It can be seen that at all shear rates the electrical conductivity after initial monotonic decrease reaches a steady state value for sufficient duration of the shear deformation (stationary plateau). The steady-state values of electrical conductivity, σ_{st}, were taken at 600 s and then plotted versus shear rate, a corresponding curve is shown in Figure 4b. As can be seen the electrical conductivity of MWNT/polycarbonate melts exhibits a pronounced 'shear-thinning' effect, similar to that observed for shear viscosity of polymer melts in the nonlinear regime of shearing.

It has been shown by Kharchenko *et al*. [51] and by us [36] that the shear thinning of electrical conductivity can be fitted by the Carreau equation [52] or a similar Equation (14):

$$\sigma = \frac{\sigma_{\mathrm{eq}}}{(1 + t_1\dot{\gamma}_0)^{\mathrm{m}_\sigma}} \tag{14}$$

where σ_{eq} is the equilibrium value of electrical conductivity, m_σ is the shear-thinning conductivity exponent and t_1 is the time constant. The shear thinning exponents for conductivity were found to be 0.66 [51] and 2 [36]. However, only one series of samples with a certain wt% of MWNTs and at one chosen melt temperature has been measured in the previous studies. So, it is not clear a priory, whether the shear-thinning curves measured for different weight fractions and at different temperatures are characterized by different values of the shear-shinning conductivity exponent or a single one. If the latter case is true, it will open an opportunity to predict the electrical conductivity at diverse processing

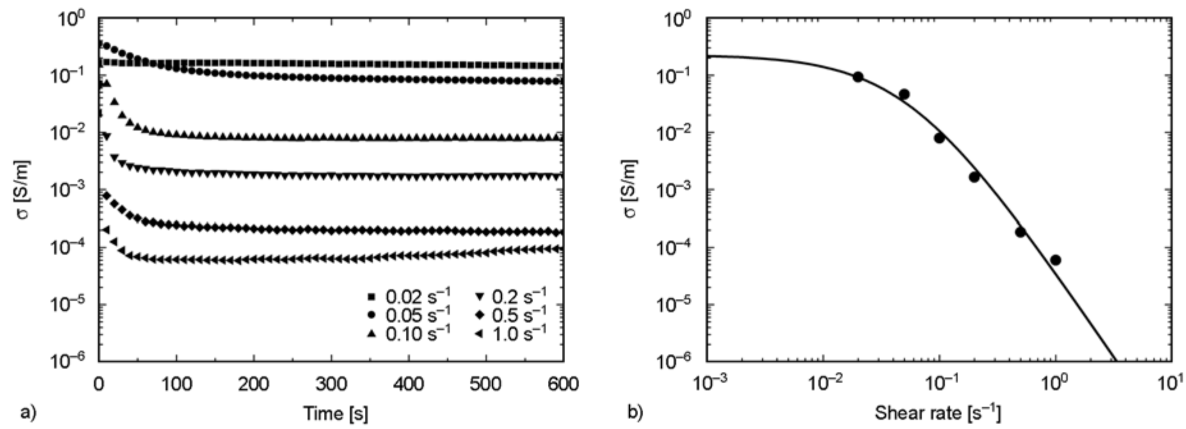

Figure 4. a) Time dependent electrical conductivity at six different shear rates: 0.02, 0.05, 0.1 0.2, 0.5, and 1.0 s^{-1}. $\Phi = 0.75$ wt%, $T = 265°\mathrm{C}$. b) Dependence of stationary electrical conductivity on shear rate. $\Phi = 0.75$ wt%, $T = 265°\mathrm{C}$. Line represents a fit with the help of Equation (14), the shear-thinning exponent $d = 3$.

conditions (after extrusion or injection moulding) based on results measured under laboratory conditions. In the following subsection we shall investigate such a possibility, which is supported by experiments varying both temperature and shear rate.

4.1. Steady-state electrical conductivity

The steady-state electrical conductivity can be calculated from Equation (13) by putting into it the stationary fraction of nanotubes in the percolating network (Equation (15)):

$$1 - f_{\mathrm{st}} = \frac{1}{1 + ab^{-1}\eta(T, \dot{\gamma}_0)\dot{\gamma}_0^{\mathrm{m}}} \qquad (15)$$

Equation (15) is given by a stationary solution of Equation (7b) when df/dt = 0. Thus,

$$\sigma_{\mathrm{Net}}^{\mathrm{st}} = \frac{\sigma_{\mathrm{f}}(T)\,\Delta p_{\mathrm{max}}^2}{[1 + ab^{-1}\eta(T, \dot{\gamma}_0)\dot{\gamma}_0^{\mathrm{m}}]^2} \qquad (16)$$

Equation (16) contains three parameters: shear-thinning conductivity exponent, $m_\sigma = 2m$, the rupture strength a and the rate constant b; the latter two appear in combination as a product $t_{\mathrm{f}} = ab^{-1}$.

Figures 5a and 5b, filled symbols, show shear-thinning dependences of the electrical conductivity measured for polymer composites at two MWNT concentrations (0.75 and 1 wt%) and three melt temperatures (230, 265 and 295°C). The strongest shear-thinning effect has been observed for the system with the lowest MWNT concentration 0.75 wt% and at the lowest temperature 230°C. The steady-state values of the electrical conductivity of the sample sheared at 1 s^{-1} falls 6 orders of magnitude compared to the unsheared system (Figure 5a). The reason of such dramatic behaviour is that, on the one hand, this system is very close to the insulator-conductor transition, and on the other hand, it has the highest matrix viscosity of 10 kPa·s. Hence, very high shear stresses easily bring a weakly percolating MWNT network into a well-dispersed state, characterized by a very low value of the electrical conductivity close to that of the polycarbonate

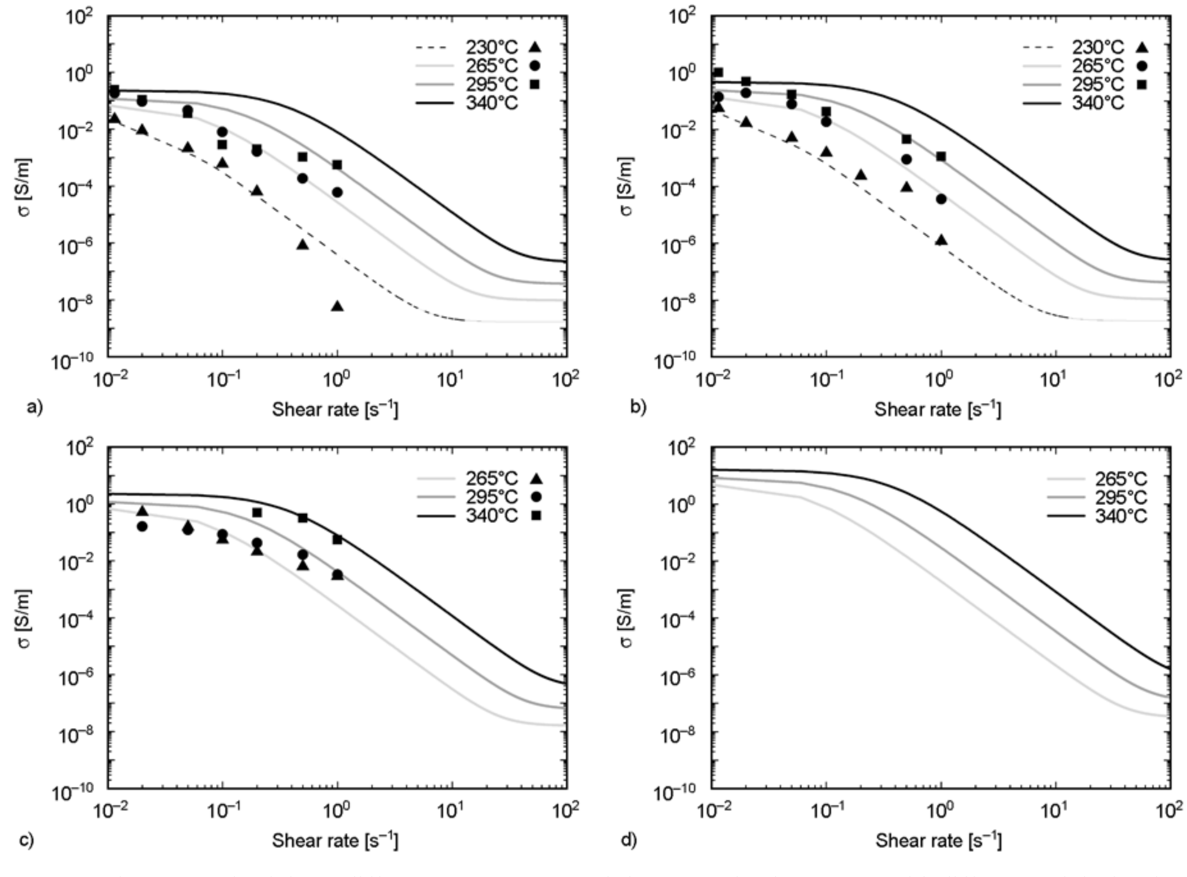

Figure 5. Stationary conductivity at different temperatures and shear rates for the systems with different weight fractions of MWNTs: 0.75 wt% (a), 1 wt% (b), 2 wt% (c) and 5 wt% (d). Experimental data – symbols, fitting – lines. The first symbols plotted at the shear rate of 0.0115 s^{-1} correspond to the conductivity values measured for the unsheared systems. In figures (a) and (b) black solid curve shows predictions for T = 340°C.

matrix. As the matrix viscosity (and thus the shear stress) rapidly decreases with temperature, the shear-thinning effect has been found less pronounced for the samples with the same MWNT concentration but sheared at higher temperatures. For example, at 295°C the electrical conductivity decreases only two orders of magnitude both for the system with 0.75 and 1 wt% MWNTs. However, the system with higher MWNT concentration exhibits a smaller shear-thinning of the electrical conductivity (it falls only 4 orders of magnitude) being farther from the percolation threshold (Figure 5b).

All these features can be captured in the frame of proposed superposition model which describes the conductivity of a percolation network with a changing number of electrical resistors. The fitting results for the systems with 0.75, 1 and 2 wt% MWNTs are presented on Figure 5a–c by different lines. All data are fitted with the same fitting parameters: the shear thinning exponent $m_\sigma = 3$ and $t_f = 0.025$. Thus, the shear-thinning exponent of electrical conductivity is found to be considerably higher than it was reported in two previous studies [36, 51]. At laboratory conditions it was possible to measure credible data for the systems with 0.75 and 1 wt% MWNTs only below 300°C, since above this temperature the samples start to leak from the rheometer cell due to lowered viscosity. Fortunately, after verification of the model on samples with low MWNT concentrations and temperatures it is possible to extrapolate the theory predictions onto the systems with higher MWNT concentrations and temperatures, i.e. to the conditions relevant for nanocomposite processing. Theoretical predictions at the temperature of 340°C, which was found to be optimal for the injection moulding of MWNT/polycarbonate melts [42], are shown on the same Figures 5a and 5b as a black solid line. Additionally, on Figure 5d we present the model predictions for the system with 5 wt% MWNTs at three melt temperatures (265, 295 and 340°C). One can see that the theory predicts a strong reduction of electrical conductivity even for this highly filled system at all melt temperatures, provided that the shear rates exceed 10^2 s^{-1}.

4.2. Percolation curves

There is no general accepted picture in literature what happens with the electrical percolation threshold in sheared systems. While the present authors interpret considerably lower values of conductivity in the sheared system as a reduction of the volume content of the agglomerates composing the conductive percolation network [35–37], other authors attribute the reduction of conductivity to a shift of the percolation threshold to higher values [53, 54]. There even exists an opinion that percolation threshold can become anisotropic under application of the shear forces, the possibility considered in the frame of anisotropic percolation theory, in which the occupation probability is different in two perpendicular directions [55]. Theory of anisotropic electrical conductivity developed by Semeriyanov *et al*. on a Bethe lattice [29] does not presume an anisotropic percolation threshold but an anisotropic conductivity of electrical resistors which may differ in directions parallel and perpendicular to the shear direction. The percolation threshold stays unaffected by the shearing and is solely defined by a functionality of the Bethe lattice. The latter should be adjusted using experimental data for a particular nanocomposite system as was shown in Subsection 3.3. The model proposed in this study is based on the same presumption of shear-independent percolation threshold and neglect orientation effects.

Figure 6a shows theoretical predictions for percolation curves at the fixed value of the percolation threshold $p_c = 0.005$ but at increasing shear rates: 0, 0.1, 1.0 and 10 s^{-1}. Compared to the curve calculated at the quiescent conditions (in the absence of shear), the electrical conductivity falls by two orders of magnitude at $\dot{\gamma}_0 = 0.1$ s^{-1}, five orders of magnitude at $\dot{\gamma}_0 = 1$ s^{-1} and eight orders of magnitude $\dot{\gamma}_0 = 10$ s^{-1}, becoming comparable with the matrix conductivity. Such behaviour, especially the form of two last curves, may give a false impression that the percolation threshold shifts to higher values with the increase of shear rate. From the data in Figure 6b one may conclude that the conductivity data measured for the annealed (equilibrated) sample at the absence of shear and for the injection molded sample can be fitted in the frame of superposition approach without assuming the shift of percolation threshold. However, we do not exclude that for some other systems with strong orientational effects (for example, low viscous epoxies filled with CNTs [53]) the percolation threshold will indeed shift to higher values under strong shearing. This has been found also for CNTs in high viscous polycarbonate

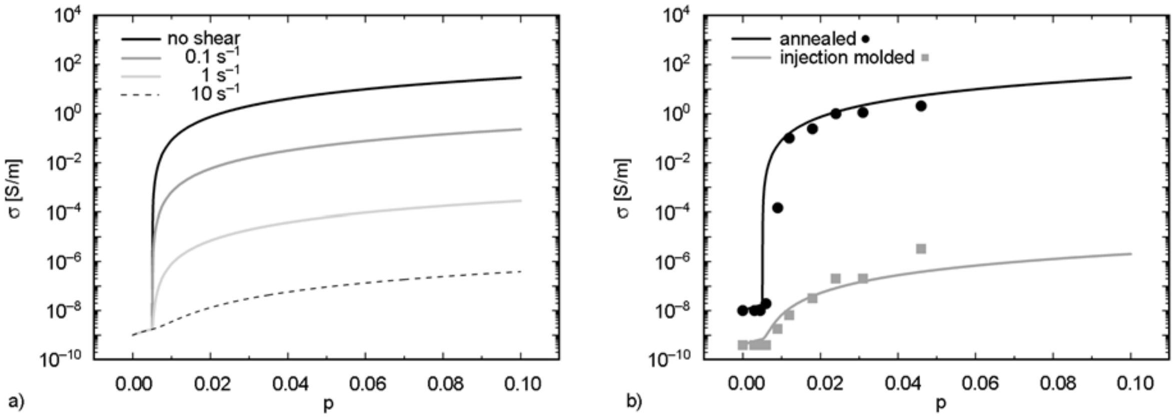

Figure 6. a) Theory prediction for percolation curves at the fixed value of the percolation threshold $p_c = 0.005$, but at increasing shear rates: 0, 0.1, 1.0 and 10 s^{-1}. $T = 230$°C. b) Fit for two samples (lines): Annealed sample is measured at $T = 230$°C in the absence of shear (circles). Injection molded sample ($T = 340$°C, average shear rate 10.0 s^{-1}) is measured at T_{room} (squares).

melt for very high shear rates typical for micro-injection moulding [41].

4.3. Transient electrical conductivity

Electrical conductivity of industrially relevant products produced by the melt processing via extrusion or mould injection depends on a whole history of a product preparation. Therefore, it is important to learn to predict not only stationary values of the electrical conductivity but also its transient behaviour in a wide range of shear rates. For the superposition approach proposed here, a correct prediction of transient behaviour means determination of two parameters in the kinetic Equation (7b): the rupture strength a and the rate constant b. Fitting of the shear-thinning curves (Section 4.1) only provides information about the ratio of these two parameters: $t_f \equiv a/b = 0.025$. One can separate parameters a and b by fitting the time-dependent data for a number of polymer nanocomposite systems with different filler loadings and at different temperatures. To lend the superposition approach a predictive quality at very high shear rates, it is essential to keep both parameters constant for a whole data pool, although it may result in higher discrepancies between experimental data and model predictions at particular shear rates. All data discussed further are fitted with the same values of fitting parameters: $a = 0.25 \cdot 10^{-4}$ $Pa^{-1} \cdot s^{-1/2}$ and $b = 10^2$ s^{-1}.

Comparison of experimental data and model predictions for the system with 0.75 wt% MWNTs is presented in Figure 7 for two different temperatures: 230°C (Figure 7a) and 265°C (Figure 7b). As can be seen, there is some variation in the initial values of electrical conductivity between different curves. Therefore, we have to introduce a correction on the initial state into our model by adjusting an initial value of the fraction of free nanotubes. This considerably improves the fits of time-dependent data measured at the laboratory conditions. The theory predictions at 230°C agree rather well with the experimental data at shear rates up to 0.1 s^{-1}, while at higher shear rates the theory overestimates the rate of shear-induced breakage. The transient behaviour at the shear rate of 1 s^{-1} is badly predicted as the stationary value for this curve is considerably overestimated in the frame of our model (see also Figure 5a). Otherwise, the theory predicts really good the time-dependent data measured at 265°C (Figure 7b).

Comparison of experimental data and model predictions for the system with 1 wt% MWNTs reveals a similar tendency: there is a noticeable overestimation of the rate breakage at 230°C (Figure 7c), while at 265°C the theory predictions fit the data rather good (Figure 7d). Contrary, at 295°C the theory slightly underestimates the rate of shear-induced breakage (not shown here). Finally we show on Figures 7e and 7f comparison between the measured data and the model predictions for the system with 2 wt% MWNTs. The scarceness of data at 340°C (Figure 7f) is due to the problem of sample leaking caused by the lowered matrix viscosity. Nevertheless, the principle agreement between the experiment and theory even at this elevated temperature is rather good.

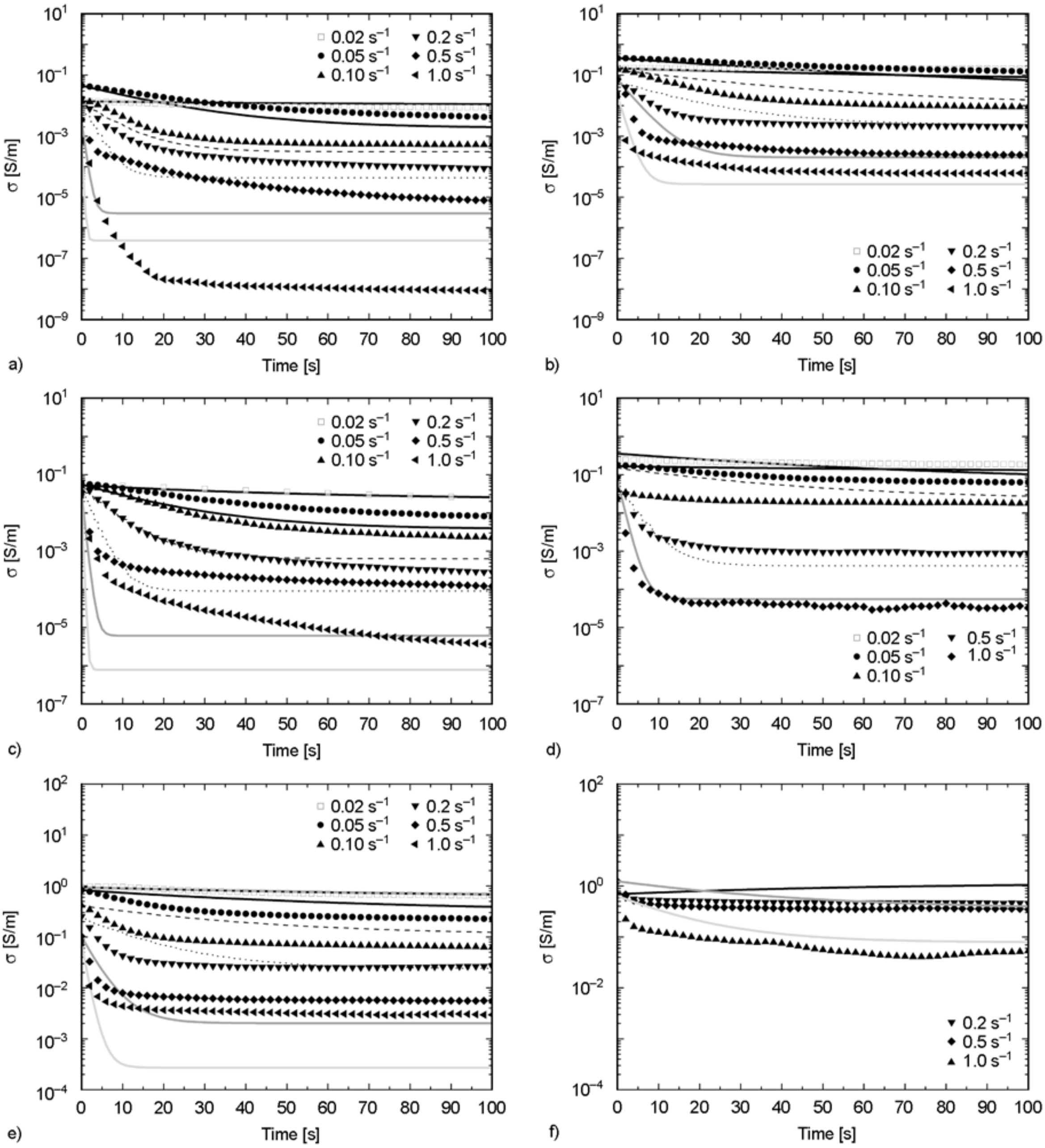

Figure 7. Time dependent electric conductivity at different temperatures and shear rates for the systems with different weight fractions of MWNTs: a) Φ = 0.75 wt%, *T* = 230°C; b) Φ = 0.75 wt%, *T* = 265°C; c) Φ = 1 wt%, *T* = 230°C; d) Φ = 1 wt%, *T* = 265°C; e) Φ = 2 wt%, *T* = 265°C; f) Φ = 2 wt%, *T* = 340°C. Experimental data – symbols, fitting – lines.

Presently, we use a simple form of kinetic equation given by expression (7b) which contains only two terms and, hence, three fitting parameters (including the shear-thinning exponent). To improve description of the time-dependent data, one needs to consider a more elaborated kinetic equation, which may contain an additional term for shear-induced aggregation, or even a hierarchic set of kinetic equations [36]. However, this will introduce a number of additional fitting parameters and thus considerably complicate the task of their extraction from the fitting procedure. This will be a topic of the next paper, while in the present studies we maintained the simplified picture of filler network kinetics.

5. Conclusions

In this paper we present a superposition approach for description of electrical conductivity in sheared polymer melts filled with attractively interacting conductive (anisometric) particles. The main assumption of superposition approach is that the filler particles can be separated into two phases: the percolating one and non-percolating one. In the absence of shear, if the percolation probability exceeds the percolation threshold, (nearly) all particles belong to the percolating phase (network) and strongly contribute to the electrical conductivity. In the presence of shear, some particles are ruptured from the network (or the percolating phase is dispersed into smaller parts) and thus they are considered to belong to the non-percolating phase. The process of network rupture, i.e. how large is the fraction of free particles, is described by an appropriate kinetic equation. This fraction defines the enhancement of electrical conductivity of the polymer matrix given by the theory of effective electrical conductivity of composites with spheroidal inclusions at low volume fractions [18]. Presently, for the sake of simplicity, it is assumed that the particles belonging to the non-percolating phase are oriented randomly. This seems to hold for small and medium shear rates. Though it is possible to account for orientational effects in the non-percolating phase using for example the Folgar-Tucker equation [19, 20].

The conductivity of percolating phase is described with the help of a coupling approach based on the classic percolation theory. There are two main assumptions of our approach:

1) the percolation probability depends on the history of shear application,
2) the particles in the percolation phase are oriented randomly.

If for some other system it will be find out that the percolating clusters are noticeably deformed by the flow before their breakage, one can try to account for this effect using the theory of anisotropic electrical conductivity proposed recently by Semeriyanov *et al* [29].

The superposition approach has been tested in the present studies on the polycarbonate composites filled with multi-walled CNTs. Four different melt temperatures, three nanotube concentrations and up to six different shear rates have been used to extract the time-dependent and shear-thinning behaviour of electrical conductivity. This allowed us to show that the 'shear-thinning' exponent of electrical conductivity is about 3 which is considerably higher than it was reported in two previous studies [36, 51]. In overall, we found a rather good agreement between the theory predictions and the experimental data. This means that results measured at relatively small shear rates in the laboratory conditions can be extrapolated to much higher shear rates typical for extrusion and injection moulding conditions. Thus, the superposition approach, if implemented in a commercial flow software, may open a way to predict – at least semi-quantitatively – the electrical conductivity of industrial products produced from polymer composites filled with highly attractive conductive particles at diverse processing conditions.

Acknowledgements

This work was carried out with the support of the BMBF Project 'CarboNet' No. 03X0504E and 03X0504F. Dr. Bierdel (Bayer Technology Services GmbH, Leverkusen, Germany) is greatly acknowledged for providing the samples for rheo-electrical measurements. Further, we would like to thank Dr. Fyodor Semeriyanov (IPF Dresden) for very helpful discussions concerning the modelling part.

References

[1] Coleman J. N., Curran S., Dalton A. B., Davey A. P., McCarthy B., Blau W., Barklie R. C.: Percolation-dominated conductivity in a conjugated-polymer-carbon-nanotube composite. Physical Review B, **58**, 7492–7495 (1998).
DOI: 10.1103/PhysRevB.58.R7492

[2] Pötschke P., Dudkin S. M., Alig I.: Dielectric spectroscopy on melt processed polycarbonate–multiwalled carbon nanotube composites. Polymer, **44**, 5023–5030 (2003).
DOI: 10.1016/S0032-3861(03)00451-8

[3] Sandler J. K. W., Kirk J. E., Kinloch I. A., Shaffer M. S. P., Windle A. H.: Ultra-low electrical percolation threshold in carbon-nanotube-epoxy composites. Polymer, **44**, 5893–5899 (2003).
DOI: 10.1016/S0032-3861(03)00539-1

[4] Bauhofer W., Kovacs J. Z.: A review and analysis of electrical percolation in carbon nanotube polymer composites. Composites Science and Technology, **69**, 1486–1498 (2009).
DOI: 10.1016/j.compscitech.2008.06.018

[5] Pötschke P., Fornes T. D., Paul D. R.: Rheological behavior of multiwalled carbon nanotube/polycarbonate composites. Polymer, **43**, 3247–3255 (2002).
DOI: 10.1016/S0032-3861(02)00151-9

[6] Pötschke P., Abdel-Goad M., Alig I., Dudkin S., Lellinger D.: Rheological and dielectrical characterization of melt mixed polycarbonate-multiwalled carbon nanotube composites. Polymer, **45**, 8863–8870 (2004).
DOI: 10.1016/j.polymer.2004.10.040

[7] Heinrich G., Klüppel M.: Recent advances in the theory of filler networking in elastomers. Advances in Polymer Science, **160**, 1–44 (2002).

[8] Fan Z., Advani S. G.: Rheology of multiwall carbon nanotube suspensions. Journal of Rheology, **51**, 585–604 (2007).
DOI: 10.1122/1.2736424

[9] Pegel S., Pötschke P., Petzold G., Alig I., Dudkin S. M., Lellinger D.: Dispersion, agglomeration, and network formation of multiwalled carbon nanotubes in polycarbonate melts. Polymer, **49**, 974–984 (2008).
DOI: 10.1016/j.polymer.2007.12.024

[10] Gojny F. H., Wichmann M. H. G., Fiedler B., Schulte K.: Influence of different carbon nanotubes on the mechanical properties of epoxy matrix composites – A comparative study. Composites Science and Technology, **65**, 2300–2313 (2005).
DOI: 10.1016/j.compscitech.2005.04.021

[11] Gojny F. H., Wichmann M. H. G., Fiedler B., Kinloch I. A., Bauhofer W., Windle A. H., Schulte K.: Evaluation and identification of electrical and thermal conduction mechanisms in carbon nanotube/epoxy composites. Polymer, **47**, 2036–2045 (2006).
DOI: 10.1016/j.polymer.2006.01.029

[12] Alig I., Skipa T., Lellinger D., Pötschke P.: Destruction and formation of a carbon nanotube network in polymer melts: Rheology and conductivity spectroscopy. Polymer, **49**, 3524–3532 (2008).
DOI: 10.1016/j.polymer.2008.05.037

[13] Alig I., Skipa T., Engel M., Lellinger D., Pegel S., Pötschke P.: Electrical conductivity recovery in carbon nanotube–polymer composites after transient shear. Physica Status Solidi B, **244**, 4223–4226 (2007).
DOI: 10.1002/pssb.200776138

[14] Alig I., Lellinger D., Dudkin S. M., Pötschke P.: Conductivity spectroscopy on melt processed polypropylene–multiwalled carbon nanotube composites: Recovery after shear and crystallization. Polymer, **48**, 1020–1029 (2007).
DOI: 10.1016/j.polymer.2006.12.035

[15] Alig I., Lellinger D., Engel M., Skipa T., Pötschke P.: Destruction and formation of a conductive carbon nanotube network in polymer melts: In-line experiments. Polymer, **49**, 1902–1909 (2008).
DOI: 10.1016/j.polymer.2008.01.073

[16] Villmow T., Pegel S., Pötschke P., Wagenknecht U.: Influence of injection molding parameters on the electrical resistivity of polycarbonate filled with multiwalled carbon nanotubes. Composites Science and Technology, **68**, 777–789 (2008).
DOI: 10.1016/j.compscitech.2007.08.031

[17] Du F., Fischer J. E., Winey K. I.: Effect of nanotube alignment on percolation conductivity in carbon nanotube/polymer composites. Physical Review B, **72**, 121404/1–121404/4 (2005).
DOI: 10.1103/PhysRevB.72.121404

[18] Zheng X., Forest M. G., Lipton R., Zhou R., Wang Q.: Exact scaling laws for electrical conductivity properties of nematic polymer nanocomposite monodomains. Advanced Functional Materials, **15**, 627–638 (2005).
DOI: 10.1002/adfm.200400200

[19] Lertwimolnun W., Vergnes B., Ausias G., Carreau P. J.: Stress overshoots of organoclay nanocomposites in transient shear flow. Journal of Non-Newtonian Fluid Mechanics, **141**, 167–179 (2007).
DOI: 10.1016/j.jnnfm.2006.11.003

[20] Folgar F., Tucker C. L.: Orientation behavior of fibers in concentrated suspensions. Journal of Reinforced Plastics and Composites, **3**, 98–119 (1984).
DOI: 10.1177/073168448400300201

[21] Kirkpatrick S.: Percolation and conduction. Reviews of Modern Physics, **45**, 574–588 (1973).
DOI: 10.1103/RevModPhys.45.574

[22] Sahimi M.: Flow phenomena in rocks: From continuum models to fractals, percolation, cellular automata, and simulated annealing. Reviews of Modern Physics, **65**, 1393–1534 (1993).
DOI: 10.1103/RevModPhys.65.1393

[23] Halperin B. I., Feng S., Sen P. N.: Differences between lattice and continuum percolation transport exponents. Physical Review Letters, **54**, 2391–2394 (1985).
DOI: 10.1103/PhysRevLett.54.2391

[24] Feng S., Halperin B. I., Sen P. N.: Transport properties of continuum systems near the percolation threshold. Physical Review B, **35**, 197–214 (1987).
DOI: 10.1103/PhysRevB.35.197

[25] Balberg I.: Limits on the continuum-percolation transport exponents. Physical Review B, **57**, 13351–13354 (1998).
DOI: 10.1103/PhysRevB.57.13351

[26] Skal A. S., Shklovskii B. I.: Topology of the infinite cluster of the percolation theory and its relationship to the theory of hopping conduction. Soviet Physics Semiconductors, **8**, 1029–1032 (1975).

[27] de Gennes P. G.: On a relation between percolation theory and the elasticity of gels. Journal de Physique Lettres, **37**, 1–2 (1976).
DOI: 10.1051/jphyslet:019760037010100

[28] Stinchcombe R. B.: Branching model for percolation theory and electrical conductivity. Journal of Physics C: Solid State Physics, **6**, L1–L5 (1973).
DOI: 10.1088/0022-3719/6/1/001

[29] Semeriyanov F., Saphiannikova M., Heinrich G.: Anisotropic generalization of Stinchcombe's solution for the conductivity of random resistor networks on a Bethe lattice. Journal of Physics A: Mathematical and Theoretical, **42**, 465001/1–465001/17 (2009).
DOI: 10.1088/1751-8113/42/46/465001

[30] Eken A. E., Tozzi E. J., Klingenberg D. J., Bauhofer W.: A simulation study on the combined effects of nanotube shape and shear flow on the electrical percolation thresholds of carbon nanotube/polymer composites. Journal of Applied Physics, **109**, 084342/1–084342/9 (2011).
DOI: 10.1063/1.3573668

[31] Eken A. E., Tozzi E. J., Klingenberg D. J., Bauhofer W.: A simulation study on the effects of shear flow on the microstructure and electrical properties of carbon nanotube/polymer composites. Polymer, **52**, 5178–5185 (2011).
DOI: 10.1016/j.polymer.2011.08.041

[32] Schueler R., Petermann J., Schulte K., Wentzel H-P.: Percolation in carbon black filled epoxy resin. Macromolecular Symposia, **104**, 261–268 (1996).
DOI: 10.1002/masy.19961040122

[33] Schueler R., Petermann J., Schulte K., Wentzel H-P.: Agglomeration and electrical percolation behavior of carbon black dispersed in epoxy resin. Journal of Applied Polymer Science, **63**, 1741–1746 (1997).
DOI: 10.1002/(SICI)1097-4628(19970328)63:13<1741::AID-APP5>3.0.CO;2-G

[34] Heinrich G., Costa F. R., Abdel-Goad M., Wagenknecht U., Lauke B., Härtel V., Tschimmel J., Klüppel M., Svistkov A. L.: Structural kinetics in filled elastomers and PE/LDH composites. Kautschuk Gummi Kunstoffe, **58**, 163–167 (2005).

[35] Skipa T., Lellinger D., Saphiannikova M., Alig I.: Shear-stimulated formation of multi-wall carbon nanotube networks in polymer melts. Physica Status Solidi B, **246**, 2453–2456 (2009).
DOI: 10.1002/pssb.200982265

[36] Skipa T., Lellinger D., Böhm W., Saphiannikova M., Alig I.: Influence of shear deformation on carbon nanotube networks in polycarbonate melts: Interplay between build-up and destruction of agglomerates. Polymer, **51**, 201–210 (2010).
DOI: 10.1016/j.polymer.2009.11.047

[37] Alig I., Skipa T., Lellinger D., Bierdel M., Meyer H.: Dynamic percolation of carbon nanotube agglomerates in a polymer matrix: Comparison of different model approaches. Physica Status Solidi B, **245**, 2264–2267 (2008).
DOI: 10.1002/pssb.200879622

[38] Lellinger D., Xu D., Ohneiser A., Skipa T., Alig I.: Influence of the injection moulding conditions on the in-line measured electrical conductivity of polymer–carbon nanotube composites. Physica Status Solidi B, **245**, 2268–2271 (2008).
DOI: 10.1002/pssb.200879619

[39] Torquato S.: Random heterogeneous materials: Microstructure and macroscopic properties, interdiciplinary applied mathematics. Springer, New York (2002).

[40] McLachlan D. S., Blaszkiewicz M., Newnham R. E.: Electrical resistivity of composites. Journal of the American Ceramic Society, **73**, 2187–2203 (1990).
DOI: 10.1111/j.1151-2916.1990.tb07576.x

[41] Abbasi S., Carreau P. J., Derdouri A.: Flow induced orientation of multiwalled carbon nanotubes in polycarbonate nanocomposites: Rheology, conductivity and mechanical properties. Polymer, **51**, 922–935 (2010).
DOI: 10.1016/j.polymer.2009.12.041

[42] Richter S., Saphiannikova M., Jehnichen D., Bierdel M., Heinrich G.: Experimental and theoretical studies of agglomeration effects in multi-walled carbon nanotube-polycarbonate melts. Express Polymer Letters, **3**, 753–768 (2009).
DOI: 10.3144/expresspolymlett.2009.94

[43] Kota A. K., Cipriano B. H., Powell D., Raghavan S. R., Bruck H. A.: Quantitative characterization of the formation of an interpenetrating phase composite in polystyrene from the percolation of multiwalled carbon nanotubes. Nanotechnology, **18**, 505705/1–505705/7 (2007).
DOI: 10.1088/0957-4484/18/50/505705

[44] Cipriano B. H., Kota A. K., Gershon A. L., Laskowski C. J., Kashiwagi T., Bruck H. A., Raghavan S. R.: Conductivity enhancement of carbon nanotube and nanofiber-based polymer nanocomposites by melt annealing. Polymer, **49**, 4846–4851 (2008).
DOI: 10.1016/j.polymer.2008.08.057

[45] Huang Y. Y., Ahir S. V., Terentjev E. M.: Dispersion rheology of carbon nanotubes in a polymer matrix. Physical Review B, **73**, 125422/1–125422/4 (2006).
DOI: 10.1103/PhysRevB.73.125422

[46] Albano E. V., Mártin H. O.: Percolation of interacting particles deposited onto a planar substrate. Thin Solid Films, **151**, 121–132 (1987).
DOI: 10.1016/0040-6090(87)90014-9

[47] Seaton N. A., Glandt E. D.: Conductivity from simulations of percolating systems of interacting particles. Journal of Physics A: Mathematical and General, **20**, 3029–3034 (1987).
DOI: 10.1088/0305-4470/20/10/044

[48] Dullaert K., Mewis J.: A structural kinetics model for thixotropy. Journal of Non-Newtonian Fluid Mechanics, **139**, 21–30 (2006).
DOI: 10.1016/j.jnnfm.2006.06.002

[49] Bilotti E., Zhang R., Deng H., Baxendale M., Peijs T.: Fabrication and property prediction of conductive and strain sensing TPU/CNT nanocomposite fibres. Journal of Materials Chemistry, **20**, 9449–9455 (2010).
DOI: 10.1039/c0jm01827a

[50] Osswald T. A., Menges G.: Material science of polymers for engineers. Hanser, Munich (2003).

[51] Kharchenko S. B., Douglas J. F., Obrzut J., Grulke E. A., Migler K. B.: Flow-induced properties of nanotube-filled polymer materials. Nature Materials, **3**, 564–568 (2004).
DOI: 10.1038/nmat1183

[52] Carreau P. J., De Kee D. C. R., Chhabra R. P.: Rheology of polymeric systems: Principles and applications. Hanser, New York (1997).

[53] Xu J., W, Florkowski W., Gerhardt R., Moon K-S., Wong C-P.: Shear modulated percolation in carbon nanotube composites. Journal of Physical Chemistry B, **110**, 12289–12292 (2006).
DOI: 10.1021/jp061090i

[54] Obrzut J., Douglas J. F., Kharchenko S. B., Migler K. B.: Shear-induced conductor-insulator transition in melt-mixed polypropylene-carbon nanotube dispersions. Physical Review B, **76**, 195420/1–195420/9 (2007).
DOI: 10.1103/PhysRevB.76.195420

[55] Friedman S. P., Seaton N. A.: Technical note: Percolation thresholds and conductivities of a uniaxial anisotropic simple-cubic lattice. Transport in Porous Media, **30**, 241–250 (1998).
DOI: 10.1023/A:1006575828107

eXPRESS Polymer Letters Vol.6, No.6 (2012) 454–464
Available online at www.expresspolymlett.com
DOI: 10.3144/expresspolymlett.2012.48

A new conjugated polymer with donor-acceptor architectures based on alternating 1,4-divinyl-2,5-dioctyloxybenzene and 5,8-(2,3-dipyridyl)-quinoxaline: Synthesis, characterization, and photoinduced charge transfer

S. J. Chen, Q. Y. Zhang, J. W. Gu, M. L. Ma, L. Zhang, J. Zhou, Y. Y. Zhou*

Key Laboratory of Space Applied Physics and Chemistry, Ministry of Education, Department of Applied Chemistry, Northwestern Polytechnical University, 710129 Shaanxi Xi'an, PR China

Received 25 October 2011; accepted in revised form 26 December 2011

Abstract. A new conjugated polymer with donor-accepter architectures poly[1,4-dioctyloxyphenylene-2,5-diylethenylene-(2,3-dipyridine-2-ylquinoxaline-5,8-diyl)ethylene] (PPV-BD) was synthesized successfully, in which the electron-donating unit was alkoxy substituted phenyl ring, and the electron-accepting unit was a quinoxaline. The resulting polymer had a lower band-gap (1.98 eV) compared to poly[2-methoxy-5-(2-ethyl)hexoxy-phenylenevinylene] (MEH-PPV, 2.12 eV), and was characterized by infrared spectroscopy (IR), nuclear magnetic resonance (NMR), thermogravimetric analysis (TGA), gel permeation chromatography (GPC), ultraviolet-visible (UV-vis) spectroscopy, photoluminescence (PL) spectroscopy and X-ray diffraction (XRD). Its photoinduced charge transfer applications in polymer solar cell (PSC) and trinitrotoluene (TNT) detection were studied respectively, and the results indicated that this polymer might be a good candidate material for PSC or detecting TNT in solution.

Keywords: *polymer synthesis, characterization, chemosensor material, photoinduced charge transfer, photovoltaic material*

1. Introduction

Conjugated polymers have attracted considerable attention due to their versatile applications in the fields of polymer light-emitting diodes (PLED) [1–3], polymer field-effect transistors (PFETs) [4, 5], chemical sensors [6], photodetectors [7], polymer solar cells (PSCs) [8], etc. In recent years, several polymers based on poly(phenylenevinylenes) (PPVs) have been synthesized and used as the active layer in photovoltaic devices [9–13]. A major drawback of most conjugated polymers for their application in PSCs is the rather poor match of the absorbance spectrum with the solar spectrum. The wavelength of maximum absorbance for most PPV derivatives lies below 500 nm (E_g = 2.0~2.2 eV), which is on the far blue side of the spectrum [14, 15]. By using low band-gap materials, an improved overlap with the solar spectrum would allow an increase in photovoltaic energy conversion. The band-gap of π-conjugated polymers can be controlled through the chemical structure of the system [16]. π-conjugated polymers with donor-acceptor architectures are currently of interest because the intramolecular charge transfer can facilitate ready manipulation of the electronic structure (HOMO/LUMO levels), leading to small band-gap semiconducting polymers [17–20]. In addition, conjugated polymers have been proven quite useful in creating highly sensi-

---

*Corresponding author, e-mail: qyzhang1803@gmail.com

tive fluorescent chemical sensors [21–23]. The conjugated polymer backbone allows efficient electron delocalization and exciton migration over large distances, thereby creating amplified sensory responses compared with small-molecule-based sensors. An additional advantage of using polymers as sensor materials emerges from that the sensory devices can easily be fabricated from these materials on electrodes either by spin coating and/or drop casting from solution or anodic electrochemical polymerization from an electrolyte solution.

In this paper, a new conjugated polymer with donor-accepter architectures poly[1,4-dioctyloxyphenylene-2,5-diylethenylene-(2,3-dipyridine-2-ylquinoxaline-5,8-diyl)ethylene] (PPV-BD) was synthesized successfully, in which the electron-donating unit was alkoxy substituted phenyl rings, and the electron-accepting unit was a quinoxaline. The quinoxaline is a good electron-accepting unit, and it has been designed in donor-acceptor fluorine-based or thiophene-based copolymers [24]. The resulting polymer had a lower band-gap (1.98 eV) compared to poly[2-methoxy-5-(2-ethyl)hexoxy-phenylenevinylene] (MEH-PPV, 2.12 eV [25]), and was characterized by infrared spectroscopy (IR), nuclear magnetic resonance (NMR), thermogravimetric analysis (TGA), gel permeation chromatography (GPC), ultraviolet-visible (UV-vis) and photoluminescence (PL) spectroscopy. Additionally, its photoinduced charge transfer (PCT) applications in PSCs and trinitrotoluene (TNT) detection were studied respectively, and the results indicated that this polymer might be a good candidate material for PSCs or detecting TNT in solution. The molecular structure of PPV-BD is shown in Figure 1.

2. Experimental

2.1. Materials

The main reagents such as p-hydroquinone (AR, Analytical Reagent), palladium (II) acetate (AR), 2,2′-bipyridyl (AR), [Bu(4)N]BF(4) (AR) were purchased from J&K Scientific Ltd., China, used as received. All the solvents used in this study were purified according to standard methods prior to use.

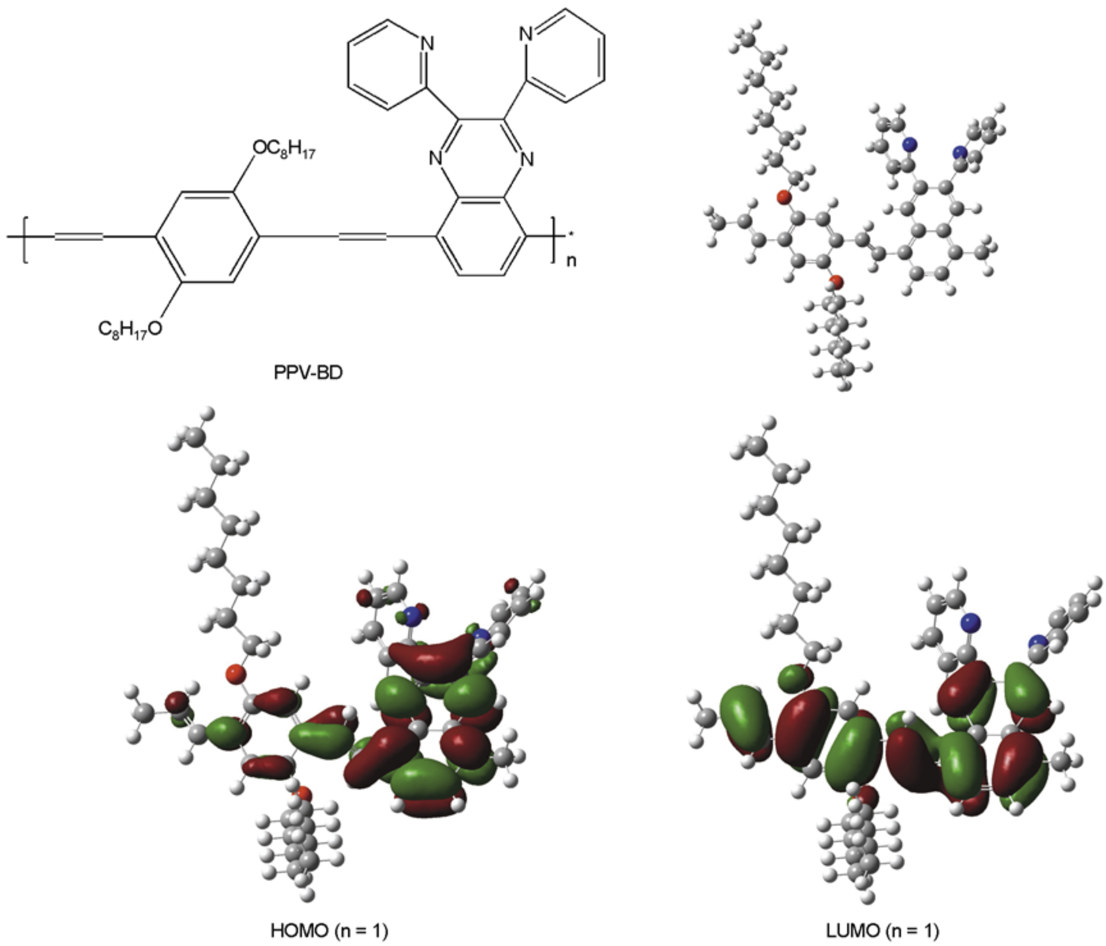

Figure 1. Molecular structure of polymer PPV-BD

1,4-divinyl-2,5-dioctyloxybenzene (monomers 1) and 5,8-dibromo-2,3-dipyridylquinoxaline (monomer 2) were synthesized according to the published literatures [26–28].

2.2. Measurements

The target compounds were characterized by NMR spectra using Bruker AVANCE 400 spectrometer (Bruker Corporation, Karlsruhe, Germany) with chloroform-d as the solvent and tetramethylsilane as the internal standard. Polymer molecular weight was determined by size-exclusion chromatography with multi-angle laser light-scattering detection (SEC-MALLS). SEC was performed using a high-performance liquid chromatography (HPLC) pump (Waters 515, Waters Corporation, USA) and a column (200 mm × 0.8 mm, MZ-Gel SDplus 500Å 5 μm). Column effluent was monitored sequentially with a miniDawn light-scattering detector (Wyatt technology Corporation, Santa, Barbara, CA, USA) and an Optical rEX differential refractometer (Wyatt Technology Corporation, Santa, Barbara, CA, USA). Two 25 mm high-pressure filter with 0.22 and 0.1 μm pores (Millipore Corporation, Bedford, Massachusetts, USA) were used for on-line filtration of the mobile phase. UV-vis spectra were recorded on a Shimadzu UV-2501PC/2550 (Shimadzu Corporation, Kyoto, Japan). Photoluminescence spectra were measured in a HITACHI F-4600 fluorescence spectrometer (Hitachi Corporation, Tokyo, Japan). FT-IR spectra were taken on a Bruker Tensor 27FT-IR spectrophotometer (Bruker Corporation, Karlsruhe, Germany) with KBr pellets. Thermogravimetric analysis (TGA) of the synthesized polymer was performed on a HENVEN HCT-1 (Beijing Scientific Instrument Factory, Beijing, China) thermal analysis system at a heating rate of 10°C/min up to 500°C in a nitrogen flow rate of 80 mL/min. Elemental C, H, N was performed on a Flash EA 1112 elemental analyzer (Thermo Electron Corporation, Waltham, USA). Cyclic voltammetry was carried out using thin films of polymer prepared from chloroform with PARSTAT-2273 (Princeton Applied Research, AMETEK, Inc., Oak Ridge, USA) in a solution of [Bu(4)N]BF(4) (0.1M) in acetonitrile at a scan rate 50 mV/s. Scanning electron microscope (SEM) images were performed in Shimadzu SSX-550 (Shimadzu Corporation, Kyoto, Japan). X-ray diffraction (XRD) data were collected using a Siemens Bruker D500 X-ray diffractometer (Bruker Corporation, Karlsruhe, Germany) at a scanning rate of 4°/min in the 2θ range from 0 to 80°, with graphite monochromatized Cu Kα radiation.

2.3. Syntheses of monomers and polymer

PPV-BD was synthesized via the Heck reaction polycondensation between monomer 1 and monomer 2 in presence of palladium (II) acetate catalyst. The synthetic routes of polymer PPV-BD are shown in Figure 2.

The syntheses of the monomer 1, monomer 2 and polymer PPV-BD are described as follows:

Synthesis of monomer 1 [26, 27]

Monomer 1 was synthesized according to the literatures [26, 27]. 18.06 g (17.3 mmol) of 1,4-bis(bromide-triphenylphosphine methyl)-2,5-dioctyloxybenzene was dissolved in a co-solvent of 230 mL dichloromethane and 70 mL (40%) formaldehyde solution. Then, 140 mL (20%) NaOH solution was added dropwise, the mixture was stirred for 15 h at 0°C under inert atmosphere. Finally, 30 mL water and 60 mL dichloromethane were added into the reactive solution. The organic layer was separated and washed by water, then dried with anhydrous Na_2SO_4. The crude product was formed after sol-

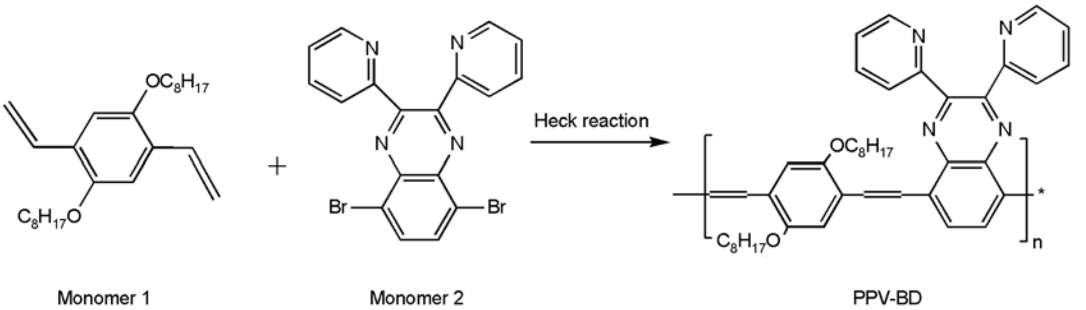

Figure 2. Synthetic routes of polymer PPV-BD

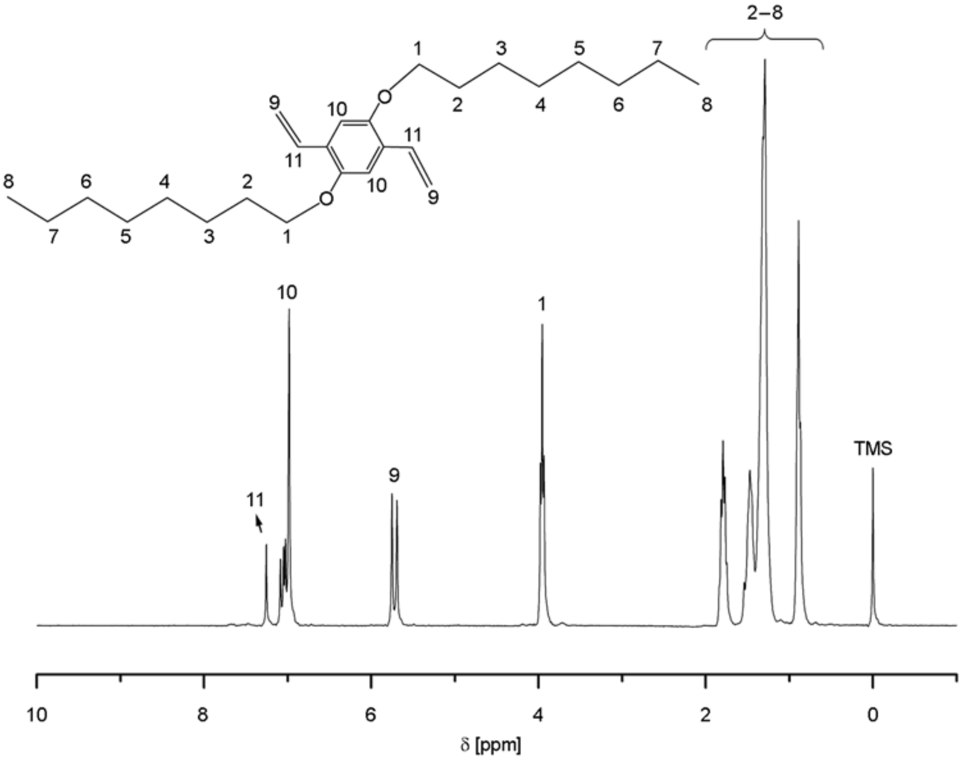

Figure 3. ^{1}H NMR spectrum of 1,4-bis(octyloxy)-2,5-divinylbenzene

vents evaporating, and recrystallized with ethanol several times to get 3.68 g of monomer 1 as white crystals. Yield 55%, mp: 45–46°C.

^{1}H NMR (CDCl$_3$; δ/ppm): 0.87–1.82 (m, 30H, H2–H8), 3.93–3.98 (t, 4H, H1), 5.69–5.71 (d, 4H, H9), 6.98 (s, 2H, H10), 7.03–7.08 (t, 2H, H11) (details in Figure 3). FT-IR (KBr, cm^{-1}): 3082 (υ(Ar–H), υ(=CH$_2$)), 3019 (υ(=CH)), 2943, 2919 (υ$_{as}$(–CH$_3$, –CH$_2$–)), 2850 (υ$_s$(–CH$_3$, –CH$_2$–)), 1212 (υ(C–O), 1618, 1500, 1466 (Ar(C=C), vinyl-υ(C=C)), 993, 893 (γ(CH=CH$_2$)). Anal. Calcd. (%) for $C_{26}H_{42}O_2$ (386.61): C, 80.77; H, 10.95. Found (%): C, 80.71; H, 12.27.

Synthesis of monomer 2 [28]

A solution of 2,3-diamino-1,4-dibromobenzene (1.03 g, 3.8 mmol) and 2,2′-bipyridil (0.806 g, 3.8 mmol) in 25 mL ethanol was heated to reflux for 3 h, then cooled to 0°C. The formed precipitate was isolated by filtration and washed with ethanol to afford 1.16 g of monomer 2 as yellow solid. Yield 70%, mp: 251–253°C.

^{1}H NMR (CDCl$_3$; δ/ppm): 7.25–7.28 (d, 2H, H4), 7.87–7.98 (d, 2H, H1, H2, H3), 8.26–8.32 (m, 4H, H5) (details in Figure 4). ^{13}C NMR (CDCl$_3$; δ/ppm): 123.4, 123.8, 124.5, 133.6, 136.9, 139.3, 148.2, 153.4, 156.5. Anal. Calcd. (%) for $C_{18}H_{10}Br_2N_4$ (442.11): C, 48.90; H, 2.28; N, 12.67. Found (%): C, 48.01; H, 2.47; N, 11.53.

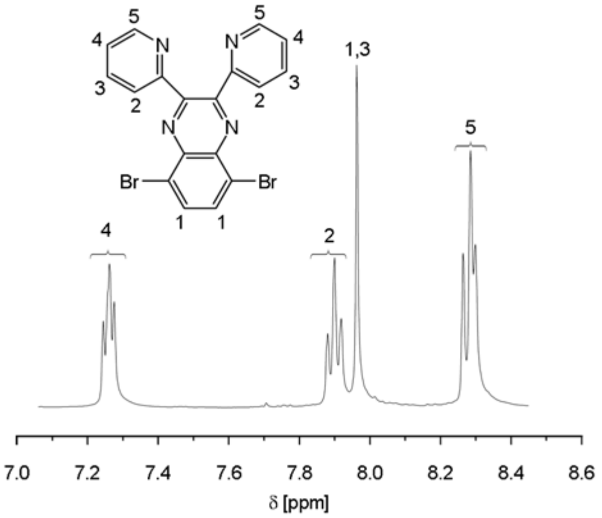

Figure 4. ^{1}H NMR spectrum of 5,8-dibromo-2, 3-dipyridy-quinoxaline

Synthesis of PPV-BD

250 mg (0.65 mmol) of monomer 1, 240 mg (0.65 mmol) of monomer 2, 14.6 mg (0.065 mmol) of palladium acetate and 248 mg (0.81 mmol) of tris(2-methylphenyl)phosphine were added into a

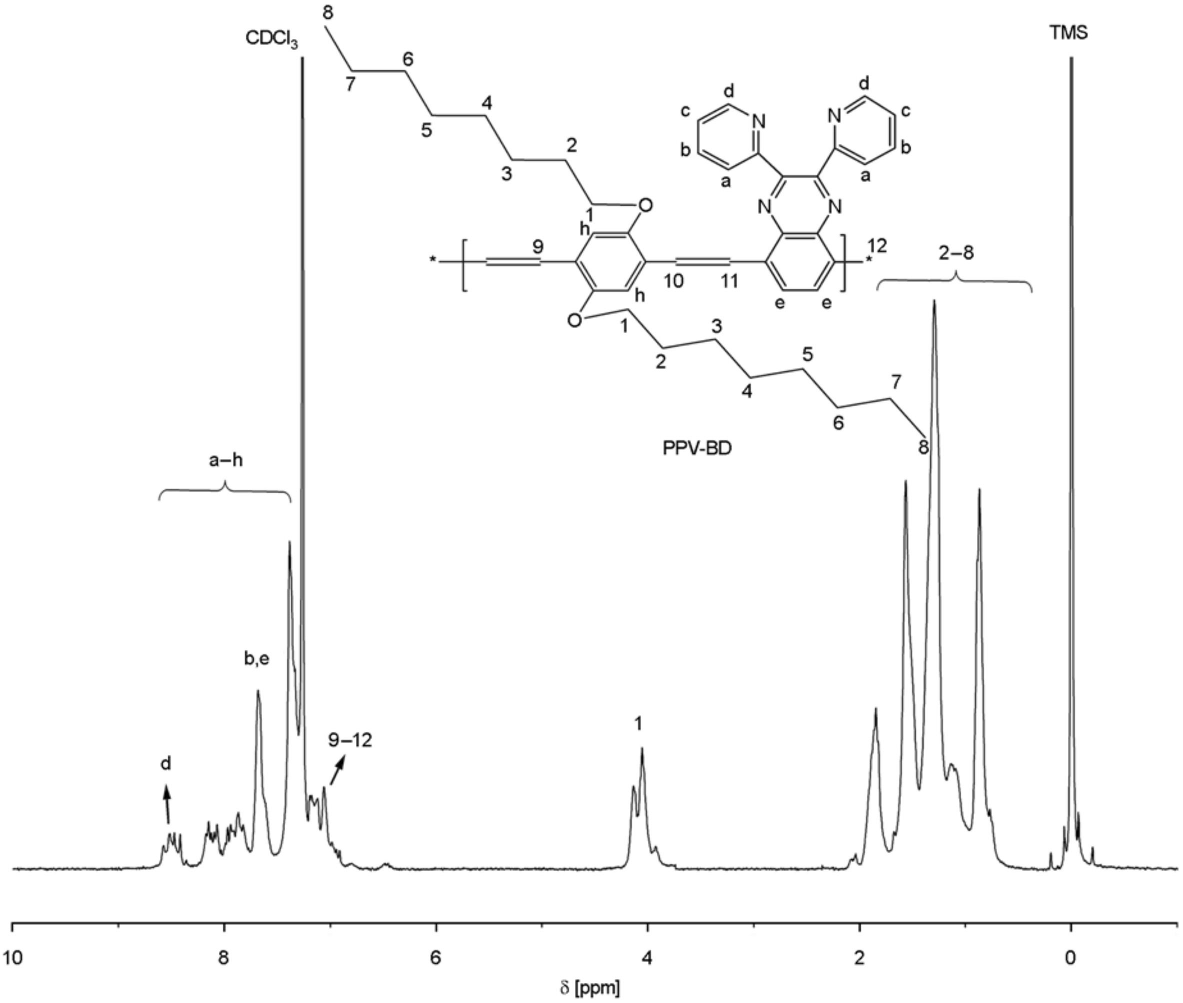

Figure 5. ^{1}H NMR spectrum in CDCl$_3$ of PPV-BD

co-solvent of 4 mL triethylamine and 10 mL N′N-dimethylformamide. The mixed solution was heated to reflux for 24 h under inert atmosphere. After cooling to room temperature, the reactant was added into 300 mL methanol slowly. The resulting precipitate was centrifugated to collect 150 mg of polymer PPV-BD as a deep-red powder. Yield 36%.

^{1}H NMR (CDCl$_3$; δ/ppm): 0.77–1.85 (m, 30H, H2–H8), 3.93–4.14 (d, 4H, H1), 6.98–7.19 (m, 4H, H9–H12), 7.33–8.52 (m, 12H, Ha-Hh) (details in Figure 5). FT-IR(KBr, cm^{-1}): 3060 (υ(Ar–H, or vinyl-H)), 2930 (υ$_{as}$(–CH$_3$, –CH$_2$–)), 2850 (υ$_s$(–CH$_3$, –CH$_2$–)), 1672 (υ(C=N)), 1595, 1466 (υ(Ar(C=C)), 1384 (δ(-CH3)), 1278 (υ(C-C)), 1203 (υ(C–O)), 751 (γ(Ar(=CH)). GPC(polystyrene standards): M_n = 11 010, M_w = 15 050, PDI = 1.37. Anal. Calcd. (%) for $(C_{44}H_{50}N_4O_2)_n$ $(666.92)_n$: C, 79.05; H, 7.78; N, 8.38. Found (%): C, 80.74; H, 6.88; N, 7.48.

3. Results and discussion

3.1. Solubility and thermal stability

Since introducing the flexible long-chain alkyl into the benzene ring, polymer PPV-BD has a good solubility in polar solvents such as chloroform, tetrahy-

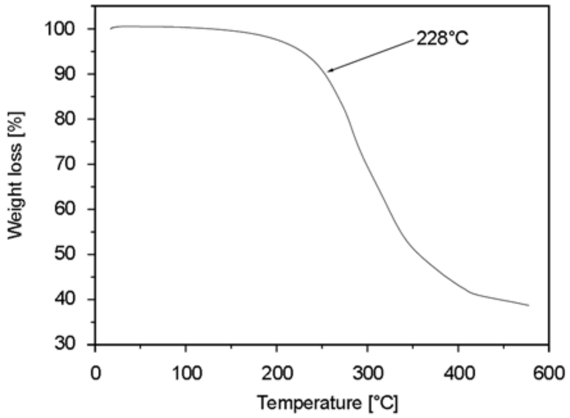

Figure 6. TGA curve of PPV-BD

drofuran and 1,2-dichlorobenzene, and the maximum solubility in chloroform is about 27 mg/mL. Figure 6 shows the TGA traces of polymer PPV-BD. The polymer showed almost no mass loss at a low temperature, but exhibited a weight loss of approximately 5% at 228°C. Hence, it can be concluded that the polymer PPV-BD has good thermal stability in a nitrogen atmosphere, which is suitable for application in optoelectronic devices.

3.2. Absorption and fluorescence properties

In order to investigate the relationships between the thickness and fluorescent performance, different thickness of polymer films were chosen to test their fluorescence properties by photoluminescence spectroscopy. The different thickness of polymer films were prepared by dissolving a certain mass of PPV-BD in chloroform to get different concentration samples (a: 5 mg/mL, b: 10 mg/mL, c: 15 mg/mL, d: 20 mg/mL, e: 27 mg/mL). Different thickness of polymer thin-films were deposited on quartz with a KW-4A spin coater (Institute of Microelectronics of Chinese Academy of Science, China) at a spin rate of 800 rpm using the above solutions, and placed under vacuum overnight before test. Figure 7 is the PL emission spectra of different thickness of PPV-BD films. It can be seen from the Figure 7, with the concentration of PPV-BD increasing, the maximum PL wavelength is red-shifting gradually. The maximum PL wavelength of PPV-BD film (625 nm) prepared from the maximum concentration (27 mg/mL) shows the largest red-shifting which red shift about 10 nm compared to that of PPV-BD film (615 nm) prepared from minimum concentration (5 mg/mL). Perhaps, with the solution concentration increasing, the thickness of film is increased accordingly, the thicker film will lead to a better π-π* stacking, therefore, presenting a larger red-shifting.

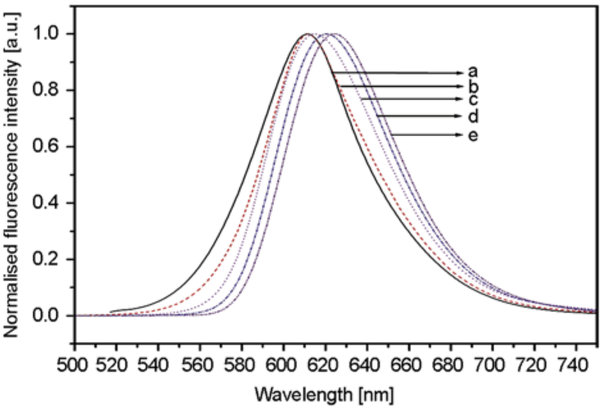

Figure 7. PL emission spectra of different thickness of PPV-BD films (a: 5 mg/mL, b: 10 mg/mL, c: 15 mg/mL, d: 20 mg/mL, e: 27 mg/mL)

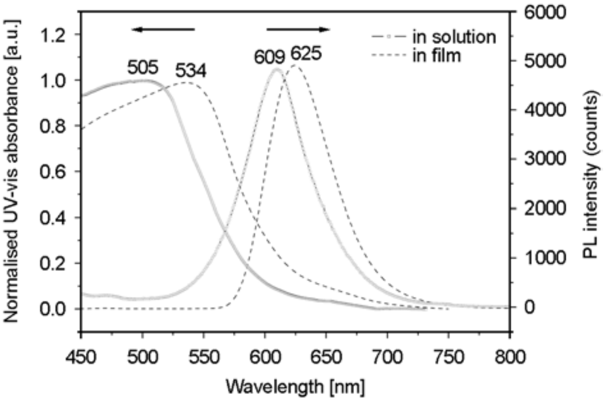

Figure 8. UV-vis spectra and PL-emission spectra (Ex: 350 nm) of PPV-BD in $CHCl_3$ and in film

The photophysical characteristic of PPV-BD was investigated by UV-vis spectroscopy and photoluminescence spectroscopy in dilute chloroform solution (0.035 mg/mL) and in film (prepared from 27 mg/mL solution) on quartz, respectively. The UV-vis absorption spectra and photoluminescence emission spectra of polymer PPV-BD in $CHCl_3$ and film are shown in Figure 8. Optical data of the polymer PPV-BD and MEH-PPV are summarized in Table 1. Figure 9 shows the molecular structure of MEH-PPV.

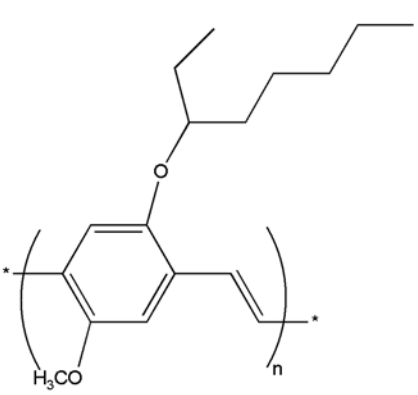

Figure 9. Molecular structure of MEH-PPV

Table 1. Optical data of polymers PPV-BD and MEH-PPV

Polymer	UV-vis [nm]				PL-em [nm]		E_g^{opt} [eV]	
	$\lambda_{max}(CHCl_3)$	λ_{max}(film)	$\lambda_{onset}(CHCl_3)$	λ_{onset}(film)	$\lambda_{max}(CHCl_3)$	λ_{max}(film)	$CHCl_3$	film
PPV-BD	505	534	609	625	609	625	2.03	1.98
MEH-PPV[25]	490	503	565	590	–	–	2.20	2.12

It can be seen from Figure 8 that polymer PPV-BD presents a slight red-shifting in their principal absorption and fluorescence bands in thin films relative to in solution. It may be attribute to conformational preferences in thin films that the interpolymer interactions is increased, forming a π-stacking of polymer chains [29, 30].

Table 1 shows the maxima of absorption at long wavelength of polymers PPV-BD and MEH-PPV in chloroform at 505 and 490 nm respectively, and 534 and 503 nm in film respectively. The results show that the absorption maximum of PPV-BD exhibits a 29 nm red-shifting in $CHCl_3$ and 31 nm red-shifting in film compared to MEH-PPV, respectively. Furthermore, the absorption spectrum onset of PPV-BD in chloroform is at about 609 nm, shifting to a longer wavelength compared to MEH-PPV (λ_{onset} = 565 nm, E_g^{opt} = 2.20 eV), corresponding to an optical band-gap (E_g^{opt}) of 2.03 eV. As anticipated, the alternation of electron-rich alkoxy substituted aromatic and electron-deficient quinoxaline units along conjugated backbone results in a decrease of the band-gap. The results show that PPV copolymers containing electron-acceptor unit quinoxaline can lower the band-gap.

As described above, the red-shifting of the UV-vis peak in film (Figure 8) suggests that PPV-BD assumes a self-assembled stacked structure in the solid state [31]. The XRD pattern of PPV-BD shown in Figure 10 supports this view. According to the Bragg equation (Equation (1)):

$$2d\sin\theta = n\lambda \qquad (1)$$

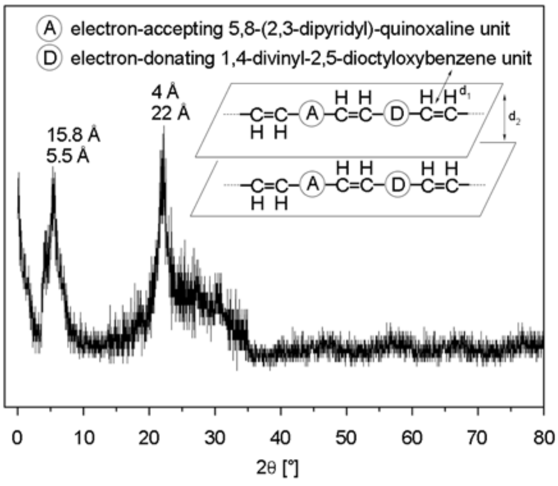

Figure 10. XRD pattern of PPV-BD. The inset is a diagrammatic drawing of PPV-BD film

The peak with a *d* value of 15.8 Å is considered to correspond to the distance between the main chains separated by the octyloxy group (d_1); the peak with a *d* value of 4.0 Å is considered to correspond to the face-to-face distance between coplanar polymer chains (d_2).

3.3. Potoinduced Charge Transfer studies

3.3.1. PCT in polymer solar cell

Polymer PPV-BD and fullerene C_{60} (PPV-BD/C_{60} ~approximately 1/4, w/w) were dissolved in 1, 2-dichlorobenzene. Polymer thin films were deposited on quartz with a KW-4A spin coater at a spin rate of 1000 rpm by using the above solution. The PL-emission spectra are shown in Figure 11. It shows that when the polymer PPV-BD is blended with fullerene C_{60}, the fluorescence of PPV-BD almost completely quenched. According to the quenching rate formula (Equation (2)):

$$Q\% = \frac{f_a - f_b}{f_a}\cdot 100 \qquad (2)$$

where, $Q\%$ denotes quenching rate, f_a denotes fluorescence intensity when the quencher mass is zero, f_b denotes the fluorescence intensity when a certain mass of quencher is added to the polymer. Thus, we can get the final fluorescence quenching rate of PPV-BD is 99.8% (PPV-BD/C_{60} ~ 1/4, w/w). Because energy (exciton) transfer from the polymer to C_{60} is highly endergonic. We attribute the fluorescence quenching to electron transfer, although a contribution from increased nonradiative decay (e.g., intersysterm crossing) cannot be ruled out. From these results, it can be referred that the polymer PPV-BD may be a good candidate photovoltaic material for PSCs.

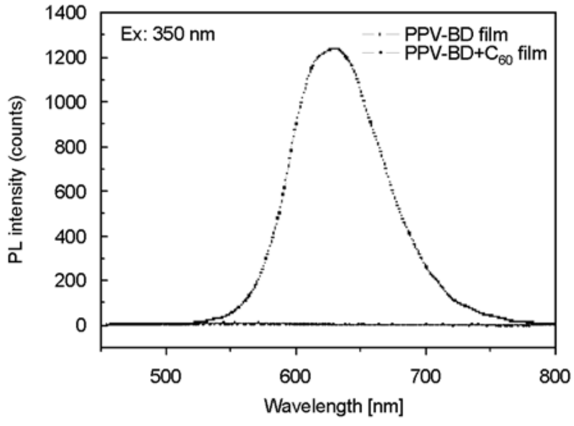

Figure 11. PL-emission spectra of PPV-BD and PPV-BD/C_{60} (approximately 1/4, w/w) in films

3.3.2. PCT application in TNT Detection

A mixed solution was prepared by dissolving 1.4 mg PPV-BD in 14 mL chloroform, then dividing it into seven parts to get samples (0.1 mg/mL). Each part of the PPV-BD solution was mixed with a chloroform solution of TNT (0, 5, 50, 300, 500, 1000, 4000 ppm), respectively. The fluorescent properties of the mixtures were recorded immediately by fluorescence spectra at excitation wavelengths of 350 nm.

Figure 12 shows the PL-emission spectra of PPV-BD in chloroform solution upon successively adding different concentrations of TNT solution. The intensity of the fluorescence decreased gradually as the concentration of TNT increased, which may be attributed to the destruction of the polymer conjugation upon interacting with TNT molecules. As we know, one property of nitroaromatics which may be exploited in detection schemes is the electron accepting capability. Substitution of the electron-withdrawing nitro groups on the aromatic ring lowers the energy of the empty π* orbitals, thereby making these compounds good electron acceptors. Conjugated polymers are electron donors. Donor ability is further enhanced in their delocalized π* excited states. Excited state delocalization is important because exciton migration increases the frequency of interaction with a bound quencher, which contributes to enhanced detection sensitivity. Fluorescent conjugated polymers have therefore been applied to the detection of nitroaromatic explosives. As it can be seen from Figure 12, when the concentration of TNT was only 5 ppm, the fluorescence quenching rate of PPV-BD was 10.66%. When the concentration of TNT was 50 ppm, and the fluorescence quenching rate of PPV-BD was 37.77%. When the concentration of TNT was 4000 ppm, the fluorescence quenching rate of PPV-BD was nearly 100%. Thus, it can be concluded that the polymer PPV-BD may also be suitable for using as a TNT chemosensor material.

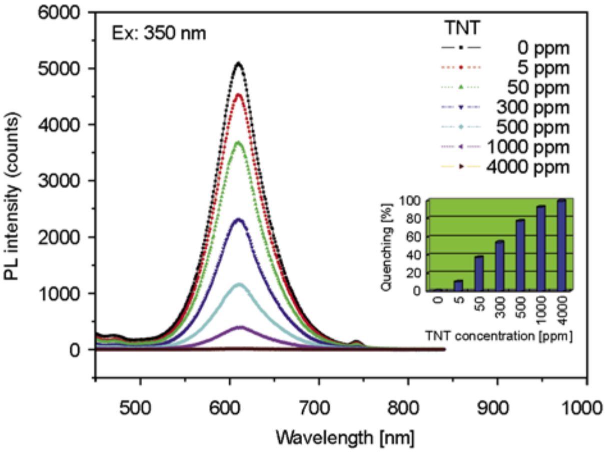

Figure 12. PL-emission spectra of PPV-BD with different TNT concentration solutions

In short, whether conjugated polymer PPV-BD blending with C_{60} or TNT, fluorescence quenching is often achieved through an electron-transfer donor-acceptor mechanism, as depicted in Figure 13.

3.4. Electrochemical properties

Thin film of polymer was drop cast from chloroform (10 mg/mL). The CV of PPV-BD was carried out in acetonitrile at a potential scan rate of 50 mV/s. Saturated calomel electrode (SCE) served as the reference electrode. It was calibrated with ferrocene (E_{Fc/Fc^+} = 0.5 V vs. SCE). HOMO and LUMO energy levels were estimated here on the basis of the reference energy level of ferrocene (4.4 eV below the vacuum) [33] according the Equation (3):

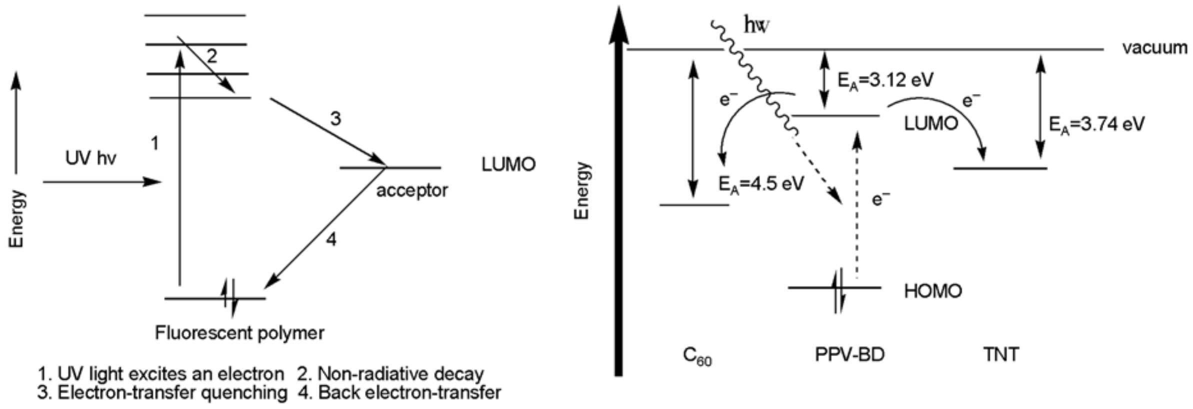

Figure 13. Electron-transfer fluorescence quenching [32]

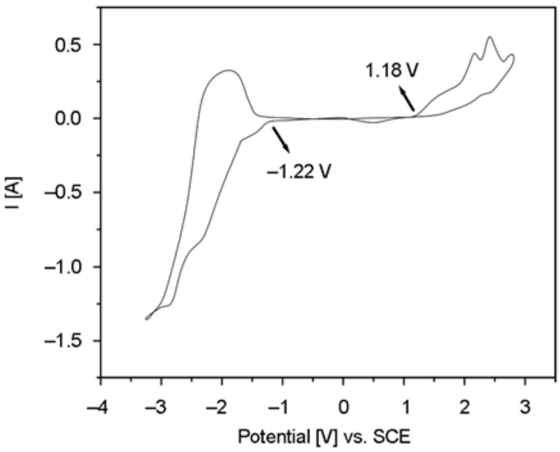

Figure 14. Cylic voltammograms of PPV-BD

$$E^{\mathrm{HOMO/LUMO}} = [-(E_{\mathrm{onset(vs.SCE)}} - E_{\mathrm{onset(Fc/Fc^{+}vs.SCE)}})] - 4.4\ \mathrm{eV} \quad (3)$$

Figure 14 shows the cyclic voltammograms (CV) of polymer PPV-BD. It shows that polymer PPV-BD reduction and oxidation are irreversible. The oxidations was observed with an onset potential at about 1.18 V versus SCE and the reductions was observed with an onset potential at about –1.22 V versus SCE. The HOMO and LUMO energy levels were estimated to be –5.08 and –2.68 eV. There is an obvious difference between LUMO of polymer PPV-BD and C_{60} (–4.5 eV) or TNT (–3.74 eV) which makes an effective charge transfer possible between polymer PPV-BD and C_{60} or TNT. The CV band-gap of polymer PPV-BD is 2.40 eV is slightly larger than its optical band. The discrepancy of values lies within the range of errors, and this discrepancy is probably due to interface barrier for charge injection [34, 35].

4. Conclusions

A new conjugated polymer with donor-accepter architectures based on alternating 1,4-divinyl-2,5-dioctyloxybenzene and 5,8-(2,3-dipyridyl)-quinoxaline was synthesized successfully. The polymer is thermostable, and it has common film-forming ability. The band-gap of PPV-BD was estimated to 1.98 eV (E_g^{opt}), which exhibited a reduction compared to MEH-PPV. Similarly, it showed a red-shifted UV-vis absorption peak in comparison to MEH-PPV. The results show that introduction of quinoxaline units leads to a reduction of the band-gap of poly(p-phenylenevinylenes) (PPVs) copolymers. Its PCT applications in PSCs and TNT detection were studied respectively, and the results indicated that this polymer might be a good candidate material for PSCs or detecting TNT in solution.

Acknowledgements

Financial supported by the 'Doctorate Foundation of Northwestern Polytechnical University (Grant No.: CX201118), National Program on Key Basic Research Project (973 Program) (Grant No.: 2010CB635111)' is acknowledged.

References

[1] Burroughes J. H., Bradley D. D. C., Brown A. R., Marks R. N., Mackay K., Friend R. H., Burns P. L., Holmes A. B.: Light-emitting diodes based on conjugated polymers. Nature, **347**, 539–541 (1990).
DOI: 10.1038/347539a0

[2] Gross M., Müller D., Nothofer H-G., Scherf U., Neher D., Bräuchle C., Meerholz K.: Improving the performance of doped π-conjugated polymers for use in organic light-emitting diodes. Nature, **405**, 661–665 (2000).
DOI: 10.1038/35015037

[3] Müller C., Falcou A., Reckefuss N., Rojahn M., Wiederhirn V., Rudati P., Frohne H., Nuyken O., Becker H., Meerholz K.: Multi-colour organic light-emitting displays by solution processing. Nature, **421**, 829–833 (2003).
DOI: 10.1038/nature01390

[4] Sirringhaus H., Tessler N., Friend R. H.: Integrated optoelectronic devices based on conjugated polymers. Science, **280**, 1741–1744 (1998).
DOI: 10.1126/science.280.5370.1741

[5] Coakley K. M., McGehee M. D.: Conjugated polymer photovoltaic cells. Chemistry of Materials, **16**, 4533–4542 (2004).
DOI: 10.1021/cm049654n

[6] Chen L., McBranch D. W., Wang H-L., Helgeson R., Wudl F., Whitten D. G.: Highly sensitive biological and chemical sensors based on reversible fluorescence quenching in a conjugated polymer. Proceedings of the National Academy of Sciences, **96**, 12287–12292 (1999).
DOI: 10.1073/pnas.96.22.12287

[7] Yu G., Wang J., McElvain J., Heeger A.: Large-area, full-color image sensors made with semiconducting polymers. Advanced Materials, **10**, 1431–1434 (1998).
DOI: 10.1002/(SICI)1521-4095(199812)10:17<1431::AID-ADMA1431>3.0.CO;2-4

[8] Chochos C. L., Choulis S. A.: How the structural deviations on the backbone of conjugated polymers influence their optoelectronic properties and photovoltaic performance. Progress in Polymer Science, **36**, 1326–1414 (2011).
DOI: 10.1016/j.progpolymsci.2011.04.003

[9] Kietzke T., Hörhold H-H., Neher D.: Efficient polymer solar cells based on M3EH–PPV. Chemistry of Materials, **17**, 6532–6537 (2005).
DOI: 10.1021/cm050148n

[10] Wang Z., Qu S., Zeng X., Liu J., Zhang C., Shi M., Tan F., Wang Z.: The synthesis of MDMO-PPV capped PbS nanorods and their application in solar cells. Current Applied Physics, **9**, 1175–1179 (2009).
DOI: 10.1016/j.cap.2009.01.008

[11] Kim S. C., Naidu B. V. K., Lee S-K., Shin W-S., Jin S-H., Jung S-J., Cho Y-R., Shim J-M., Lee J. K., Lee J. W., Kim J. H., Gal Y-S.: Synthesis and photovoltaic properties of novel PPV-derivatives tethered with spirobifluorene unit for polymer solar cells. Solar Energy Materials and Solar Cells, **91**, 460–466 (2007).
DOI: 10.1016/j.solmat.2006.10.014

[12] Shen P., Ding T., Huang H., Zhao B., Tan S.: Poly(*p*-phenylenevinylene) derivatives with conjugated thiophene side chains: Synthesis, photophysics and photovoltaics. Synthetic Metals, **160**, 1291–1298 (2010).
DOI: 10.1016/j.synthmet.2010.03.024

[13] Zou Y., Hou J., Yang C., Li Y.: A novel n-type conjugated polymer DOCN-PPV: Synthesis, optical, and electrochemical properties. Macromolecules, **39**, 8889–8891 (2006).
DOI: 10.1021/ma0626057

[14] Yu G., Gao J., Hummelen J. C., Wudl F., Heeger A. J.: Polymer photovoltaic cells: Enhanced efficiencies via a network of internal donor-acceptor heterojunctions. Science, **270**, 1789–1791 (1995).
DOI: 10.1126/science.270.5243.1789

[15] Shaheen S. E., Brabec C. J., Sariciftci N. S., Padinger F., Fromhertz T., Hummelen J. C.: 2.5% efficient organic plastic solar cells. Applied Physics Letters, **78**, 841–843 (2001).
DOI: 10.1063/1.1345834

[16] Roncali J.: Synthetic principles for bandgap control in linear π-conjugated systems. Chemical Reviews, **97**, 173–206 (1997).
DOI: 10.1021/cr950257t

[17] Cui Y., Zhang X., Jenekhe S. A.: Thiophene-linked polyphenylquinoxaline: A new electron transport conjugated polymer for electroluminescent devices. Macromolecules, **32**, 3824–3828 (1999).
DOI: 10.1021/ma9901994

[18] Agrawal A. K., Jenekhe S. A.: Electrochemical properties and electronic structures of conjugated polyquinolines and polyanthrazolines. Chemistry of Materials, **8**, 579–589 (1996)
DOI: 10.1021/cm9504753

[19] Zhang Q. T., Tour J. M.: Alternating donor/acceptor repeat units in polythiophenes. Intramolecular charge transfer for reducing band gaps in fully substituted conjugated polymers. Journal of the American Chemical Society, **120**, 5355–5362 (1998).
DOI: 10.1021/ja972373e

[20] Zhang Q. T., Tour J. M.: Low optical bandgap polythiophenes by an alternating donor/acceptor repeat unit strategy. Journal of the American Chemical Society, **119**, 5065–5066 (1997).
DOI: 10.1021/ja9640399

[21] Anferov V. P., Mozjoukhine G. V., Fisher R.: Pulsed spectrometer for nuclear quadrupole resonance for remote detection of nitrogen in explosives. Review of Scientific Instruments, **71**, 1656–1659 (2000).
DOI: 10.1063/1.1150514

[22] Toal S. J., Trogler W. C.: Polymer sensors for nitroaromatic explosives detection. Journal of Materials Chemistry, **16**, 2871–2883 (2006).
DOI: 10.1039/B517953J

[23] Wang D., Gaylord B. S., Bazan G. C.: Fluorescein provides a resonance gate for FRET from conjugated polymers to DNA intercalated dyes. Journal of the American Chemical Society, **126**, 5446–5451 (2004).
DOI: 10.1021/ja035550m

[24] Ashraf R. S., Hoppe H., Shahid M., Gobsch G., Sensfuss S., Klemm E.: Synthesis and properties of fluorene-based polyheteroarylenes for photovoltaic devices. Journal of Polymer Science Part A: Polymer Chemistry, **44**, 6952–6961 (2006).
DOI: 10.1002/pola.21645

[25] Thompson B. C., Kim Y-G., Reynolds J. R.: Spectral broadening in MEH-PPV:PCBM-based photovoltaic devices via blending with a narrow band gap cyanovinylene–dioxythiophene polymer. Macromolecules, **38**, 5359–5362 (2005).
DOI: 10.1021/ma0505934

[26] Lu S.: Design, synthesis and performance of organic and polymeric photovoltaic materials (in Chinese). Zhejiang University, Hangzhou (2004).

[27] McKean D. D., Parrinello G., Renaldo A. F., Stille J. K.: Synthesis of functionalized styrenes via palladium-catalyzed coupling of aryl bromides with vinyl tin reagents. The Journal of Organic Chemistry, **52**, 422–424 (1987).
DOI: 10.1021/jo00379a020

[28] Ashraf P. R. S.: Band gap engineering of donor-acceptor π-conjugated poly(heteroarylene)s and poly(heteroaryleneethynylene)s. Dr. rer. nat. thesis, Friedrich Schiller University of Jena (2005).

[29] Colladet K., Fourier S., Cleij T. J., Lutsen L., Gelan J., Vanderzande D.: Low band gap donor–acceptor conjugated polymers toward organic solar cells applications. Macromolecules, **40**, 65–72 (2007).
DOI: 10.1021/ma061760i

[30] Apperloo J. J., Janssen R. A. J., Malenfant P. R. L., Fréchet J. M. J.: Concentration-dependent thermochromism and supramolecular aggregation in solution of triblock copolymers based on lengthy oligothiophene cores and poly(benzyl ether) dendrons. Macromolecules, **33**, 7038–7043 (2000).
DOI: 10.1021/ma000793+

[31] Morikita T., Yamaguchi I., Yamamoto T.: New charge transfer–type π-conjugated poly(aryleneethynylene) containing benzo[2,1,3]thiadiazole as the electron-accepting unit. Advanced Materials, **13**, 1862–1864 (2001).
DOI: 10.1002/1521-4095(200112)13:24<1862::AID-ADMA1862>3.0.CO;2-#

[32] Wu C., Peng H., Jiang Y., McNeill J.: Energy transfer mediated fluorescence from blended conjugated polymer nanoparticles. The Journal of Physical Chemistry B, **110**, 14148–14154 (2006).
DOI: 10.1021/jp0618126

[33] de Leeuw D. M., Simenon M. M. J., Brown A. R., Einerhand R. E. F.: Stability of n-type doped conducting polymers and consequences for polymeric microelectronic devices. Synthetic Metals, **87**, 53–59 (1997).
DOI: 10.1016/S0379-6779(97)80097-5

[34] Chen Z-K., Huang W., Wang L-H., Kang E-T., Chen B. J., Lee C. S., Lee S. T.: A family of electroluminescent silyl-substituted poly(*p*-phenylenevinylene)s: Synthesis, characterization, and structure–property relationships. Macromolecules, **33**, 9015–9025 (2000).
DOI: 10.1021/ma0005670

[35] Janietz S., Bradley D. D. C., Grell M., Giebeler C., Inbasekaran M., Woo E. P.: Electrochemical determination of the ionization potential and electron affinity of poly(9,9-dioctylfluorene). Applied Physics Letters, **73**, 2453–2455 (1998).
DOI: 10.1063/1.122479

eXPRESS Polymer Letters Vol.6, No.6 (2012) 465–475
Available online at www.expresspolymlett.com
DOI: 10.3144/expresspolymlett.2012.49

Preparation and characterization of an aromatic polyester/polyaniline composite and its improved counterpart

C. S. Wu*

Department of Chemical and Biochemical Engineering, Kao Yuan University, Kaohsiung County, Taiwan 82101, Republic of China

Received 31 October 2011; accepted in revised form 28 December 2011

Abstract. Poly(butylene terephthalate) (PBT) composites containing polyaniline (PANI) were prepared using a melt-blending process. Maleic anhydride-grafted PBT (PBT-*g*-MA) and PANI were used to improve the compatibility of PANI within the PBT matrix. PBT-*g*-MA/PANI composites exhibited noticeably superior mechanical properties compared with those of PBT/PANI due to greater compatibility with the added PANI. The antibacterial and antistatic properties of the composites were also evaluated. *Escherichia coli* were chosen as the standard bacteria for determining the antibacterial properties of the composite materials. The PBT-*g*-MA/PANI composites showed markedly enhanced antibacterial and antistatic properties compared to PBT/PANI composites due to the formation of imide bonds from condensation of the anhydride carboxyl acid groups of PBT-*g*-MA with the amino groups of PANI. The optimal level of PANI in the composites was 9 wt%, as excess PANI led to separation of the two organic phases, lowering their compatibility.

Keywords: *polymer composites, poly(butylene terephthalate), polyaniline, antibacterial, antistatic*

1. Introduction

The revolutionary discovery of metallic properties in molecularly doped polyacetylene opened a new field of research: electronically conducting polymers [1]. Conducting polymers, such as polypyrrole, polyaniline, etc., are polymers with electronically conjugated backbones that, when doped, conduct electricity. These materials have recently attracted much attention due to their potential use in many technological applications that could benefit from their unique polymeric and electronic properties [2–4]. Polyaniline (PANI) is important among known electronic conducting polymers. Several simple chemical methods for synthesis of PANI are known. However, PANI's utilization has been limited because most chemically synthesized PANI is difficult to manipulate using normal melt processing techniques. Furthermore, because thin conducting films of PANI are necessary for most applications – such as for electrodes, sensor devices, control of electromagnetic interference, and the dissipation of electrostatic charge – more easily processable PANI-based materials are needed [5–8].

The principal disadvantage of PANI is its poor processability, and for this reason, some of its potential applications have not been fully explored. A reportedly effective method for improving PANI processability is to prepare a core-shell composite using more easily processable polymers for the core material and PANI for the shell material [9–11]. In these kinds of PANI composites, a good balance can be achieved between electrical and mechanical properties. Chen *et al*. [12] found that core-shell particles of poly(butyl acrylate–methyl methacry-

---

*Corresponding author, e-mail: t50008@cc.kyu.edu.tw

late)-polyaniline can be obtained through dispersion of PANI in a bilayer structure of poly(butyl acrylate–methyl methacrylate) latex. Wang and Jing [13] reported a preparation method for polystyrene-polyaniline core-shell structured particles, and they described the properties of their conductive core-shell particles upon incorporation into epoxy-based composites. This study focuses on the effects of functionalized PANI on the electrochemical behavior and conducting properties of poly(butylene terephthalate) (PBT)-based composite materials.

PBT is a thermoplastic, semicrystalline polymer with excellent processability; it has been used widely in structural materials in the electrical, electronics, and automotive industries [14, 15]. The ongoing practical demands for higher performance materials in various advanced industries has led to the development of new PBT-based composites with additional functional properties, such as high electrical conductivity, antibacterial activity and flame retardance [16–18]. Of these properties, antibacterial activity holds particular interest. The potential benefits of self-sterilizing fabrics made with antibacterial PBT fibers include reduced disease transfer among hospital populations and biowarfare protection. Much research has been conducted to extend and develop commercial applications for PBT in high-performance composites using various reinforcing fillers [19, 20].

This study focused on the characterization of composites of PBT-*g*-MA and PANI prepared using an *in situ* polycondensation reaction process. To the best of our knowledge, PANI has not yet been evaluated systematically as a reinforcement material in PBT for the production of antibacterial and antistatic composites.

2. Experimental

2.1. Materials

PBT resins (PBT-1100) were obtained from Chang Chun Corporation (Taiwan). Analytical reagent-grade aniline (purity 99.9%), ammonium persulfate (SAN, 95%), ammonium peroxydisulftate (APS, 99.9%), benzoyl peroxide, and maleic anhydride (MA) were obtained from Sigma–Aldrich Co. (USA). The MA was purified prior to use by recrystallization from chloroform. Benzoyl peroxide was used as a polymerization initiator and was purified by dissolution in chloroform and reprecipitation in methanol. Other reagents were purified using conventional methods.

2.2. Grafting reaction and grafting percentage

A mixture of MA and benzoyl peroxide was added in four equal portions at 2 min intervals to molten PBT to allow grafting to take place and to form MA-grafted PBT (PBT-*g*-MA). The reactions were performed in a nitrogen atmosphere at 45±2°C. Preliminary experiments indicated that the reaction equilibrium was attained in less than 12 h. Thus, reactions were allowed to progress for 12 h under stirring at a rotor speed of 60 rpm. The resultant product (4 g) was dissolved in 200 mL of refluxing trifluoroacetic acid/deuterated chloroform ($CF_3COOH/CDCl_3$) solution (20:80, v/v) at 40±2°C, and the solution was filtered through several layers of cheesecloth. The $CF_3COOH/CDCl_3$-soluble product in the filtrate was extracted five times using 600 mL of cold acetone per extraction. The MA loading of the $CF_3COOH/CDCl_3$-soluble polymer was determined by titration and expressed as a grafting percentage. Approximately 2 g of copolymer were heated for 2 h in 200 mL of refluxing $CF_3COOH/CDCl_3$ solution. This solution was then titrated immediately with 0.03 N ethanolic potassium hydroxide (KOH), which had been standardized against a solution of potassium hydrogen phthalate, with a phenolphthalein indicator. The acid number and the grafting percentage of the PBT-*g*-MA were then calculated using the following Equations (1) and (2) [21]:

$$\text{Acid number [mg KOH/g]} = \frac{V_{\text{KOH}}[\text{mL}]\cdot C_{\text{KOH}}[\text{N}]\cdot 56.1}{\text{polymer}[\text{g}]} \tag{1}$$

$$\text{Grafting percentage [\%]} = \frac{\text{Acid number}\cdot 98.1}{561}\cdot 100\% \tag{2}$$

At benzoyl peroxide and MA loadings of 0.3 and 10 wt%, respectively, the grafting percentage was 1.06 wt%.

2.3. Synthesis of PANI

The syntheses of PANI and PBT and the preparation of the PBT-PANI composite materials are illus-

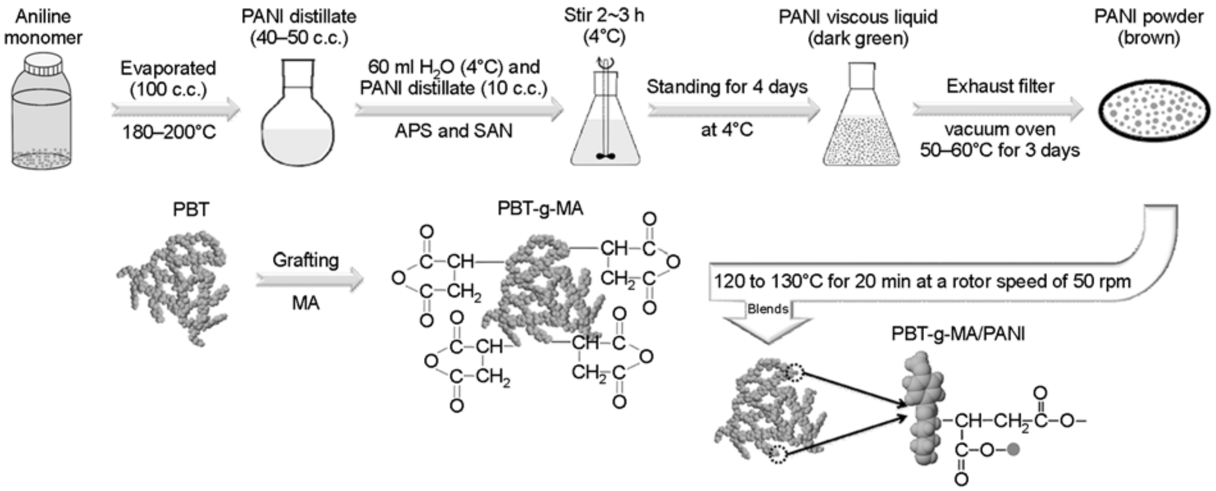

Figure 1. Reaction scheme for the modification of PBT, synthesis of PANI, and the preparation of composite materials

trated in Figure 1. First, a vacuum distillation unit was used to distill and purify 100 mL of aniline monomer to obtain 40–50 mL of purified aniline monomer, and then 10 mL of aniline monomer were drawn by pipette and injected into a conical flask containing 60 mL of deionized water. Then, 5.74 g of APS (oxidizer) and 4.76 g of SAN (monomer) were added to the flask. The flask was placed in an ice bath, the contents were mixed for 2–3 h, and then the flask was placed in a cooling water circulation device and maintained below 4°C for 4 days to obtain a green-black viscous liquid. This viscous liquid reaction product was then suction filtered, and the product was washed with deionized water until the wash liquid was clear. The washed product was then placed in a vacuum drying oven, dried at 50–60°C, and taken out 3 days later. Brown PANI powder was obtained.

2.4. Preparation of composite materials

The composites were prepared using a ‘Plastograph’ 200 Nm W50EHT mixer with a blade-type rotor (C.W. Brabender Instruments, Inc., Hackensack, NJ). Prior to composite formation, PANI samples were dried in a vacuum oven at 50–60°C for 2 days. Composites of PBT/PANI or PBT-*g*-MA/PANI were prepared with 0, 3, 6, 9, 12, and 15 wt% PANI filler. Approximately 40 g of the composite mixture (polymer and filler) were mixed at 50 rpm and 220–230°C for 20 min with an antimony trioxide (Sb_2O_3) catalyst. Composite mixtures of PBT/PANI or PBT-*g*-MA/PANI were placed in a vacuum oven at 70–80°C for 24 h. Standard specimens were prepared by pressing the hybrid composites into 1 mm-thick plates using a hydraulic press at 230°C and 100 atm. Following pressing, the plates were placed in a dryer for cooling. Prior to characterization, the specimens were conditioned for 24 h at a relative humidity of 50±5%.

2.5. Characterization of hybrid composites

Fourier transform infrared spectrometry (FTIR; FTS-7PC; Bio-Rad, Hercules, CA) was used to investigate the grafting reaction of MA onto PBT and to verify ester bond formation between the PANI phase and the PBT matrix. Samples subjected to FTIR analysis were ground into fine powders in a milling machine and pressed into pellets with KBr. Solid-state ^{13}C nuclear magnetic resonance (NMR) analyses were performed with an AMX 400 ^{13}C NMR spectrometer (Bruker, Madison, WI) at 100 MHz. ^{13}C NMR spectra were acquired under cross-polarization and magic angle sample spinning. Power decoupling was employed with a 90° pulse and 4 s cycle time. An Instron mechanical tester (Model LLOYD, LR5K type) was used to measure the tensile strength and the elongation at break, in accordance with ASTM D638. Test samples were prepared in a hydrolytic press at 180°C and conditioned at 50±5% relative humidity for 24 h before making measurements. Measurements were made using a crosshead speed of 20 mm/min. Five measurements were performed for each sample, and the results were averaged to obtain a mean value. A thin film of each composite was created using a hydrolytic press and treated with hot water at 80°C for 24 h prior to being coated with gold. The surface morphology of these thin films was observed using scanning electron microscopy (SEM; model S-1400, Hitachi Microscopy, Tokyo, Japan). Electrical resistivity was measured directly on laminated films (0.1 mm thick) using an Ohm-Stat RT-1000 resistivity meter.

2.6. Determination of antibacterial properties

The *Escherichia coli* (BCRC 10239) were obtained from the Bioresource Collection and Research Center (BCRC; Hsinchu, Taiwan) and maintained in a nutrient broth (NB) medium (3 g beef extract and 5 g peptone in 1 L of distilled water, pH 7.0). Nutrient agar was produced by the addition of 15 g of agar to 1 L of NB. The bacteria were stored at −20°C in an NB medium containing 60% glycerol. Prior to testing, 150 mL of NB medium were inoculated with 10 μL of preserved bacteria, and the culture was grown aerobically at 37°C. After overnight incubation, 3 mL of the culture were transferred to fresh NB medium and maintained at 37°C while shaking at 120 rpm for 18 h. Wells were constructed (3.00 cm diameter, 0.05 cm thick) on the surface of each composite sample ($5.00\times5.00\times0.005$ cm, 0.05 cm thick) to hold the bacterial suspension in contact with the sample. A 0.01 mL aliquot of bacterial suspension ($1.26\cdot10^6$ colony-forming units [CFUs]/mL) was placed on the surface of each sample and covered with a sterile polyethylene film ($4.00\times4.00\times0.005$ cm; Figure 2a). The samples were incubated at 37±1°C at a relative humidity of ~90%. Following incubation for 24 h, the number of CFUs of *E. coli* was determined by direct plate counting. Figure 2b shows images of the *E. coli* colonies from the PBT-*g*-MA and PBT-*g*-MA/PANI (9 wt%) samples that had been exposed to the composite for various time periods.

The Japanese Industrial Standard JIS L 1902:1998 is a method typically used to estimate the antibacterial activity of textiles and can also be applied to determine the antibacterial activity of PBT and PANI composites. This method determines the antibacterial index (ABI) and kill-bacterial index (KBI) according to the Equations (3) and (4):

$$\text{ABI} = \log B - \log C \qquad (3)$$

$$\text{KBI} = \log A - \log C \qquad (4)$$

where *A* represents the number of bacteria that are recovered from the inoculated untreated sample (native PBT or PBT-*g*-MA) immediately following inoculation, *B* is the number of bacteria remaining in the inoculated untreated sample after 18 h, and *C* is the number of the bacteria remaining in the inoculated treated sample after 18 h. According to the antibacterial standard of the Japanese Association for the Functional Evaluation of Textiles, an ABI value greater than 2.2 indicates bacterial inhibition, while a KBI greater than 0 indicates a bactericidal effect.

2.7. Bacteria inhibition tests

E. coli bacteria were activated in the liquid medium, and the activated bacteria were moved to new medium for 18 h cultivation. The samples (100 μL) were then dropped into the culture dish. Next, a sterilized triangular glass rod was used to spread the bacteria in the dish. In addition, the specimen (about 1.40 cm diameter, 0.03 cm thick) was wiped with 75% alcohol for sterilization and placed into a culture dish with clippers. The culture dish edges were sealed using sealing membrane and placed inside an

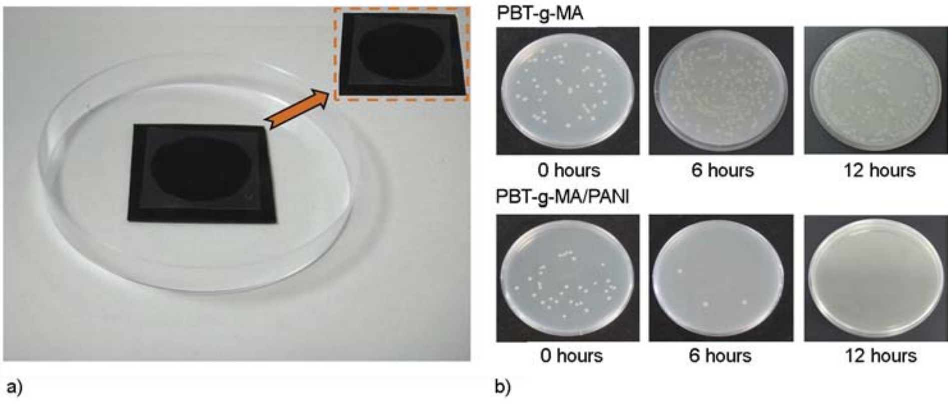

a)

b)

Figure 2. (a) Images of composite samples loaded with a fixed volume (0.1 mL) of *E. coli* for the evaluation of antibacterial activity. (b) *E. coli* exposed to PBT-*g*-MA or PBT-*g*-MA/PANI (9 wt%) over time.

incubator at 30°C for 24 h cultivation to observe the bacterial inhibitory effects.

3. Results and discussion

3.1. FTIR/NMR analyses

The FTIR spectra of unmodified PBT and of PBT-*g*-MA are shown in Figure 3a and 3b, respectively. The characteristic transitions of PBT at 3300~3700, 1700~1760, and 500~1500 cm^{-1} appeared in the spectra of both polymers [22], with two extra shoulders observed at 1786 and 1857 cm^{-1} in the modified PBT spectrum. These extra features are characteristic of anhydride carboxyl groups. Similar results have been reported previously [23]. The shoulders represent free acid in the modified polymer and thus denote the successful grafting of MA onto PBT. In the composite PBT/PANI (9 wt%), the N−H stretching vibration peak at 3336 cm^{-1} intensified (Figure 3c) due to contributions from the −NH group of PANI. The FTIR spectrum of the PBT-*g*-MA/PANI (9 wt%) composite in Figure 3d revealed a peak at 1717 cm^{-1}, and a new peak at 3198 cm^{-1} was observed. This new peak was assigned to the imide stretching vibration of a copolymer formed via condensation and imide formation between the MA groups of PBT-*g*-MA and the amino groups of PANI [24]. The characteristic imide stretching vibration peak was not present in the FTIR spectrum of the PBT/PANI (9 wt%) composite (Figure 3c). Typically, the FTIR spectrum of PANI exhibits peaks in the ranges of 3100~3500 cm^{-1} and 1000~1700 cm^{-1} [25].

Further evidence for imide formation was provided by ^{13}C NMR spectroscopy. The ^{13}C NMR spectrum of neat PBT (Figure 4a) was similar to that reported by Jansen *et al*. [26] and showed five peaks: (1) δ = 170.3 ppm; (2) δ = 134.3 ppm; (3) δ = 129.6 ppm; (4) δ = 66.9 ppm; and (5) δ = 27.8 ppm. Relative to

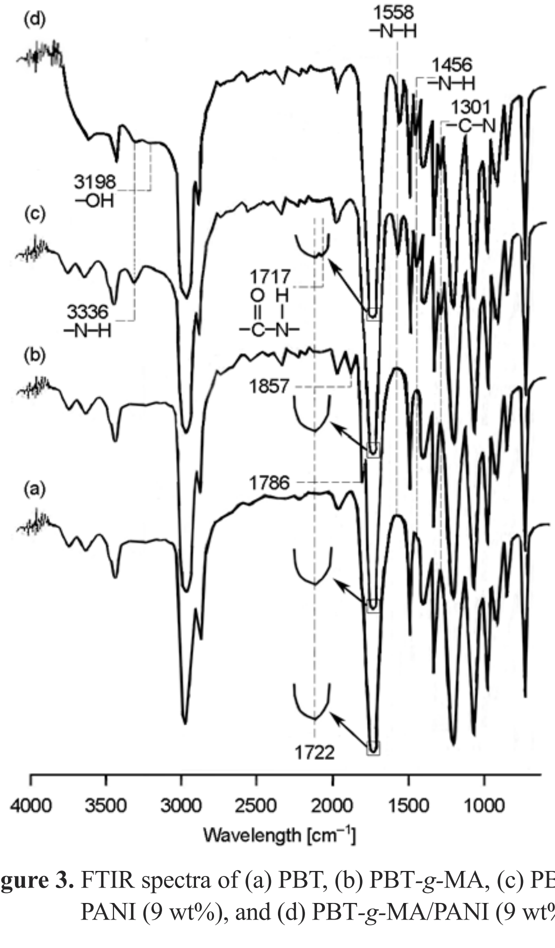

Figure 3. FTIR spectra of (a) PBT, (b) PBT-*g*-MA, (c) PBT/PANI (9 wt%), and (d) PBT-*g*-MA/PANI (9 wt%)

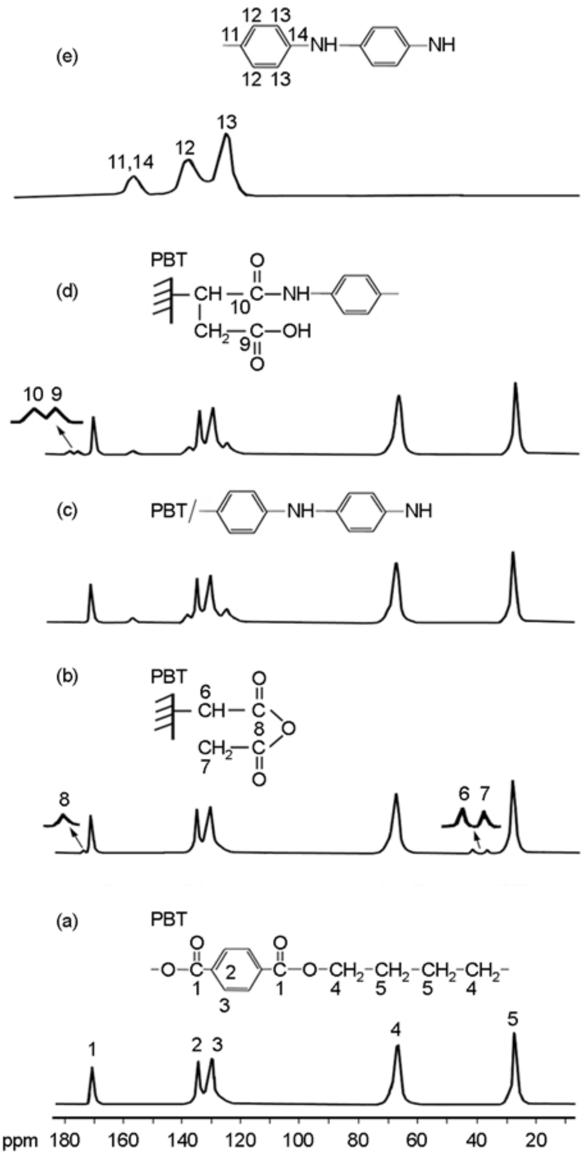

Figure 4. ^{13}C solid-state NMR spectra of (a) PBT, (b) PBT-*g*-MA, (c) PBT/PANI (9 wt%), (d) PBT-*g*-MA/PANI (9 wt%), and (e) PANI

that of neat PBT, the ^{13}C NMR spectrum of PBT-*g*-MA (Figure 4b) contained three additional peaks: (6) δ = 36.1 ppm, (7) δ = 42.6 ppm, and (8) δ = 172.1 ppm. These peaks confirmed the grafting of MA onto PBT. The ^{13}C NMR spectrum of PBT/PANI, shown in Figure 4c, also exhibited peaks that were not observed in neat PBT and corresponded to aromatic carbon atoms in the PANI ((Figure 4e) (11), (14) δ = 157.9 ppm; (12) δ = 137.8 ppm; (13) δ = 123.2 ppm). Peaks (9) and (10) (Figure 4d), originating from the reaction between the MA groups of PBT-*g*-MA and the amino groups of PANI, were found at δ = 175.6 ppm and δ = 177.1 ppm, respectively. These results, combined with the presence of FTIR peaks at 1717 and 3336 cm^{-1}, provide further evidence of imide group formation via condensation of PBT-*g*-MA with PANI.

3.2. Hybrid morphology

The morphology of the PANI and polymer composites can be directly related to their electrical properties. In general, good dispersion of PANI throughout the polymer matrix, effective functionalization of PANI, and strong interfacial adhesion between the two phases is required to obtain a composite material with satisfactory electrical properties. In the current study, PANI may be thought of as a dispersed phase within a PBT or PBT-*g*-MA matrix. To evaluate the composite morphology, SEM was employed to examine tensile fractures in the surfaces of PBT/PANI (9 wt%) and PBT-*g*-MA/PANI (9 wt%) samples. The SEM microphotographs of PBT/PANI (9 wt%) in Figure 5a indicated that the PANI in this composite tended to agglomerate into bundles and was unevenly distributed in the matrix. This poor dispersion was due to the formation of hydrogen bonds between PANI and the disparate hydrophilicities of PBT and PANI. Poor wetting in these composites was also noted (Figure 5a) and was attributed to the large difference in the surface energies of the PANI and the polymer matrix [27].

In contrast, the PBT-*g*-MA/PANI (9 wt%) microphotographs presented in Figure 5b indicated a more homogeneous dispersion with improved wetting of PANI in the PBT-*g*-MA matrix, as indicated by the complete coverage of PBT-*g*-MA on PANI and the removal of both materials when PANI was pulled from the bulk. This improved interfacial adhesion was attributed to the similar hydrophilicity of the two components, which prevented hydrogen bonding in PANI.

3.3. Mechanical properties

Figure 6 shows the variation in tensile strength at break with PANI content for PBT/PANI and PBT-*g*-MA/PANI composites. The tensile strength of neat PBT decreased when it was grafted with MA. In PBT/PANI composites, the effect of PANI con-

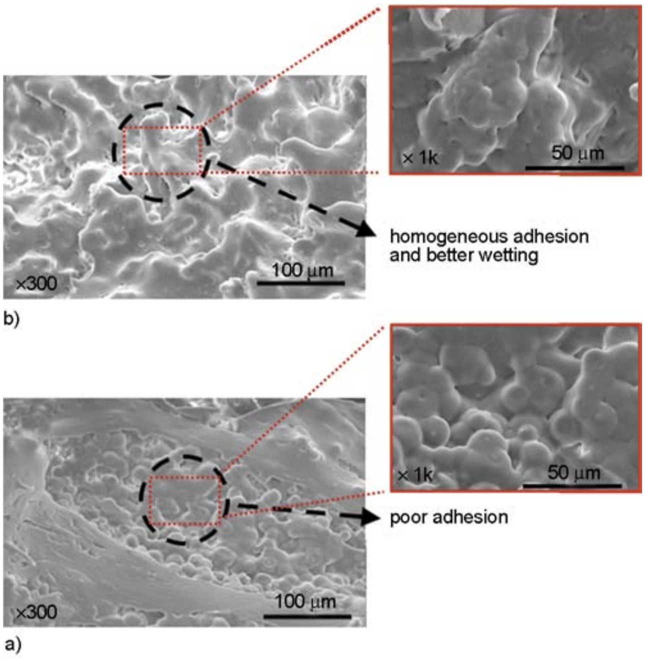

Figure 5. SEM micrographs showing the distribution and adhesion of PANI in (a) PBT/PANI (9 wt%) and (b) PBT-*g*-MA/PANI (9 wt%) composites

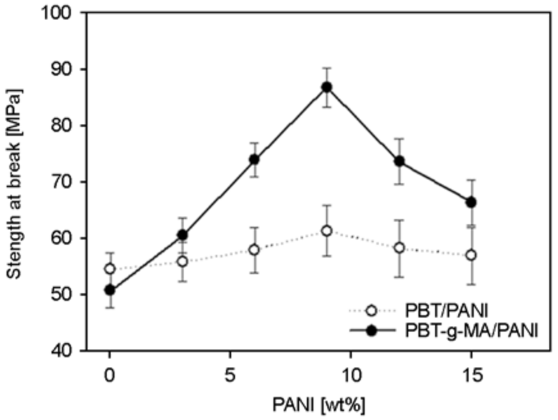

Figure 6. The effect of PANI content on tensile strength at break for PBT/PANI and PBT-g-MA/PANI composites

tent on the tensile strength was somewhat insignificant, which could be attributed to the fact that interfacial forces between the PBT matrix and the PANI consist of only relatively weak hydrogen bonds. In contrast, even though PBT-*g*-MA had a lower tensile strength than pure PBT, the PBT-*g*-MA/PANI composites exhibited much better tensile strength than the equivalent PBT/PANI composites. In addition, the tensile strength of PBT-*g*-MA/PANI hybrids increased rapidly as PANI content increased from 0 to 9 wt%, at which point the tensile strength approached a plateau and improved only slightly. The positive effect that PANI had on the tensile strength of PBT-*g*-MA was attributed to three factors: (1) the presence of PANI and the consequent formation of chemical bonds through dehydration of MA groups in PBT-*g*-MA, which immobilized or partially immobilized the polymer phases and added stiffness to the composite layers; (2) the high aspect ratio and surface area of the PANI; and (3) the powder dispersion of PANI layers in the polymer matrix. The data also suggested that PANI layers and molecular orientation contributed to the observed reinforcement effect. The slight decrease in tensile strength observed when the PANI content was above 9 wt% was attributed to the inevitable aggregation of PANI at higher PANI contents and is similar to the deterioration in other properties observed when PANI content was above 9 wt%. Together, these results support theoretical and molecular simulation predictions that stress transfer, and hence strength, of powder–polymer composites can be effectively increased by the formation of chemical bonds between the components [28–30].

3.4. Electrical properties

The electrical conductivities of PBT/PANI and PBT-*g*-MA/PANI composites were obtained by calculating the reciprocal of measured resistivity values and are summarized in Figure 7. As expected, both PBT/PANI and PBT-*g*-MA/PANI exhibited lower electrical resistivities than pure PBT and PBT-*g*-MA. Initially, the electrical resistivities decreased markedly with increasing PANI content, and then they decreased slightly when the content of PANI was greater than 9 wt%. Moreover, the electrical resistivity of each PBT-*g*-MA/PANI hybrid was lower than that of its PBT/PANI equivalent. The reduced electrical resistivities of PBT-*g*-MA/PANI composites compared to those of PBT/PANI composites were attributed to imide bond formation, which inhibited polymer motion in the MA-grafted materials and prohibited the chain rearrangement and reorganization required for solidification. The imide linkages formed in the PBT-*g*-MA/PANI were stronger than the hydrogen bonds formed in PBT/PANI and were thus more effective at hindering polymer motion. In turn, this lower resistivity also allowed the PBT-*g*-MA/PANI composites to more easily form an interconnected conductive pathway throughout the material. The lower observed resistivity in the 9 wt% composites indicated that an excess amount of PANI was present at levels >9 wt% and that PANI was physically dispersed throughout the polymer matrix. This excess may have led to aggregate formation phases, thereby reducing the matrix compatibility with PBT/PANI and PBT-*g*-MA/PANI.

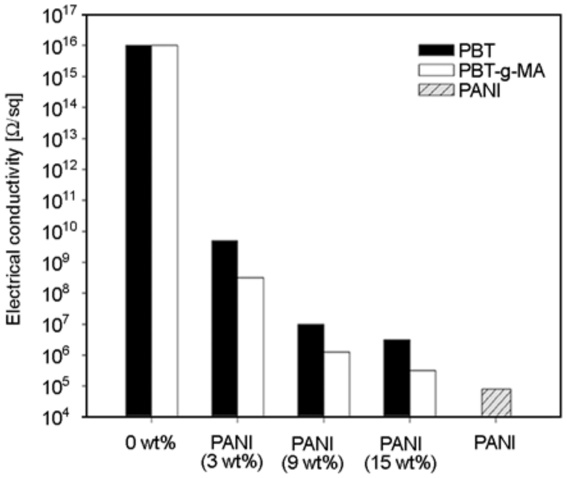

Figure 7. Electrical resistivities of PBT, PBT-*g*-MA, PBT/PANI, and PBT-*g*-MA/PANI composites

Although the 9 wt% PBT/PANI and PBT-*g*-MA/PANI composites exhibited resistivity values as low as 1.1·10^7 and 8.1·10^6 Ω/sq, they cannot be classified as conductive materials [31, 32]. The results of the antistatic testing with pristine PBT-*g*-MA and PBT-*g*-MA/PANI (sample size: 3.50 cm diameter and 0.10 cm thick) are depicted in Figure 8. Each film was rubbed and immersed in small plastic foam balls. Any adsorption of the plastic balls indicates the presence of static electricity. The pristine PBT-*g*-MA adsorbed a significant number of plastic balls, while the 3 wt% PBT-*g*-MA/PANI composite (Figure 8b) showed only a small number of balls attached to the surface. Furthermore, both the 9 and 15 wt% PBT-*g*-MA/PANI composites (Figure 8c, 8d) were clean due to its lower electrical resistivity (<10^9 Ω/sq). Although, the electrical resistivity of 3 wt% PBT-*g*-MA/PANI (6.7·10^8 Ω/sq) was in the range of dissipative materials, some plastic balls were adsorbed on the surface. The electrostatic dissipative property of the 3 wt% sample was not sufficient when compared to that of the 9 wt% (8.1·10^6 Ω/sq) and 15 wt% (3.4·10^5 Ω/sq) samples. From this result, it can be deduced that the samples exhibit absolute electrostatic dissipation when the electrical resistivity is <10^8 Ω/sq. Thus, the addition of PANI to the composite resulted in electrostatic dissipative properties in the bulk material, particularly when the PANI content was greater than 9 wt%.

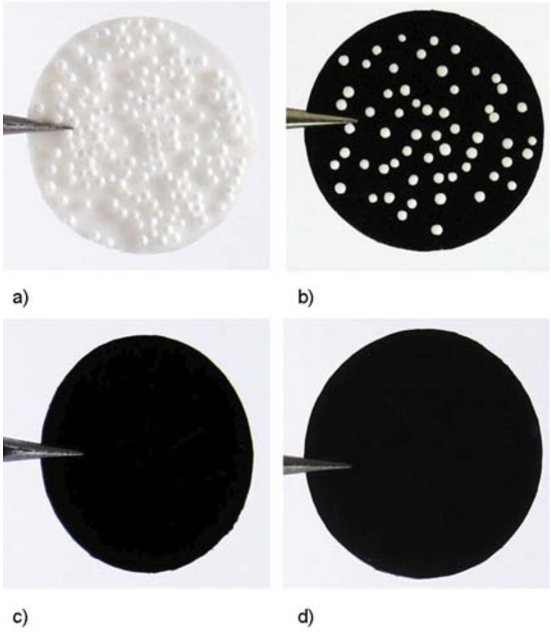

Figure 8. Antistatic properties of (a) PBT-*g*-MA, (b) PBT-*g*-MA/PANI (3 wt%), (c) PBT-*g*-MA/PANI (9 wt%), and (d) PBT-*g*-MA/PANI (15 wt%) composites

3.5. Antibacterial properties of the composites

Figure 9a illustrates the results of the antibacterial properties of the PBT/PANI and PBT-*g*-MA/PANI composites. Figure 9a shows that the PBT-*g*-MA *without* incorporated PANI displayed no antibacterial zones, indicating that the pure PBT-*g*-MA materials possessed no antibacterial properties. However, some micro-sized antibacterial zones were found in the PBT-*g*-MA/PANI composite specimens with as little as 3 wt% PANI, and with increasing PANI content, the antibacterial zones became more apparent. This indicated that the PBT-*g*-MA/PANI composites displayed an antibacterial effect due to the addition of PANI.

Antibacterial activity was evaluated with clinically infectious *E. coli* As shown in Figure 9b, when in contact with PBT or PBT-*g*-MA, the E. coli cell count increased with time from 1.26·10^6 to

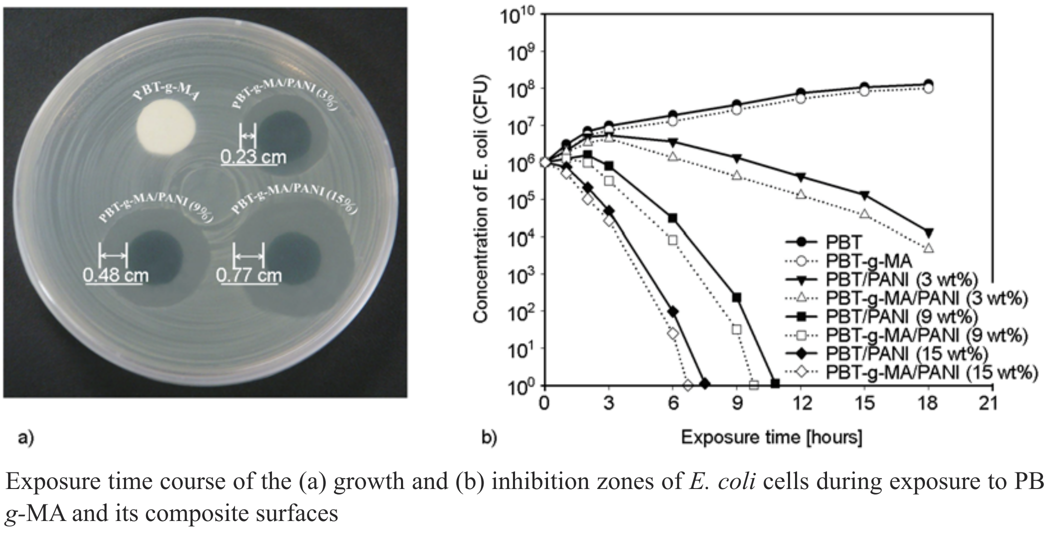

Figure 9. Exposure time course of the (a) growth and (b) inhibition zones of *E. coli* cells during exposure to PBT or PBT-*g*-MA and its composite surfaces

Table 1. Effects of PANI content on the antibacterial properties of PBT/PANI and PBT-*g*-MA/PANI composites

	PBT/PANI			PBT-g-MA/PANI		
	3 wt%	9 wt%	15 wt%	3 wt%	9 wt%	15 wt%
A	$1.26\cdot10^6$	$1.26\cdot10^6$	$1.26\cdot10^6$	$1.26\cdot10^6$	$1.26\cdot10^6$	$1.26\cdot10^6$
B	$1.31\cdot10^8$	$1.31\cdot10^8$	$1.31\cdot10^8$	$1.28\cdot10^8$	$1.28\cdot10^8$	$1.28\cdot10^8$
C	$1.33\cdot10^4$	0	0	$6.70\cdot10^3$	0	0
ABI	3.99	–	–	4.28	–	–
KBI	1.98	–	–	2.27	–	–

$1.31\cdot10^8$ CFU/mL and from $1.26\cdot10^6$ to $1.28\cdot10^8$ CFU/mL, respectively, after incubation at 37°C for 24 h. Conversely, under the same conditions, the bacterial cell count rapidly decreased to near zero when in contact with composites PBT/PANI or PBT-*g*-MA/PANI containing more than 9 wt% PANI. At 9 wt% PANI, the onset of *E. coli* reduction was observed at 3 h, which was significantly shorter than the approximately 6 h onset observed with the 3 wt% PANI composites. This effect is most likely due to the surface density of PANI. As noted in Table 1, according to the guidelines set forth by JIS L 1902:1998 and the Japanese Association for the Functional Evaluation of Textiles, it was concluded that PBT/PANI or PBT-*g*-MA/PANI suppressed the growth of *E. coli*. Furthermore, we noted that all the samples containing PBT-*g*-MA/PANI exhibited a higher degree of bacterial suppression than the corresponding samples of PBT/PANI, which was attributed to imide formation from the condensation of the anhydride carboxyl groups of PBT-*g*-MA with the amino groups of PANI. This led to stronger electrostatic interactions in PBT-*g*-MA/PANI and resulted in greater antibacterial activity; bacterial strains with an extracellular capsule such as *E. coli* carry less negative charge and are less prone to adsorption by the positively charged surface of PBT-*g*-MA/PANI.

4. Conclusions

The compatibility properties of PBT/PANI composites were improved when PBT-*g*-MA was used in place of PBT. The composite of PBT-*g*-MA with PANI led to the formation of imide functional groups that were not present in analogous PBT/PANI composites. These imide groups were responsible for different electrical properties between the two copolymers. FTIR spectra and ^{13}C solid-state NMR indicated that the MA moiety had been successfully grafted onto the PBT copolymer and that imide bonds had formed in the PBT-*g*-MA/PANI composites. The SEM microphotographs indicated that the wettability of PANI in PBT-*g*-MA was much better than the wettability of PANI in ungrafted PBT. Maximum tensile strengths occurred at about 9 wt% PANI, but excess PANI reduced the compatibility of the composite components due to aggregation of PANI. The electrical resistivity of the PBT-*g*-MA/PANI (9 wt%) composite was $8.1\cdot10^6$ Ω/sq, which is 10^7-fold lower than that of neat PBT, affording it high antistatic efficiency. Antibacterial activity was enhanced upon addition of 3 wt% PANI into PBT-*g*-MA and resulted in high ABI and KBI values. In summary, the current study demonstrates a method for enhancing the compatibility between PBT and PANI and improving the antibacterial and antistatic properties of PBT- and PANI-based composites.

References

[1] Tourillon G., Garnier F.: Effect of dopant on the physicochemical and electrical properties of organic conducting polymers. The Journal of Physical Chemistry, **87**, 2289–2292 (1983).
DOI: 10.1021/j100236a010

[2] Zhang K., Zhang L. L., Zhao X. S., Wu J.: Graphene/polyaniline nanofiber composites as supercapacitor electrodes. Chemistry of Materials, **22**, 1392–1401 (2010).
DOI: 10.1021/cm902876u

[3] Vercelli B., Zotti G.: Polypyrrole self-assembled monolayers and electrostatically assembled multilayers on gold and platinum electrodes for molecular junctions. Chemistry of Materials, **18**, 3754–3763 (2006).
DOI: 10.1021/cm060802e

[4] Liu P., Wu Y., Pan H., Ong B. S., Zhu S.: High-performance polythiophene thin-film transistors processed with environmentally benign solvent. Macromolecules, **43**, 6368–6373 (2010).
DOI: 10.1021/ma100212h

[5] Li Y., Wang Z., Wang Q., Wang C., Xue G. A.: A facile and efficient route for coating polyaniline onto positively charged substrate. Macromolecules, **43**, 4468–4471 (2010).
DOI: 10.1021/ma100475u

[6] Fowler J. D., Virji S., Kaner R. B., Weiller B. H.: Hydrogen detection by polyaniline nanofibers on gold and platinum electrodes. The Journal of Physical Chemistry C, **113**, 6444–6449 (2009).
DOI: 10.1021/jp810500q

[7] Li G., Martinez C., Semancik S.: Controlled electrophoretic patterning of polyaniline from a colloidal suspension. Journal of the American Chemical Society, **127**, 4903–4909 (2005).
DOI: 10.1021/ja0441763

[8] Chen Y., Kang E. T., Neoh K. G., Tan K. L.: Surface functionalization of poly(tetrafluoroethylene) films via consecutive graft copolymerization with glycidyl methacrylate and aniline. The Journal of Physical Chemistry B, **104**, 9171–9178 (2000).
DOI: 10.1021/jp000152g

[9] Wang P., Tan K. L., Zhang F., Kang E. T., Neoh K. G.: Synthesis and characterization of poly(ethylene glycol)-grafted polyaniline. Chemistry of Materials, **13**, 581–587 (2001).
DOI: 10.1021/cm000829c

[10] Sanchez C., Soler-Illia G. J. de A. A., Ribot F., Lalot T., Mayer C. R., Cabuil V.: Designed hybrid organic–inorganic nanocomposites from functional nanobuilding blocks. Chemistry of Materials, **13**, 3061–3083 (2001).
DOI: 10.1021/cm011061e

[11] Wu Q., Wang Z., Xue G.: Controlling the structure and morphology of monodisperse polystyrene/polyaniline composite particles. Advanced Functional Materials, **17**, 1784–1789 (2007).
DOI: 10.1002/adfm.200700170

[12] Chen C-F., Lee K-H., Chiu W-Y.: Synthesis and characterization of poly(butyl acrylate–methyl methacrylate)/polyaniline core–shell latexes. Journal of Applied Polymer Science, **104**, 823–830 (2007).
DOI: 10.1002/app.25624

[13] Wang Y., Jing X.: Preparation of polystyrene/polyaniline core/shell structured particles and their epoxy-based conductive composites. Polymer International, **56**, 126–131 (2007).
DOI: 10.1002/pi.2119

[14] Levchik S. V., Weil E. D.: Flame retardancy of thermoplastic polyesters – A review of the recent literature. Polymer International, **54**, 11–35 (2005).
DOI: 10.1002/pi.1663

[15] Danès F., Garnier B., Dupuis T., Lerendu P., Nguyen T-P.: Non-uniformity of the filler concentration and of the transverse thermal and electrical conductivities of filled polymer plates. Composites Science and Technology, **65**, 945–951 (2005).
DOI: 10.1016/j.compscitech.2004.10.017

[16] Gallo E., Braun U., Schartel B., Russo P., Acierno D.: Halogen-free flame retarded poly(butylene terephthalate) (PBT) using metal oxides/PBT nanocomposites in combination with aluminium phosphinate. Polymer Degradation and Stability, **94**, 1245–1253 (2009).
DOI: 10.1016/j.polymdegradstab.2009.04.014

[17] Dasaradhudu Y., Narasimha Rao V. V. R.: DC electrical conduction in solution-grown pure and iodine-doped poly(butylene terephthalate) films. Polymer International, **35**, 329–335 (1994).
DOI: 10.1002/pi.1994.210350405

[18] Braun U., Bahr H., Sturm H., Schartel B.: Flame retardancy mechanisms of metal phosphinates and metal phosphinates in combination with melamine cyanurate in glass-fiber reinforced poly(1,4-butylene terephthalate): The influence of metal cation. Polymers for Advanced Technologies, **19**, 680–692 (2008).
DOI: 10.1002/pat.1147

[19] Jang S. H., Kim Y. H., Lim S., Choi G. D., Kim S. H., Kim W. N.: Effects of fiber characteristics on the mechanical and rheological properties of poly(butylene terephthalate)/glass fiber composites. Journal of Applied Polymer Science, **116**, 3005–3012 (2010).
DOI: 10.1002/app.31844

[20] Chisholm B. J., Moore R. B., Barber B., Khouri F., Hempstead A., Larsen M., Olson E., Kelley J., Balch G., Caraher J.: Nanocomposites derived from sulfonated poly(butylene terephthalate). Macromolecules, **35**, 5508–5516 (2002).
DOI: 10.1021/ma012224n

[21] Wu C-S.: Renewable resource-based composites of recycled natural fibers and maleated polylactide bioplastic: Characterization and biodegradability. Polymer Degradation and Stability, **94**, 1076–1084 (2009).
DOI: 10.1016/j.polymdegradstab.2009.04.002

[22] Balabanovich A. I., Zevaco T. A., Schnabel W.: Fire retardance in poly(butylene terephthalate). The effects of red phosphorus and radiation-induced cross-links. Macromolecular Materials Engineering, **289**, 181–190 (2004).
DOI: 10.1002/mame.200300153

[23] Vicente A. I., Campos J., Bordado J. M., Ribeiro M. R.: Maleic anhydride modified ethylene–diene copolymers: Synthesis and properties. Reactive and Functional Polymers, **68**, 519–526 (2008).
DOI: 10.1016/j.reactfunctpolym.2007.10.026

[24] Zheng W., Levon K., Taka T., Laakso J., Österholm J-E.: Phase behaviors and interactions of *N*-alkylated polyanilines and ethylene-*co*-vinyl acetate blends. Journal of Polymer Science Part B: Polymer Physics, **33**, 1289–1306 (1995).
DOI: 10.1002/polb.1995.090330814

[25] Rodrigues P. C., Cantão M. P., Janissek P., Scarpa P. C. N., Mathias A. L., Ramos L. P., Gomes M. A. B.: Polyaniline/lignin blends: FTIR, MEV and electrochemical characterization. European Polymer Journal, **38**, 2213–2217 (2002).
DOI: 10.1016/S0014-3057(02)00114-3

[26] Jansen M. A. G., Goossens J. G. P., de Wit G., Bailly C., Koning C. E.: The microstructure of poly(butylene terephthalate) copolymers via ^{13}C NMR sequence distribution analysis: Solid-state copolymerization versus melt copolymerization. Analytica Chimica Acta, **557**, 19–30 (2006).
DOI: 10.1016/j.aca.2005.05.063

[27] Im J. S., Kim J. G., Lee S-H., Lee Y-S.: Enhanced adhesion and dispersion of carbon nanotube in PANI/PEO electrospun fibers for shielding effectiveness of electromagnetic interference. Colloids and Surfaces A: Physicochemical and Engineering Aspects, **364**, 151–157 (2010).
DOI: 10.1016/j.colsurfa.2010.05.015

[28] De Risi F. R., D'Ilario L., Martinelli A.: Synthesis and characterization of epoxidized polybutadiene/polyaniline graft conducting copolymer. Journal of Polymer Science Part A: Polymer Chemistry, **42**, 3082–3090 (2004).
DOI: 10.1002/pola.20150

[29] Chen S. A., Fang W. G.: Electrically conductive polyaniline-poly(vinyl alcohol) composite films: Physical properties and morphological structures. Macromolecules, **24**, 1242–1248 (1991).
DOI: 10.1021/ma00006a004

[30] Wu C-S.: Preparation and characterization of a polycaprolactone/C_{60} composite and its improved counterpart (PCL–NH_2/C_{60}–OH). Journal of Applied Polymer Science, **114**, 3489–3499 (2010).
DOI: 10.1002/app.30833

[31] Blythe A. R.: Electrical resistivity measurements of polymer materials. Polymer Testing, **4**, 195–209 (1984).
DOI: 10.1016/0142-9418(84)90012-6

[32] Narkis M., Lidor G., Vaxman A., Zuri L.: New injection moldable electrostatic dissipative (ESD) composites based on very low carbon black loading. Journal of Electrostatics, **47**, 201–214 (1999).
DOI: 10.1016/S0304-3886(99)00041-8

eXPRESS Polymer Letters Vol.6, No.6 (2012) 476–484
Available online at www.expresspolymlett.com
DOI: 10.3144/expresspolymlett.2012.50

Thermal diffusivity of *in-situ* exfoliated graphite intercalated compound/polyamide and graphite/polyamide composites

S. R. Kim[1*], *M. Poostforush*[1], *J. H. Kim*[1], *S. G. Lee*[2]

[1]Department of Polymer Science and Engineering, Chungju National University, 380-702 Chungju, Korea
[2]Information Research Center, Korea Research Institute of Chemical Technology, 360-154 Daejon, Korea

Received 13 November 2011; accepted in revised form 8 January 2012

Abstract. The thermal diffusivity of graphite intercalated compound (GIC)/polyamides (PA6, PA66 and PA12) and graphite/polyamides composites were investigated. The polyamides/GIC composites were prepared by an *in-situ* exfoliation melting process and thermal diffusivity of the composites was measured by a laser flash method. The surface chemistry of the GIC and graphite was investigated using Fourier transform infrared spectroscopy, the fracture morphology of the composites was observed by field emission scanning electron microscopy. The thermal diffusivity of the *in-situ* exfoliation processed PA/GIC composites showed a significant improvement over those of PA/expanded graphite intercalated compound composites and PA/graphite composites. We suggest that the larger flake size and high expansion ratio of the GIC during the *in-situ* exfoliation process leads to 3-dimensional conductive pathways and high thermal diffusivity. Thermal diffusivity of the polyamides/GIC (20 vol%) composites was increased approximately 18 times compared to that of pure polyamides.

Keywords: *polymer composites, thermal diffusivity, graphite intercalated compound*

---

1. Introduction

Thermal diffusivity is a measure of the rate of heat propagation through a material and it is an important property in nonsteady-state heat transfer, which occurs during the heating and cooling of a material [1]. Thermal diffusivity is crucial in certain practical applications and polymer composites with high thermal diffusivity can potentially be used in electronic circuit boards, heat sinks and light weight thermal management systems. The reliability of electronic devices is exponentially dependent on the operating temperature and quick dissipation of heat could increase the service life of these devices. To increase the thermal diffusivity of polymers, the addition of suitable inorganic or metallic fillers to the polymeric matrix is effective and convenient [2]. Graphite has a layered structure composed of alternating carbon layers. The carbon atoms are in-plane covalently bonded while carbon layers are bound by much weaker van der Waals forces. Graphite appears to be one of the most promising fillers in that could produce composites with excellent thermal, mechanical, and electrical properties at a reasonable cost. Graphite intercalated compound (GIC) expands up to few hundred times their initial volume at high temperatures and the expanded graphite sheets could exfoliate to a nanoscale level along the *c*-axis of the graphene layers [3, 4]. GIC has high conductivity and it could be a good candidate for thermal management systems and could be used in many applications where high thermal dissipation is required. The exfoliated nanosheets of GIC could

---

[*] Corresponding author, e-mail: srkim@cjnu.ac.kr

form continuous thermal conductive pathways and groups like –OH and –COOH in the exfoliated graphite sheet may result in good miscibility with both nonpolar and polar molecules [5]. There are many reports on the use of preheat-treated GIC as a filler [3, 5, 6]. However, there are very few studies on the thermal diffusivity of *in-situ* exfoliation processed graphite intercalated compound based composites. Uhl *et al*. [7] used different expandable graphite grades to prepare PA6/expandable graphite composites and they reported the enhancement of thermal stability without any significant deterioration in mechanical properties. Zheng and Wong [8] prepared poly(methyl methacrylate)/expanded graphite to study the effect of expanded graphite on electrical and structural integrity.

In this study, we used an *in-situ* exfoliation process to produce the GIC based thermally conductive polyamide (PA) composites. Graphite/polyamide composites were also prepared and the thermal diffusivity of this graphite/polyamide composite was compared with that of the GIC/PAs composites. The effect of polyamide grades and processing temperature on thermal diffusivity were also investigated.

2. Experimental

2.1. Materials

Three different types of commercial grade polyamides (PA6, PA66 and PA12) were chosen as the matrix. PA6 (1011 BRT, Hyosung, Seoul, Korea), PA66 (Radipol A45, Radici Chimica, Novara, Italy), and PA12 (30303 JFX1, Ube, Osaka, Japan) were used. The properties of the polymer matrices are summarized in Table 1. GIC (SFF, Chuetsu Graphite Works, Osaka, Japan) and graphite (SC20 QKG, Qingdao Kropfmuehl Graphite, Qingdao, China) were used as thermally conductive fillers and the properties of these fillers are shown in Table 2. GIC is a sulfuric acid based graphite intercalated compound. All the materials were used as-received condition.

Table 1. Matrix properties

	PA6	PA12	PA66
Density [kg/m^3]	1140	1010	1130
Melting temperature [°C]	224.2	172.6	266.9
Thermal diffusivity [m^2/s]	$1.59\cdot10^{-7}$	$1.22\cdot10^{-7}$	$1.58\cdot10^{-7}$
Sample shape	Pellet	Pellet	Pellet

2.2. Sample preparation

PAs and fillers (without any heat treatment) were dry mixed on desired volume percentages. Three different filler volume percentages, 5, 10, and 20 vol%, were used in the sample preparation. The exfoliated graphite nanosheets were produced from the sulfuric acid-treated intercalated graphite compound using *in-situ* melt processing. To prepare the expanded graphite intercalated compound (ExGIC), the weighted GIC was loaded into a crucible, put into a silicon muffle furnace (Wang-Sung, Seoul, Korea), and heat-treated at 280°C for 10 min. Due to the higher expansion ratio (~200) of GIC, a compaction step was needed after expansion to put the expanded GIC into the chamber of internal mixer and it was difficult to prepare PAs/ExGIC composites with a higher ExGIC loading.

The composites of polyamides with GIC, ExGIC and graphite were prepared by a batch-type mixer (W50EH, Brabender, Duisburg, Germany) at 60 rpm for 10 min at the appropriate processing temperature. After mixing the filler with polyamide, the composites were cooled at room temperature. Abrasive paper was used to make a disc sample with 10 mm diameter and 1 mm thickness to measure the thermal diffusivity.

2.3. Fourier transform infrared analysis

To investigate the chemical functional groups on the GIC and graphite, Fourier transform infrared (FTIR) spectra were obtained with a Bruker EQUINOX 55 (Bruker Optics, Wissemburg, France) in the mid infrared range (4000–400 cm^{-1}). The filler was ground with KBr powder and pressed into disc tablet to obtain the FTIR spectra.

Table 2. Properties of the graphite intercalated compound and graphite

Properties	Graphite intercalated compound	Graphite
Particle size [µm]	250	20
Onset expansion temperature [°C]	250	–
Density [kg/m^3]	2000	2100
Bulk density [kg/m^3]	580	170
Shape	Flake	Flake

2.4. Scanning electron microscopy

A field emission scanning electron microscope (S–4500, JEOL, Tokyo, Japan) at an acceleration voltage of 10 kV was used to observe the morphology of the fillers and the fractured surface of the composites. The composites were cryogenically fractured in liquid nitrogen. The samples were Pt-coated using a sputter coater (108, Cressington Scientific, Watford, UK) for 2 min before imaging to avoid charging during observation.

2.5. Differential scanning calorimeter analysis

To measure the heat of fusion and crystallinity of the virgin polyamides and composites, a differential scanning calorimeter (N-650, Scinco, Seoul, Korea) was used, a 10–15 mg sample was loaded in the Al pan and the experiments were conducted in a nitrogen atmosphere. The temperature range scanned was from 30 to 300°C at a heating rate of 20°C/min. The crystallnity (χ_c) of the composites was calculated with the Equation (1):

$$\chi_c = \frac{\Delta H_m}{\varphi \Delta H_m^0} \cdot 100 \qquad (1)$$

where ΔH_m is the heat of fusion of the polyamide, φ is the mass fraction of polyamide in the composites, and ΔH_m^0 is the heat of fusion of a 100% crystalline polyamide.

2.6. Thermal diffusivity

The thermal diffusivity (α) of the composites was measured by a laser flash method (TC-7000, ULVAC, Kanagawa, Japan) at 30°C. The laser flash technique was introduced in 1961 by Parker *et al.* [9]. This technique measures the characteristic rise time. Laser heat pulses irradiated on the front side of the disc sample; the heat was transmitted through the sample thickness (L) direction and was measured by an infrared camera. The time to reach the half of the maximum temperature ($t_{1/2}$) at the back side of the sample was chosen to calculate the thermal diffusivity by Equation (2):

$$\alpha = 1.38 \frac{L^2}{\pi^2 t_{1/2}} \qquad (2)$$

Due to nature of the phase delay technique, the measured property is the directional thermal diffusivity.

3. Results and discussion

3.1. FTIR analysis

Figure 1 shows the infra-red (IR) spectra of the heat treated GIC at 280°C and the spectra of graphite. The broad peak around 3435 cm^{-1} is attributed to absorbed water in the graphite GIC. The peak at 1397 cm^{-1} may be ascribed to NO_3^- which originates from the HNO_3 solution during the preparation step [10, 11]. The large band centered at 1100 cm^{-1} of the GIC is attributed to sulphates. It indicates that traces of sulphuric acid are still present in the GIC after expansion. The peak in the 1500–1680 cm^{-1} region is assigned to aromatic C=C bonds and various substitution modes of the aromatic ring. The peaks at 2900–2800 cm^{-1} of the GIC indicate the presence of aliphatic carbons. Such species may be produced during the degradation of graphite under air [12]. Oxygen functional groups on the surface of fillers may facilitate chemical interactions with the functional groups of the polyamide.

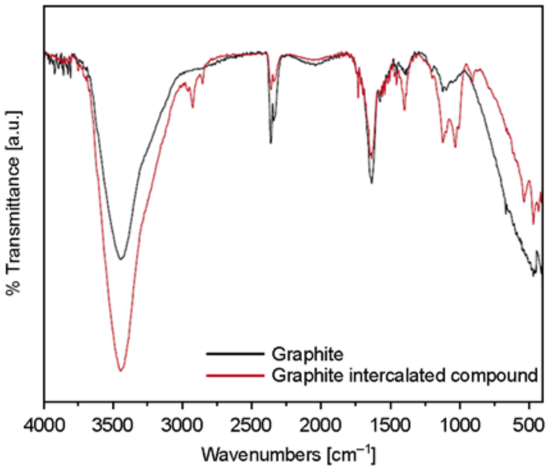

Figure 1. FTIR spectra of graphite and graphite intercalated compound (heat-treated at 280°C)

3.2. Morphological characteristics

The graphite, GIC, and polyamide based composites were observed by scanning electron microscope (SEM). Figure 2a shows the image of graphite flakes with average particle size of 20 µm. The GIC before expansion has a relatively smooth surface and some small flakes were observed on the surface of the GIC as shown in Figure 2b. The irregular flake shape of the GIC was similar to natural graphite flakes and the graphite stacks can be seen from the side view (not shown). The diameter and thickness of the GIC

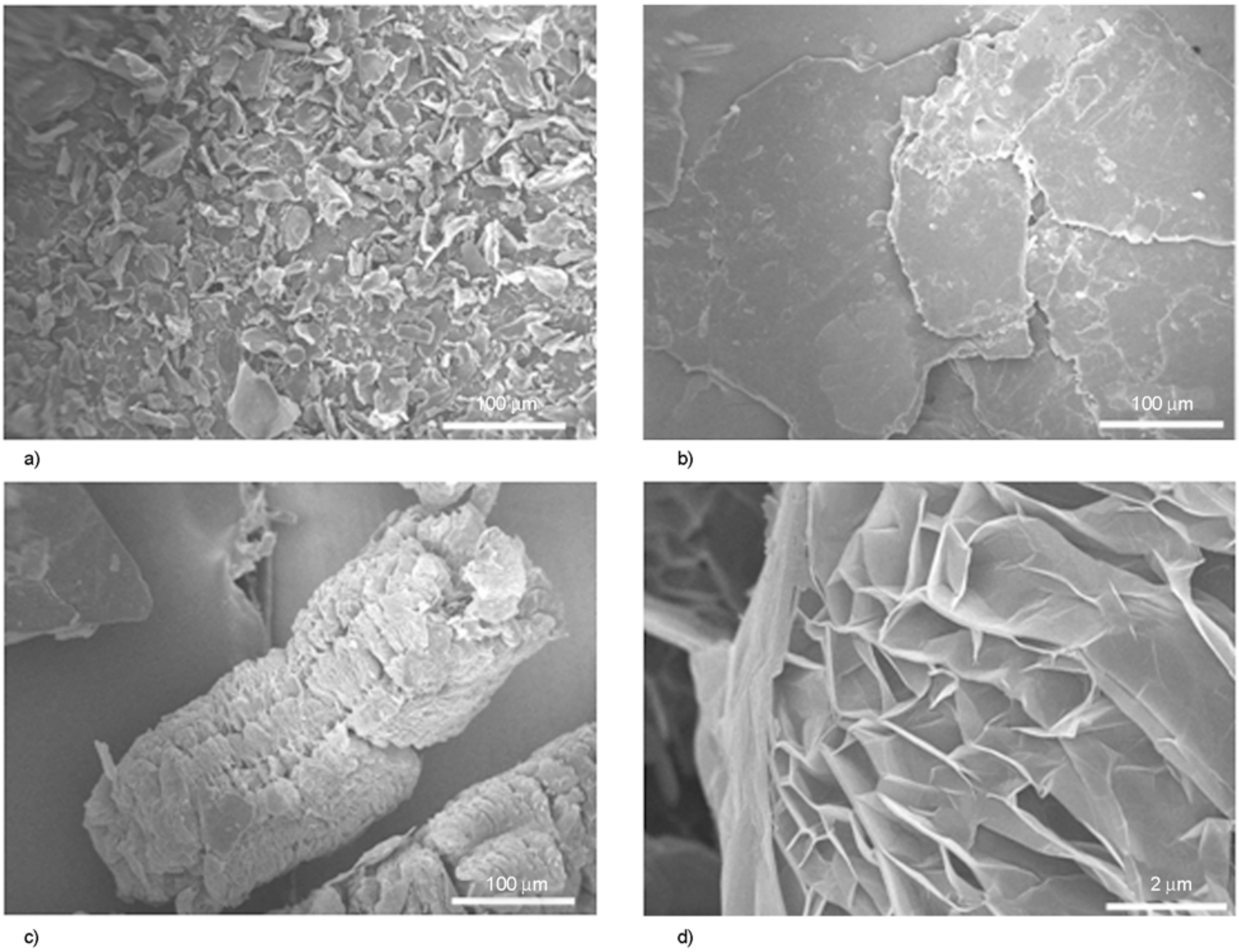

Figure 2. SEM images of (a) graphite (×250), (b) graphite intercalated compound before expansion (×250), (c) expanded graphite intercalated compound (×250), and (d) expanded graphite intercalated compound (×10 000)

before expansion were about 150 and 10 µm, respectively. The worm-like structure of GIC was observed (Figure 2c) after heating to 280°C. The SEM image at higher magnifications shows layered structures with thicknesses ranging from a few nanometers to a few micrometers (Figure 2d). Figures 3a–3c show the fractured SEM images of different polyamides based composites at 10 vol% of GIC loading after *in-situ* exfoliation processing.

The nanosheets of exfoliated/intercalated graphite were well dispersed in the all polyamide matrices during *in-situ* the exfoliation processing. The intercalated/exfoliated graphite structure was observed when the processing temperature was higher than the onset expansion temperature, i.e. 250°C, for GIC. The distance between the expanded nanosheets was as large as several micrometers and the thickness of the exfoliated nanosheets in the polyamide matrix mostly ranged from 40 to 80 nm, it decreased to as low as 7 nm after *in-situ* exfoliation processing (inset in Figure 3c).

Carbon atoms positioned in adjacent planes on the graphite layer are bound by weaker van der Waals forces. The weak interplanar forces allow for certain atoms, molecules, and ions to intercalate into the interplanar spaces of the graphite and the expansion ratio of GIC varies with temperature, heat treatment time, intercalating temperature etc. [5]. In general, the expansion ratio in c axis of the GIC is 200–300 [13]. The high expansion of the GIC during *in-situ* exfoliation could offer close contact between the matrix and exfoliated nanosheets and form 3-dimensional conductive pathways in the matrix.

We also used graphite as a filler to compare with the GIC. The average particle size of the graphite was 20 µm and the thickness was ca. 2 µm. The graphite filler did not expand and a continuous graphite net-

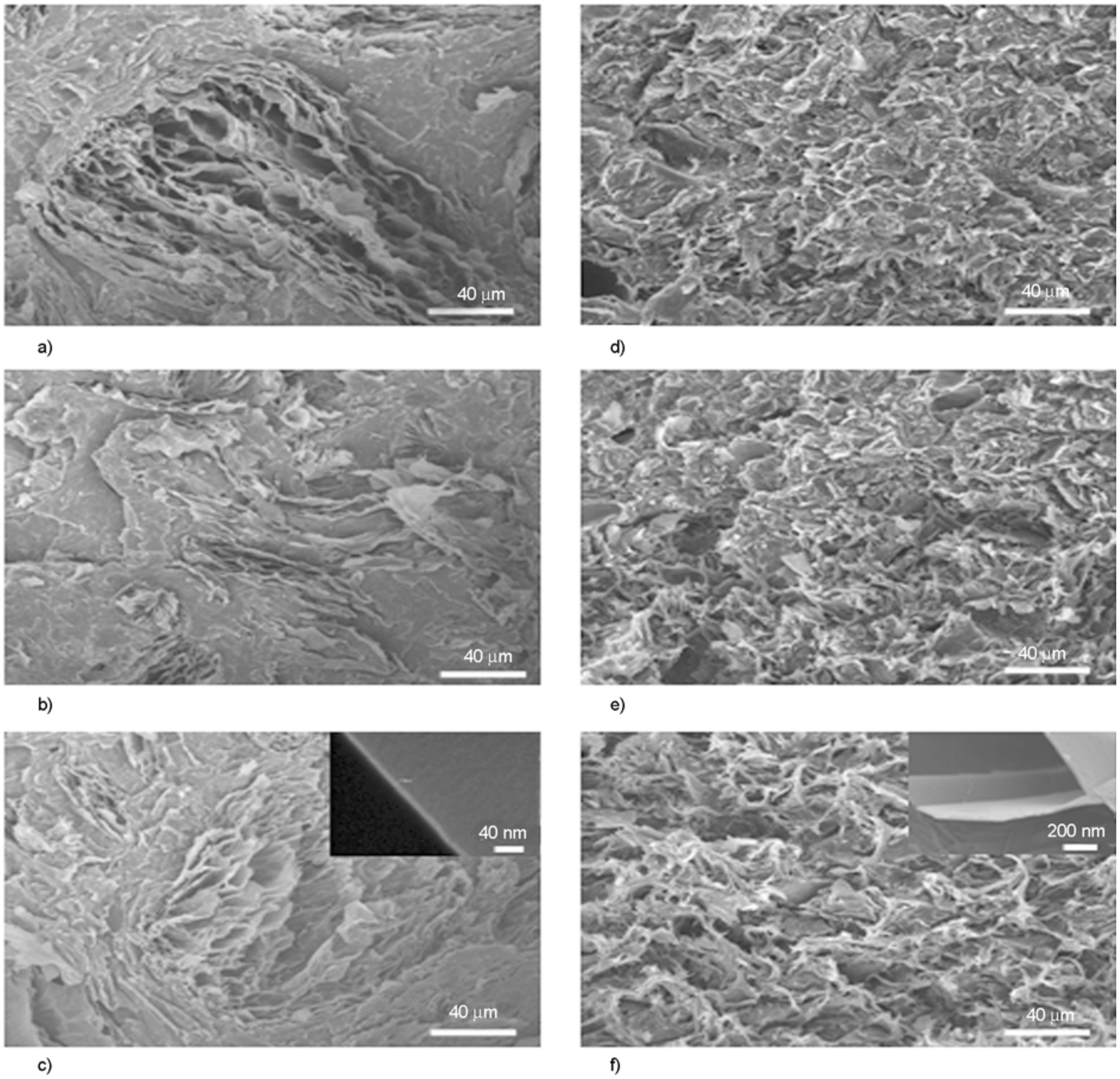

Figure 3. SEM images of PA composites at 10 vol% of fillers (a) PA6/GIC, (b) PA66/GIC, (c) PA12/GIC, (d) PA6/graphite, (e) PA66/graphite, and (f) PA12/graphite (×500)

work was not observed in the polyamide. Small graphite fillers in thermally insulating polyamide matrix could increase the thermal interface resistance which plays a critical role in heat transfer [14, 15]. As shown in Figures 3d–3f, the small graphite particles were dispersed well in the polyamide matrix after melt mixing. A graphite sheet thickness of ca. 50 nm was observed (inset of Figure 3f).

The fracture surface of the PA12/graphite composite showed the elongated ligaments of the matrix due to the ductile nature of PA12. Exfoliation/intercalation of the GIC in the polyamide matrix resulted in a larger contact area between nanosheets (Figures 3a–3c). Therefore, it is apparent that the phonon transfer of GIC based composites is much easier than that of graphite based composites.

To investigate the effect of the processing temperature of the graphite intercalated compound on the thermal diffusivity of the PA/GIC, two different processing temperatures, i.e., a temperature lower (210°C) and the higher (265°C) than the expansion temperature (250°C) of GIC were chosen. Different processing temperatures led to a distinctive morphology of the composites, as shown in Figure 4. At lower temperature (Figure 4a), the graphite particles remained in a stacked form. At the higher processing temperature (265°C), however, the GIC was exfoliated and the micro- and nanosheets were sep-

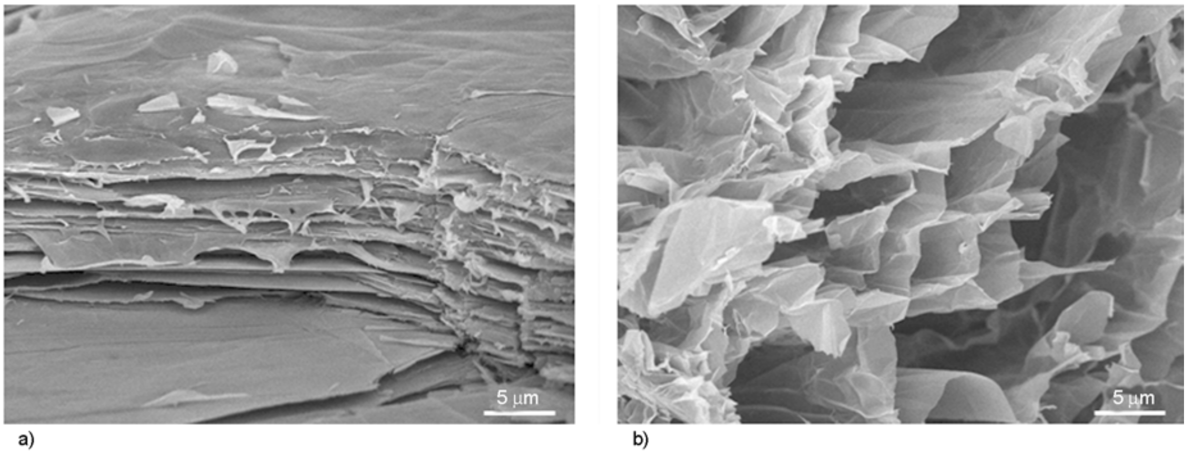

Figure 4. SEM images of PA12/GIC composites processed (a) at 210°C and (b) at 265°C (×3000)

arated and big spaces of up to ~10 µm between the graphite sheets were observed (Figure 4b). The higher expansion ratio and appropriate dispersion of the GIC at a higher processing temperature than the onset expansion temperature (250°C), led to the exfoliation of the GIC and formed tightly connected thermal paths as shown in Figure 4b.

3.3. Crystallinity

To investigate the crytallinity effect on thermal diffusivity, the heat of fusion of the composite was measured using differential scanning calorimetry (DSC). The DSC melting curves of the polyamides and composites at 20 vol% of filler content are plotted in Figure 5, and related thermal properties derived from the DSC thermograms are summarized in Table 3. Table 3 shows the Tm, crystallinity and thermal diffusivity of different polyamides and composites. The crystallinities of pure PA6, PA66, and PA12 were 46.9, 41.1 and 24.7%, respectively. The presence of intercalated/exfoliated graphite sheets may also affect the crystallization behavior of the polyamides. The crystallinity at 20 vol% of graphite and graphite intercalated compounds are lower than that of pure polyamide 6. The crystallinity was higher in the GIC filled composite compared to the graphite filled composite. The graphite nanosheets in the composites may induce transcrystallization and the higher surface of exfoliated/intercalated GIC compared to the graphite could provide more filler surface for crystal nucleation and result in the higher crystallinity. The longer methylene

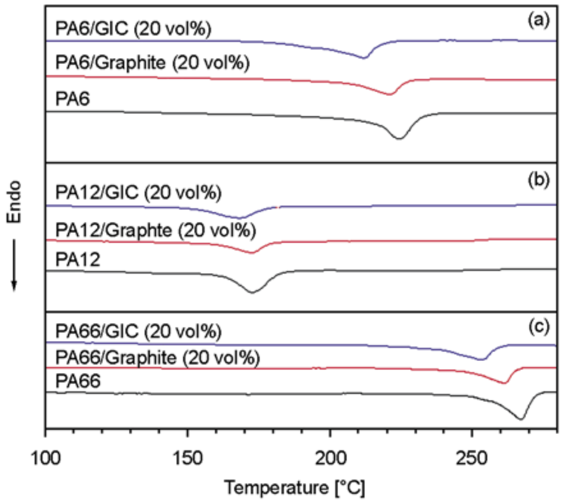

Figure 5. Melting curves of polyamides and PA composites by DSC (a) PA6, (b) PA12, and (c) PA66

Table 3. DSC results and the thermal diffusivity of pure polyamides and composites

Sample	T_m [°C]	ΔH_m [J/g]	χ_c[a] [%]	Thermal diffusivity [m^2/s]
PA6	224.2	89.3	46.9	$1.59\cdot10^{-7}$
PA6/Graphite (20 vol%)	219.0	49.7	26.1	$1.23\cdot10^{-6}$
PA6/GIC (20 vol%)	211.9	58.0	30.4	$2.59\cdot10^{-6}$
PA66	266.9	78.1	41.1	$1.58\cdot10^{-7}$
PA66/Graphite (20 vol%)	261.3	42.1	27.7	$1.20\cdot10^{-6}$
PA66/GIC (20 vol%)	250.3	46.8	30.8	$2.49\cdot10^{-6}$
PA12	172.6	37.5	24.7	$1.22\cdot10^{-7}$
PA12/Graphite (20 vol%)	171.0	22.4	13.4	$8.63\cdot10^{-7}$
PA12/GIC (20 vol%)	167.6	33.2	19.8	$2.59\cdot10^{-6}$

[a] The heat of crystallization of 100% crystalline PA6 [16], PA66 [17], and PA12 [18] is 202.7, 190.0, and 209.2 J/g, respectively.

group and the smaller amount of hydrogen bonding in the PA12 compare to the PA6 and PA66 leads to the less chain alignment and lower crystallinity.

The crystalline part conducts phonon better than the amorphous part [19]. In graphite containing composites, the thermal diffusivity of matrix is dominant and the higher crystallinty of PA6 and PA66 compared to that of PA12 may result in the higher thermal diffusivity of PA6/graphite and PA66/graphite. However, in GIC containing PA composites, the 3-dimensional network of GIC may be dominant at higher volume percentage as a result of *in-situ* exfoliation than the thermal diffusivity of matrix and the thermal diffusivity of PAs/GIC (20 vol%) composites was similar among polyamide grades.

The melting temperatures of PA/GIC composites shift toward a lower temperature, which is potentially related to the reduction of hydrogen bonding between polyamide molecules by the presence of nanoscale graphite sheets and imperfect crystals [20].

3.4. Thermal diffusivity

Figure 6 shows the thermal diffusivity of three different polyamides based composites as a function of filler loading. The thermal diffusivity linearly increased with increasing filler content due to the decrease of distance and the increase of the overlapped area of graphite fillers. However, there was a noticeable difference in the heat conducting capability of the GIC, ExGIC and graphite based composites. The thermal diffusivity of the PA/GIC was higher than that of the PA/graphite composites in all volume percentages. The higher expansion ratio and the larger diameter, of up to tens of micrometers, of the exfoliated/intercalated sheets and the functional groups on the surface in the exfoliated/intercalated graphite may be responsible for the higher thermal diffusivity. Most of the heat transfer occurs by phonons in the polymer composites and there is less phonon scattering in the largely overlapped PA/GIC which leads to a high thermal diffusivity. The smaller graphite particles than those in the GIC act as phonon scattering centers and further impede the heat transfer from graphite particle to graphite particle. Phonon transfer across the interface is hindered and the thermal resistance of the interface, also called the Kapitza resistance, represents a barrier to heat flow associated with differences in the phonon spectra of the two phases. In PA/graphite (20 vol%) composites, the small sized graphite particles resulted in a reduction of more than 50% in the thermal diffusivity compared with the *in-situ* exfoliated GIC/PA composites.

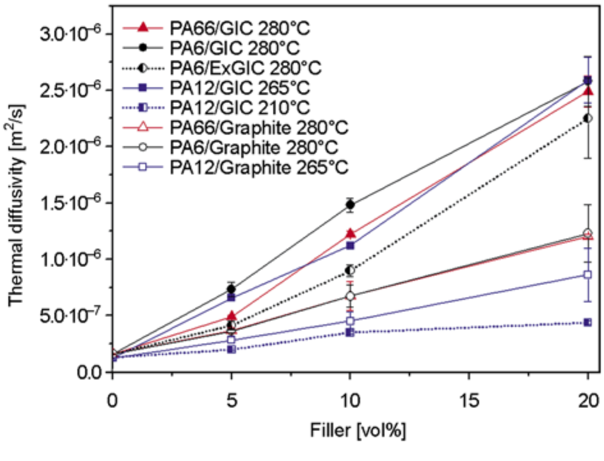

Figure 6. Thermal diffusivity of the PAs/GIC, PA6/ExGIC, and PAs/graphite composites as a function of filler loading

The thermal diffusivity of randomly oriented GIC/polyamide composites was increased to $2.59\cdot10^{-6}$ m^2/s at 20 vol%. This is an increase of approximately 18 times compared to pure polyamides. This magnitude is comparable to the through-plane thermal diffusivity, $3.28\cdot10^{-6}$ m^2/s, of polyetherimide (1.5 wt%)/graphite nanoplatelets (xGnP-15, 98.5 wt%) paper prepared by vacuum filtration method [21].

It should be noted that the thermal diffusivity of the three different polyamides based composites at 20 vol% of graphite intercalated compound was similar. The dominant contribution of thermal diffusivity from the *in-situ* exfoliated graphite sheets over the PA matrix could be a reason for the similar thermal diffusivity of three PA/GIC composites.

The PA6/ExGIC composites showed a lower thermal diffusivity than the *in-situ* processed PA6/GIC composites. It could be related to significant lateral size reduction of graphite platelets in ExGIC during melt mixing (not shown). The smaller size and overlap of graphite platelets in polymer matrix is not beneficial for phonon transfer and it may result in lower thermal diffusivity than that of *in-situ* processed PAs/GIC composites.

The thermal diffusivity of PA12/graphite (20 vol%) composites was the lowest among all the composites at same filler content. The fracture surface of PA12/graphite composite (Figure 3f) shows the higher number of elongated fibrils compared to that of PA6- and PA66 based composites (Figure 3d, 3e). The longer methylene segment and the lower crystallinity of PA12 could lead to better graphite dispersion and the elongated fibril structure without formation of thermally conductive pathways. It could increase the interfacial thermal resistance or the phonon scattering and consequently could lower the thermal diffusivity.

The thermal diffusivity of the PA12/GIC was significantly increased by changing the processing temperature from 210 to 265°C as shown in Figure 6. This is explained by the expansion of the GIC, as shown in Figure 4. The GIC remained in stacked at the lower processing temperature, 210°C, and the thermal diffusivity of the PA12/GIC composite was $3.83\cdot10^{-7}$ m^2/s m²/s at 20 vol%, this slightly increased with increasing GIC content. However, the thermal diffusivity of the PA/GIC composite increased rapidly with GIC content when processed at 265°C. Here the thermal diffusivity was 7 times higher, $2.59\cdot10^{-6}$ m^2/s, than that of the sample processed at 210°C. There was little change in the thermal diffusivity with respect to processing temperature in the graphite based PA composites (not shown).

4. Conclusions

Highly thermally conductive polyamide composites were developed using *in-situ* exfoliation of graphite intercalated compound and the thermal diffusivity of the PA/GIC composites was compared to the PA/graphite composites. The PA/GIC composites showed considerably greater improvements in thermal diffusivity compared to the PA/ExGIC and PA/graphite composites. The thermal diffusivity of PA66/GIC (20 vol%) was increased 18 times compared to that of pure PA66. The larger particle size, high expansion ratio, the surface chemistry and the formation of 3-dimensional thermally conductive pathways of GIC resulted in this high thermal diffusivity. The thermal diffusivity of the *in-situ* exfoliated PA/GIC composite was comparable to that of through-plane graphite nanoplatelet (xGnP) paper prepared by vacuum filtration method. The high thermal diffusivity was obtained when the melt processing temperature was higher than the onset temperature of expansion. Utilization of *in-situ* exfoliated GIC in other polymeric matrixes or in hybrid composites could offer promising thermal diffusivity at a reasonable cost.

Acknowledgements

This research was financially supported by the Ministry of Education, Science Technology of Korea through the Human Resource Training Project for Regional Innovation and the Fundamental R & D Program for Core Technology of Materials which are sponsored by the Ministry of Knowledge Economy of the Korean Government.

References

[1] Vettegren V. I., Bashkarev A. Ya., Suslov M. A.: Thermal diffusivity of antifriction polymer composites. Technical Physics Letters, **33**, 869–871 (2007). DOI: 10.1134/S1063785007100185

[2] Singh V., Joung D., Zhai L., Das S., Khondaker S. I., Seal S.: Graphene based materials: Past, present and future. Progress in Materials Science, **56**, 1178–271 (2011). DOI: 10.1016/j.pmatsci.2011.03.003

[3] Zheng W., Wong S-C., Sue H-J.: Transport behavior of PMMA/expanded graphite nanocomposites. Polymer, **43**, 5767–5773 (2002). DOI: 10.1016/S0032-3861(02)00599-2

[4] Chen G-H., Wu D-J., Weng W-G., He B., Yan W-L.: Preparation of polystyrene–graphite conducting nanocomposites via intercalation polymerization. Polymer International, **50**, 980–985 (2001). DOI: 10.1002/pi.729

[5] Li Y-C., Chen G-C.: HDPE/expanded graphite nanocomposites prepared via masterbatch process. Polymer Engineering and Science, **47**, 882–888 (2007). DOI: 10.1002/pen.20772

[6] Fukushima H., Drzal L. T., Rook B. P., Rich M. J.: Thermal conductivity of exfoliated graphite nanocomposites. Journal of Thermal Analysis and Calorimetry, **85**, 235–238 (2006). DOI: 10.1007/s10973-005-7344-x

[7] Uhl F. M., Yao Q., Nakajima H., Manias E., Wilkie C. A.: Expandable graphite/polyamide-6 nanocomposites. Polymer Degradation and Stability, **89**, 70–84 (2005). DOI: 10.1016/j.polymdegradstab.2005.01.004

[8] Zheng W., Wong S-C.: Electrical conductivity and dielectric properties of PMMA/expanded graphite composites. Composites Science and Technology, **63**, 225–235 (2003). DOI: 10.1016/S0266-3538(02)00201-4

[9] Parker W. J., Jenkins R. J., Butter C. P., Abbot G. L.: Flash method of determining thermal diffusivity, heat capacity, and thermal conductivity. Journal of Applied Physics, **32**, 1679–1684 (1961). DOI: 10.1063/1.1728417

[10] Nakamoto K.: Infrared and Raman spectra of inorganic and coordination compounds. Wiley, New York (1997).

[11] Zhang S., Gu A., Gao H., Che X.: Characterization of exfoliated graphite prepared with the method of secondary intervening. International Journal of Industrial Chemistry, **2**, 123–130 (2011).

[12] Duquesne S., Le Bras M., Bourbigot S., Delobel R., Vezin H., Camino G., Eling B., Lindsay C., Roels T.: Expandable graphite: A fire retardant additive for polyurethane coatings. Fire and Materials, **27**, 103–117 (2003).
DOI: 10.1002/fam.812

[13] Pan Y-X., Yu Z-Z., Ou Y-C., Hu G-H.: A new process of fabricating electrically conducting nylon 6/graphite nanocomposites via intercalation polymerization. Journal of Polymer Science Part B: Polymer Physics, **38**, 1626–1633 (2000).
DOI: 10.1002/(SICI)1099-0488(20000615)38:12<1626::AID-POLB80>3.0.CO;2-R

[14] Nan G-W., Liu G., Lin Y., Li M.: Interface effect on thermal conductivity of carbon nanotube composites. Applied Physics Letters, **85**, 3549–3551 (2004).
DOI: 10.1063/1.1808874

[15] Huxtable S. T., Cahill D. G., Shenogin S., Xue L., Ozisik L., Barone P., Usrey M., Strano M. S., Siddons G., Shim M., Keblinski P.: Interfacial heat flow in carbon nanotube suspensions. Nature Materials, **2**, 731–734 (2003).
DOI: 10.1038/nmat996

[16] Chao L-C., Chang E-P.: Interaction of anhydrous ferric chloride with nylon 6. Journal of Applied Polymer Science, **26**, 603–610 (1981).
DOI: 10.1002/app.1981.070260219

[17] Prime R. B.: Thermosets. in 'Thermal characterization of polymeric materials' (ed.: Turi E.) Academic Press, San Diego, 1380–1766 (1997).

[18] Gogolewski S., Czerntawska K., Gastorek K.: Effect of annealing on thermal properties and crystalline structure of polyamides. Nylon 12 (polylaurolactam). Colloid and Polymer Science, 258, 1130–1136 (1980).
DOI: 10.1007/BF01382456

[19] Han Z., Fina A.: Thermal conductivity of carbon nanotubes and their polymer nanocomposites: A review. Progress in Polymer Science, **36**, 914–944 (2011).
DOI: 10.1016/j.progpolymsci.2010.11.004

[20] Zhou H., Zhang S., Yang M.: The thermal conductivity of Nylon 6/clay nanocomposites. Journal of Applied Polymer Science, **108**, 3822–3827 (2008).
DOI: 10.1002/app.27984

[21] Xiang J., Drzal L. T.: Thermal conductivity of exfoliated graphite nanoplatelet paper. Carbon, **49**, 773–778 (2011).
DOI: 10.1016/j.carbon.2010.10.003

eXPRESS Polymer Letters Vol.6, No.6 (2012) 485–493
Available online at www.expresspolymlett.com
DOI: 10.3144/expresspolymlett.2012.51

Preparation of poly(ethylene terephthalate)/layered double hydroxide nanocomposites by *in-situ* polymerization and their thermal property

W. Cui, Q. Jiao, Y. Zhao, H. Li, H. Liu, M. Zhou*

School of Chemical Engineering and the Environment, Beijing Institute of Technology, 100081 Beijing, P. R. China

Received 2 November 2011; accepted in revised form 11 January 2012

Abstract. Terephthalate (TA) intercalated layered double hydroxides (LDHs) were synthesized using hydroxides as raw materials, and poly(ethylene terephthalate) (PET)/LDH nanocomposites with different contents of TA intercalated LDHs were prepared by *in-situ* polymerization. The structure, morphology and thermal property of PET/LDH nanocomposites were investigated. The TA intercalated LDHs were partially exfoliated and well dispersed in PET matrix. The PET/LDH nanocomposites exhibit enhanced thermal stability relative to pure PET, confirmed by the thermogravimetric analysis results. The results of differential scanning calorimetry suggest that LDH nanoparticles could effectively promote the nucleation and crystallization of PET.

Keywords: *nanocomposites, poly(ethylene terephthalate), layered double hydroxides, in situ polymerization*

1. Introduction

Layered double hydroxides (LDHs), known as a class of anionic clays, have attracted increasing interest due to their broad applications in areas such as catalysis, materials, medicine and environmental protection. LDHs can be represented by the general formula $[M^{2+}_{(1-x)}M^{3+}_{x}(OH)_2]^{x+}\cdot A^{n-}_{x/n}\cdot zH_2O$, where the di- and trivalent cations (M^{2+} and M^{3+}, respectively) can be most metal ions. The value of x may be varied over a wide range. An^{-} is an exchangeable anion, which can be simple inorganic species, organic anions, heteropoly acid anions, polymers [1, 2].

The polymer/LDH systems have been much less studied than the cationic clays due to the delamination difficulties of LDHs with the small gallery space and hydrophilic surface character [3]. However, the highly tunable properties, the anion exchange capacity have converted these materials into a new emerging class of layered crystals, which seems to be better suited for the preparation of multifunctional polymer/layered crystal nanocomposites. In recent years, study on the LDH nanocomposites with various polymers such as polyimide [4], epoxy [5], poly(ethylene terephthalate) (PET) [6], polyamide 6 [7], poly(butylene terephtahlate) [8], unsaturated polyester [9] and poly(vinyl alcohol) [10, 11], concerning physical properties and dispersion, has been widely reported. To apply anionic LDHs to nanocomposite system, preparation of organo-modified LDHs resulting in an increase in gallery spacing is very important because inorganic LDHs and organic polymer matrix are basically incompatible. In the past 20 years, many reports about the intercalation of organic anions into LDHs were discussed [12–17].

PET is a semicrystalline polyester with a high melting point and very good mechanical strength, due to the presence of the aromatic ring in the polymeric

---

*Corresponding author, e-mail: jiaoqz@bit.edu.cn structure [18]. Recently, PET/organo-modified LDH nanocomposites have been reported and focused on their synthesis and properties. Lee and coworkers [18] prepared PET/LDH nanocomposites using anionic surfactants intercalated LDHs by a direct melt compounding method. Rives and coworkers prepared PET/LDH nanocomposites through a microwave [19] and mechanical grinding method [20]. Dodecylsulfate intercalated LDHs were used to enhance the compatibility between the PET polymer and the LDHs. Recently, Rives and coworkers [21] reported the preparation of PET/LDH nanocomposites using TA intercalated LDHs through a microwave heating route. It is found that the microwave process improves the dispersion and the thermal stability of nanocomposites due to the interaction of the microwave radiation.

However, *in situ* polymerization has become the main procedure for the preparation of nanocomposites due to its versatility and compatibility with reactive monomers [22], as well as permitting the control of the polymer and the composite structures. This method relies on the swelling of the organically modified LDHs by the monomer, followed by *in situ* polymerization initiated thermally or by addition of a suitable compound (catalyst) [19]. The chain growth in the LDH galleries accelerates exfoliation and nanocomposite formation [6].

In this work, PET/LDH nanocomposites were prepared by *in situ* polymerization. LDHs were organically modified using terephthalate (TA) as the interlamellar anion, to overcome the lack of compatibility between the polymer and LDHs containing purely inorganic anions. The chemical, thermal properties and morphology of the PET/LDH nanocomposites were studied.

2. Experimental

2.1. Materials

All the reagents were purchased from the Beijing YILI Fine Chemical Limited (Beijing, P.R. China) and used without further purification.

2.2. Preparation of TA intercalated LDHs

The preparation of TA intercalated LDHs followed a simple but efficient method that was newly developed in our laboratories [23, 24]. The key feature of this method is a reaction of freshly generated hydroxides and terephthalic acid under a hydrothermal condition. Compared to other methods, the terephthalate-intercalated LDHs synthesized using this method exhibit higher purity and higher crystallinity.

The freshly generated $Mg(OH)_2$ and $Al(OH)_3$ (molar ratio 2:1) were placed in 80 mL of deionized water. Terephthalic acid was added to the suspension with a vigorous stirring. Then the suspension was taken under a hydrothermal condition at 120°C for 10 h. The product was collected after filtration by vacuum pumping and washed thoroughly with deionized water several times, and dried at 80°C overnight.

2.3. Preparation of PET/LDH nanocomposites

All the samples were prepared by a conventional 2-step polycondensation [6, 25]. In a typical procedure for the preparation of PET/LDH nanocomposites, TA intercalated LDHs were previously dispersed in ethylene glycol (EG, 1 mol) using a sonicating homogenizer for 15 min. The EG slurry containing TA intercalated LDHs was then mixed with dimethyl terephthalate (DMT) (0.5 mol) and 0.020 wt% (with respect to the DMT amount) of manganese acetate and magnesium acetate as catalyst. TA intercalated LDH contents were 0, 0.5, 1.0, and 2.0 wt% with respect to the DMT amount. The ester interchange reaction was carried out at 190–230°C with a continuous removal of byproduct (methanol). Polycondensation reaction was carried out at 280°C with ethylene glycol antimony catalyst at a pressure of 0.1 Torr for 2 h. The as-synthesized nanocomposite samples were dried at vacuum oven for 1 day at 70°C.

2.4. Characterizations

The crystal structures of samples were identified using a powder X-ray diffraction (XRD) on an X' Pert Pro MPD Powder X-Ray diffractometer (PANalytical, Almelo, Holland) with Cu Kα radiation. FT-IR spectra were recorded on a Bruker Vector 22 instrument (Brucker AXS, GmbH, Germany) after 20 scans within 4000–400 cm^{-1} at a resolution of 2 cm^{-1}. The sample was finely ground for 1 min, combined with oven dried spectroscopic grade KBr and pressed into a disc. The Scanning electron microscopy (SEM) images were recorded by a S-4800 instrument (Hitachi, Tokyo, Japan) at 15 kV. The SEM micrographs were taken from a sample fractured surface which was broken in liquid nitrogen and the morphology of the samples was observed on a JEM-1200EX (JEOL Ltd, Japan) transmission electron microscope (TEM) operated at 100 kV with copper mounted holey carbon grids. Thermogravimetric analysis (TGA) was carried out on a TA instrument Q5000 thermobalance (TA instruments, New Castle, DE, USA) over the range of 50 to 650°C at a heating rate of 10°C·min^{-1} under air atmosphere (50 mL·min^{-1}). The thermal properties of the nanocomposites were examined with a Shimadzu DSC-60 instrument (Shimadzu, Kyoto, Japan). To remove previous thermal history, all samples were first heated 300°C for 5 min and then cooling run was performed at a rate of 10 °C/min. Then, second heating run was carried out at a rate of 10°C/min.

3. Results and discussion

3.1. The structure and morphology of TA intercalated LDHs

The XRD pattern of TA intercalated LDHs is shown in Figure 1. For comparison, that of the carbonate LDHs prepared by a coprecipitation reaction is also presented in Figure 1. The XRD patterns exhibit the characteristic reflections of LDH materials with a series of (00l) peaks appearing as narrow symmetric lines at low angle corresponding to the basal spacing and higher order reflections. Compared to the carbonate LDHs, the basal spacing of the TA intercalated LDHs increases from 0.76 to 1.42 nm, which suggests the terephthalate anions were successfully intercalated. Given that the thickness of the brucite-like layer of LDHs is 0.48 nm [1], the gallery height in the TA intercalated LDHs is 0.94 nm. This data is same as the diameter of the long axis of terephthalate anion, which suggests a monolayer arrangement for the intercalated terephthalate anions oriented perpendicular to the LDH layers [26].

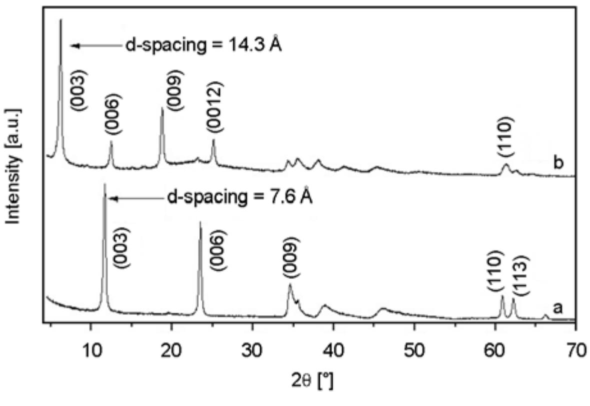

Figure 1. XRD patterns of different LDHs a) carbonate LDHs; b) TA intercalated LDHs

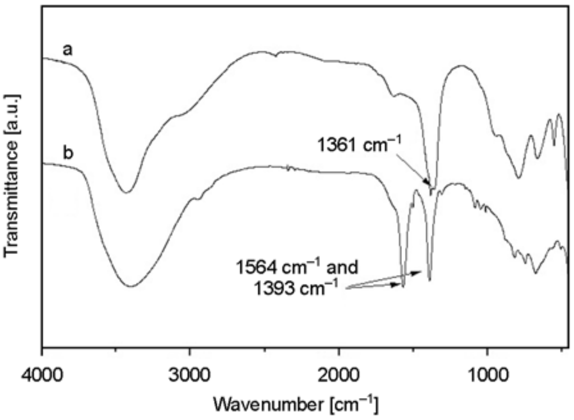

Figure 2. FT-IR spectra of different LDHs a) carbonate LDHs; b) TA intercalated LDHs

The FT-IR spectra of the carbonate LDHs and the TA intercalated LDHs are shown in Figure 2. The absorption at 1361 cm^{-1} which is attributed to carbonate ions in the carbonate LDHs is not present in the spectrum of the TA intercalated LDHs. The spectra of carboxylate are dominated by the asymmetric and symmetric RCO^{2-} stretches of the organic guests at around 1580 and 1400 cm^{-1} [27, 28]. As TA was incorporated into the LDH interlayers, two peaks appeared at 1564 and 1393 cm^{-1}, which are assigned to carboxylate group stretching of the terephthalate guest [23]. This confirms the existence of terephthalate anion in the interlayer of LDH sheets.

3.2. The structure and morphology of PET/LDH nanocomposites

The XRD patterns for PET and PET/LDH nanocomposites with 0.5, 1, 2 wt% of TA intercalated LDHs and 2 wt% of carbonate LDHs are shown in Figure 3. In the case of PET nanocomposites with 2 wt% of carbonate LDHs, a small (003) reflection (arrow mark) which corresponds to a basal spacing of carbonate LDHs is shown at around 11.3°. It indicates that the carbonate LDH particles were not exfoliated by the PET molecules during *in-situ* polymerization. In the cases of PET nanocomposites with TA intercalated LDHs, the characteristic peak of basal spacing for TA intercalated LDHs completely disappeared, indicating the partial exfoliation of LDHs interlayer structures in the PET matrix, in which the gallery height of intercalated

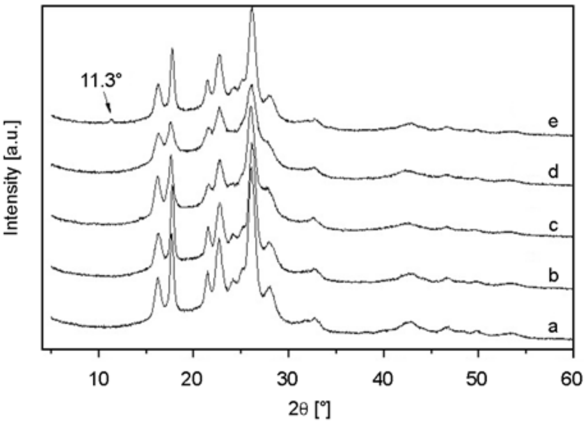

Figure 3. XRD patterns of PET (a) and PET/LDH nanocomposites with b) 0.5 wt% of TA intercalated LDHs; c) 1 wt% of TA intercalated LDHs; d) 2 wt% of TA intercalated LDHs; e) 2 wt% of carbonate LDHs

layers is large enough and the layer correlation is not detected by X-ray diffractometer. Although, XRD provides a partial picture about distribution of nanofiller and disappearance of peak corresponding to d-spacings does not always confirm the exfoliated nanocomposites [29], because XRD measurements detect average diffractions came from overall sample area irradiated by X-ray. If the characteristic peak shift to the lower angle beyond the XRD scan range (<3°) owing to increased gallery spacing resulting from the partial intercalation of PET molecules, then LDH characteristic diffractions for the gallery spacing cannot be detected by the XRD apparatus [6]. Therefore, a complete characterization of nanocomposite morphology requires to be investigated [30, 31].

The SEM images of PET nanocomposites with 2 wt% of carbonate LDHs and TA intercalated LDHs are shown in Figure 4. In Figure 4a, the particles of carbonate LDHs can be clearly seen. Some particles about 600 nm were shown, which were much bigger than the carbonate LDHs before polymerization. This is because the complete form of layered LDH aggregates. The carbonate LDHs had the least interaction with PET matrix, and were not intercalated by PET molecules during the polymerization. These layer structures can diffract the X-rays, resulting in the peak for LDH structure in XRD profiles which matches the XRD results

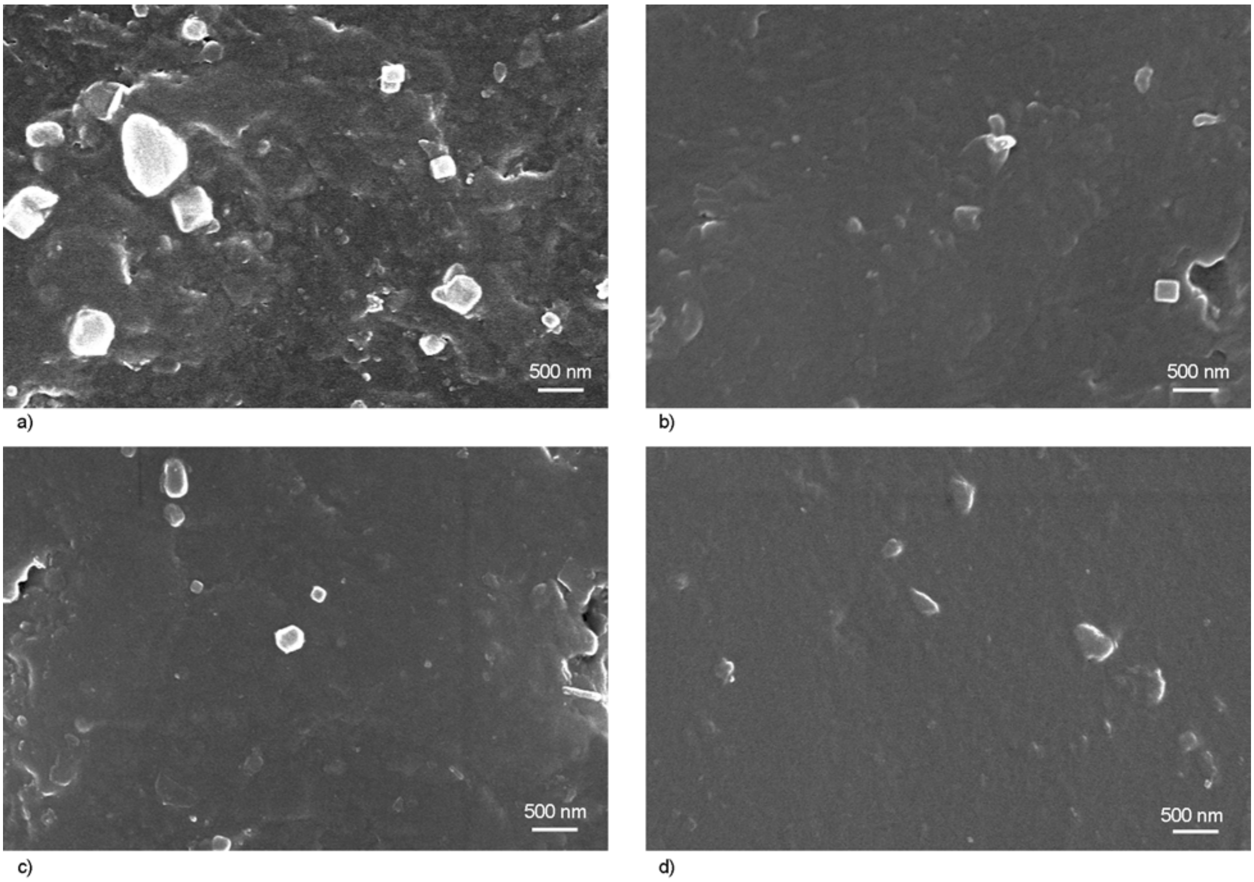

Figure 4. SEM images of the PET/LDH nanocomposites with a) 2 wt% of carbonate LDHs; b) 0.5 wt% of TA intercalated LDHs; c) 1 wt% of TA intercalated LDHs; d) 2 wt% of TA intercalated LDHs

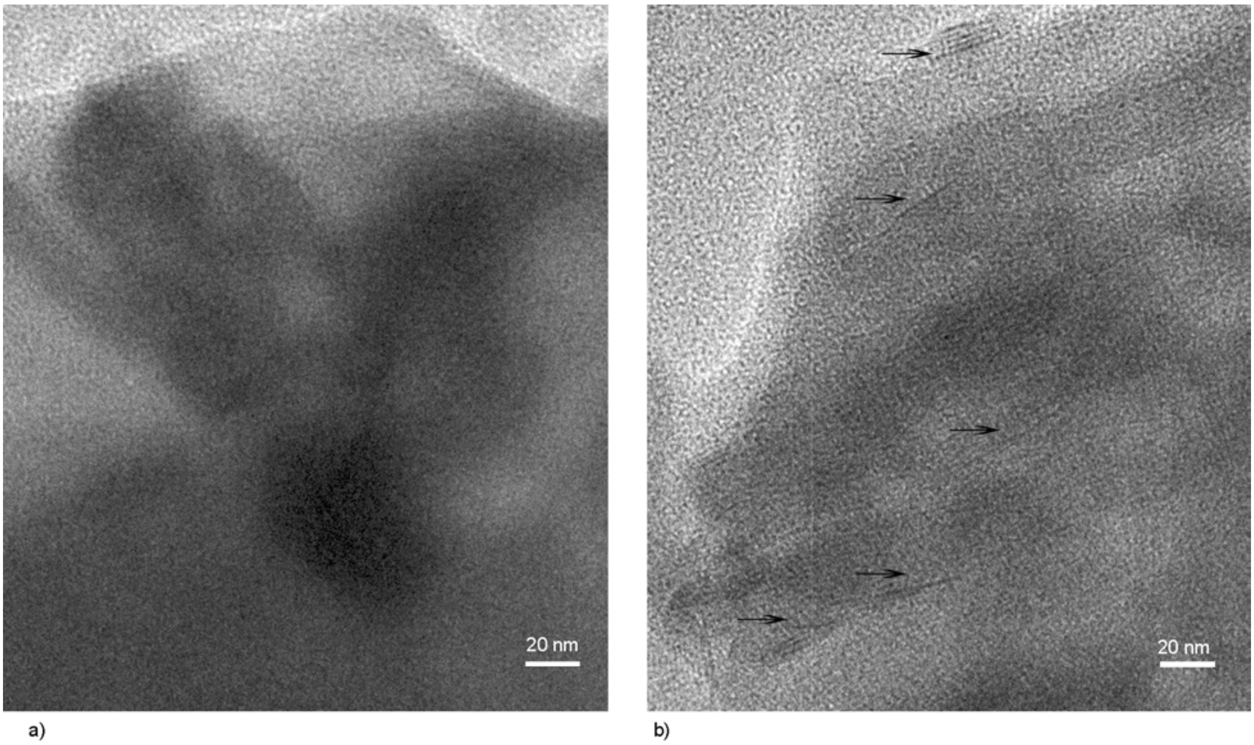

Figure 5. TEM images of the PET/LDH nanocomposites with a) 2 wt% of carbonate LDHs; b) 2 wt% of TA intercalated LDHs

shown in Figure 3. In Figure 4b, 4c and 4d, there was little agglomeration of the particles. Apparently, the particles of TA intercalated LDHs were less than that of carbonate LDHs in PET matrix with the same loading level (2%). It indicates that the TA intercalated LDHs were intercalated and/or exfoliated efficiently by PET molecules during polymerization and dispersed well in PET matrix.

TEM was used to examine exactly the state of the TA intercalated LDHs in the PET matrix. The TEM images taken from PET nanocomposites with 2 wt% of carbonate LDHs and 2 wt% TA intercalated LDHs are shown in Figure 5. The dark lines represent the LDH layers, whereas the bright areas represent PET matrix. In Figure 5a, big particles or aggregates are found because the carbonate LDHs were not intercalated by PET molecules during the in-situ polymerization. In Figure 5b, the micrograph clearly shows the lamellar structure of LDHs exfoliated by the PET macromolecular chain; the lines of the layers are well shown using the arrow marks. The thickness and lateral sizes of the exfoliated LDH layers can be calculated as being about 1~2 nm and 20~80 nm, respectively.

3.3. Thermal property and crystallization behavior of PET/LDH nanocomposites

TGA curves for PET and PET/LDH nanocomposites with 0.5, 1.0, and 2.0 wt% of TA intercalated LDHs and 2 wt% of carbonate LDHs are shown in Figure 6, and the results are summarized in Table 1. Decomposition of PET takes place in three steps [19]. The first weight loss starts at about 300°C, corresponds to removal of water. The main weight loss starts at about 400°C. This second step is attrib-

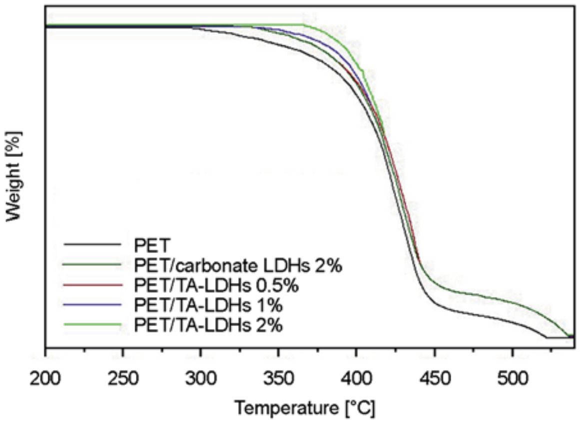

Figure 6. TGA curves of PET and PET/LDH nanocomposites with 2 wt% of carbonate LDHs and 0.5, 1, 2 wt% of TA intercalated LDHs

uted to the partial decomposition of the polymer. Finally, a new weight loss, due to oxidative elimination of the carbonaceous residue derived from the initial polymer degradation, is recorded at 470°C, and all the samples are finally lost at 520°C. In Figure 6, all the nanocomposites are more stable up to high temperature than pure PET, and show similar curves and slopes. The temperature at weight reduction of 2% (T^2_D) and 5% (T^5_D) for PET/LDH nanocomposites in Table 1 are also higher than those of pure PET. It indicates that there is a strong interaction between the TA-LDHs and polymer matrix. The exfoliated nanolayers of TA-LDHs obstructed the internal diffusion of intense heat and various gaseous substances that formed during pyrolysis of PET. Terephthalate is used to increase the basal spacing of the LDHs and overcome the lack of compatibility between the polymer and LDHs containing purely inorganic anions. The increasing of the basal spacing of the LDHs is helpful for the exfoliation of LDH layers. After polymerization, the characteristic XRD peak of basal spacing for TA intercalated LDHs completely disappeared, indicating the partial exfoliation of LDHs interlayer structures. The SEM and TEM images can show that the TA intercalated LDHs were partially exfoliated and well dispersed in PET matrix during polymerization. Thus, it is believed that the introduction of TA intercalated LDHs into the PET matrix can improve the thermal stability owing to the heat insulation effect of the LDH layers and the mass transport barrier against the volatile gases generated during thermal decomposition [6]. The thermal stability of PET/LDHs nanocomposites with 1% TA-LDHs is relatively higher than PET/LDHs nanocomposites with 2% TA-LDHs. This may be due to the dispersion of 1% TA-LDHs in the PET matrix is better than 2% according to the SEM images. The exfoliated nanolayers of PET/TA-LDHs 1% is more than that of 2%.

PET is a semicrystalline polymer and its properties are related to its morphological features such as degree of crystallization, size (thickness and lateral dimension of lamellae) and perfection of crystallites [32]. Therefore, it is important to study the crystallization behavior of PET/LDH nanocomposites. Figures 7 and 8 are the differential scanning calorimetry (DSC) thermograms of pure PET and PET/LDH nanocomposites with 2 wt% of carbonate LDHs and 0.5, 1, 2 wt% of TA intercalated LDHs with the heating and cooling measurements, respectively. The results of DSC are summarized in Table 1. The values of the melting peaks (T_m) of the

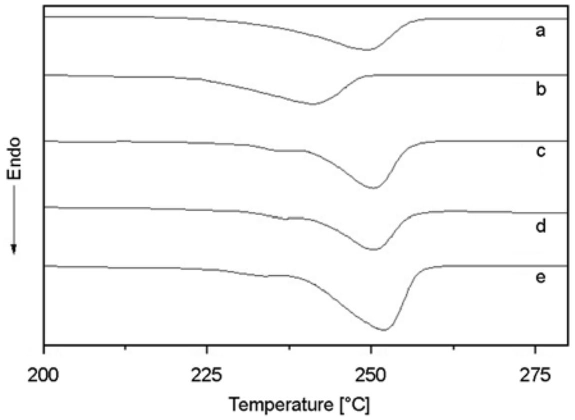

Figure 7. DSC thermograms of PET (a) and PET/LDH nanocomposites with 2 wt% of carbonate LDHs (b), 0.5 (c), 1 (d) and 2 (e) wt% TA intercalated LDHs during heating run

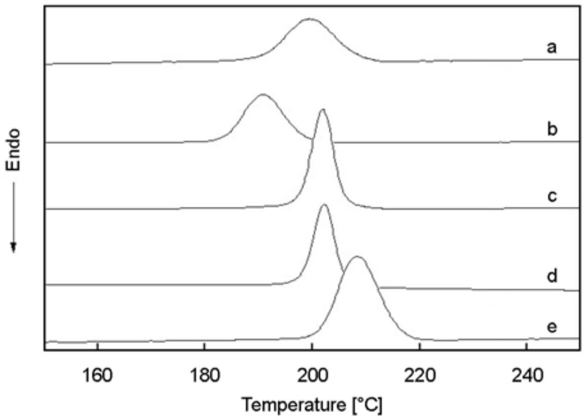

Figure 8. DSC thermograms of PET (a) and PET/LDH nanocomposites with 2 wt% of carbonate LDHs (b), 0.5 (c), 1 (d) and 2 (e) wt% TA intercalated LDHs during cooling run

Table 1. Thermal properties of PET and PET/LDH nanocomposites

Sample	T_m [°C]	ΔH_0 [J/g]	X_c [%]	T_{cc} [°C]	ΔT [°C]	T^2_D [°C]	T^5_D [°C]
PET	249.3	45.0	32	199.4	49.9	320	345
PET/carbonate LDHs 2%	241.0	38.6	28	190.7	50.3	349	368
PET/TA-LDHs 0.5%	250.2	53.4	38	201.9	48.3	329	358
PET/TA-LDHs 1%	250.3	50.0	36	202.2	48.1	377	386
PET/TA-LDHs 2%	251.8	72.7	53	208.3	43.5	354	374

nanocomposites increased from 249.3 to 251.8°C when the TA intercalated LDH content was increased from 0 to 2 wt%. The crystallization temperature during cooling (T_{cc}) of the nanocomposites increased from 199.4 to 208.3°C with increasing TA intercaltated LDH content. The crystallization temperature reflects the overall crystallization rate, attributed to the combined effects of nucleation and growth [33]. Thus the degree of super cooling ($\Delta T = T_m - T_{cc}$) can be used to represent the crystallizability of the polymer; that is, the smaller the ΔT, the higher the overall crystallization rate. As shown in Table 1, the degree of super cooling of the PET/TA intercalated LDH nanocomposites decreased.

The degree of crystallinity (X_c) of the samples were determined, which can be calculated using the Equation (1) [32]:

$$X_c = \frac{\Delta H_f}{\Delta H_f^0} \cdot 100 \qquad (1)$$

where ΔH_f^0 is the melting enthalpy of 100% crystalline PET (ΔH_f^0 = 140 J/g [34]) and ΔH_f is the normalized melting enthalpy of the sample, as shown by Equation (2):

$$\Delta H_f = \frac{\Delta H_0}{w} \qquad (2)$$

where ΔH_0 is the heat of fusion of PET/LDH nanocomposites [J/g], and w is the weight fraction of PET in the PET/LDH nanocomposite samples [wt%].

As shown in Table 1, the X_c values of the PET/TA-LDH nanocomposites are all higher than those of pure PET. These results suggest that small additions of TA intercalated LDHs increased the crystallization degree of polymer. The LDH nanofillers acted as a nucleating agent for the crystallization and accelerated the crystallization rate of the PET matrix [18]. On the other hand, The T_m and T_{cc} values of PET nanocomposites with 2 wt% of carbonate LDHs were decreased. TA-LDHs can be partially exfoliated and well dispersed in PET due to the larger interlayer space and the stronger interaction with PET matrix. The exfoliated nanolayers effectively promote the nucleation and crystallization of PET. However, the carbonate LDHs had the least interaction with polymer matrix and did not have good compatibility with PET molecules. The carbonate LDHs were not exfoliated and agglomerated in the PET matrix. Therefore they cannot act as a nucleating agent of crystallization.

4. Conclusions

The PET/LDH nanocomposites were prepared by *in-situ* polymerization. Their structure, morphology, thermal property and crystallization behavior were investigated. To enhance the compatibility between PET matrix and LDHs, TA intercalated LDHs were prepared using hydroxides as raw materials. Compared to the agglomeration of carbonate LDHs in PET matrix, TA intercalated LDHs could be partially exfoliated by PET molecules during in-situ polymerization and dispersed well in the PET matrix. The nanocomposites thus obtained were thermally more stable than pure PET. The addition of LDHs which acted as a nucleating agent resulted in an increase in crystallization rate.

References

[1] Cavani F., Trifirò F., Vaccari A.: Hydrotalcite-type anionic clays: Preparation, properties and applications. Catalysis Today, **11**, 173–301 (1991). DOI: 10.1016/0920-5861(91)80068-K

[2] Evans D. G., Xue D.: Preparation of layered double hydroxides and their applications as additives in polymers, as precursors to magnetic materials and in biology and medicine. Chemical Communications, **2006**, 485–496 (2006). DOI: 10.1039/b510313b

[3] O'Leary S., O'Hare D., Seeley G.: Delamination of layered double hydroxides in polar monomers: New LDH-acrylate nanocomposites. Chemical Communications, **2002**, 1506–1507 (2002). DOI: 10.1039/b204213d

[4] Hsueh H-B., Chen C-Y.: Preparation and properties of LDHs/polyimide nanocomposites. Polymer, **44**, 1151–1161 (2003). DOI: 10.1016/S0032-3861(02)00887-X

[5] Hsueh H-B., Chen C-Y.: Preparation and properties of LDHs/epoxy nanocomposites. Polymer, **44**, 5275–5283 (2003). DOI: 10.1016/S0032-3861(03)00579-2

[6] Lee W. D., Im S. S.: Thermomechanical properties and crystallization behavior of layered double hydroxide/poly(ethylene terephthalate) nanocomposites prepared by in-situ polymerization. Journal of Polymer Science Part B: Polymer Physics, **45**, 28–40 (2007). DOI: 10.1002/polb.20993

[7] Zammarano M., Bellayer S., Gilman J. W., Franceschi M., Beyer F. L., Harris R. H., Meriani S.: Delamination of organo-modified layered double hydroxides in polyamide 6 by melt processing. Polymer, **47**, 652–662 (2006).
DOI: 10.1016/j.polymer.2005.11.080

[8] Berti C., Fiorini M., Sisti L.: Synthesis of poly(butylene terephtahlate) nanocomposites using anionic clays. European Polymer Journal, **45**, 70–78 (2009).
DOI: 10.1016/j.eurpolymj.2008.09.039

[9] Pereira C. M. C., Herrero M., Labajos F. M., Marques A. T., Rives V.: Preparation and properties of new flame retardant unsaturated polyester nanocomposites based on layered double hydroxides. Polymer Degradation and Stability, **94**, 939–946 (2009).
DOI: 10.1016/j.polymdegradstab.2009.03.009

[10] Li B., Hu Y., Zhang R., Chen Z., Fan W.: Preparation of the poly(vinyl alcohol)/layered double hydroxide nanocomposite. Materials Research Bulletin, **38**, 1567–1572 (2003).
DOI: 10.1016/S0025-5408(03)00203-4

[11] Zhang Z., Zhu M., Sun B., Zhang Q., Yan C., Fang S.: The effect of hydrotalcite and zinc oxide on smoke suppression of commercial rigid PVC. Journal of Macromolecular Science Part A: Pure and Applied Chemistry, **43**, 1807–1814 (2006).
DOI: 10.1080/10601320600940930

[12] Meyn M., Beneke K., Lagaly G.: Anion-exchange reactions of layered double hydroxides. Inorganic Chemistry, **29**, 5201–5207 (1990).
DOI: 10.1021/ic00351a013

[13] Newman S. P., Jones W.: Synthesis, characterization and applications of layered double hydroxides containing organic guests. New Journal of Chemistry, **22**, 105–115 (1998).
DOI: 10.1039/a708319j

[14] Kovanda F., Jindová E., Lang K., Kubát P., Sedláková Z.: Preparation of layered double hydroxides intercalated with organic anions and their application in LDH/poly(butyl methacrylate) nanocomposites. Applied Clay Science, **48**, 260–270 (2010).
DOI: 10.1016/j.clay.2009.11.012

[15] Káfuňková E., Taviot-Guého C., Bezdička P., Klementová M., Kovář P., Kubát P., Mosinger J., Pospíšil M., Lang K.: Porphyrins intercalated in Zn/Al and Mg/Al layered double hydroxides: Properties and structural arrangement. Chemistry of Materials, **22**, 2481–2490 (2010).
DOI: 10.1021/cm903125v

[16] Costa F. R., Leuteritz A., Wagenknecht U., Jehnichen D., Häußler L., Heinrich G.: Intercalation of Mg–Al layered double hydroxide by anionic surfactants: Preparation and characterization. Applied Clay Science, **38**, 153–164 (2008).
DOI: 10.1016/j.clay.2007.03.006

[17] Gago S., Costa T., de Melo J. S., Gonçalves I. S., Pillinger M.: Preparation and photophysical characterisation of Zn–Al layered double hydroxides intercalated by anionic pyrene derivatives. Journal of Materials Science, **18**, 894–904 (2008).
DOI: 10.1039/b715319h

[18] Lee W. D., Im S. S., Lim H-M., Kim K-J.: Preparation and properties of layered double hydroxide/poly(ethylene terephthalate) nanocomposites by direct melt compounding. Polymer, **47**, 1364–1371 (2006).
DOI: 10.1016/j.polymer.2005.12.056

[19] Martínez-Gallegos S., Herrero M., Rives V.: *In situ* microwave-assisted polymerization of polyethylene terephtalate in layered double hydroxides. Journal of Applied Polymer Science, **109**, 1388–1394 (2008).
DOI: 10.1002/app.28215

[20] Martínez-Gallegos S., Herrero M., Barriga C., Labajos F. M., Rives V.: Dispersion of layered double hydroxides in poly(ethylene terephthalate) by *in situ* polymerization and mechanical grinding. Applied Clay Science, **45**, 44–49 (2009).
DOI: 10.1016/j.clay.2009.04.007

[21] Herrero M., Martínez-Gallegos S., Labajos M., Rives V.: Layered double hydroxide/polyethylene terephthalate nanocomposites. Influence of the intercalated LDH anion and the type of polymerization heating method. Journal of Solid State Chemistry, **184**, 2862–2869 (2011).
DOI: 10.1016/j.jssc.2011.08.017

[22] Chang J-H., Mun M-K., Lee I. C.: Poly(ethylene terephthalate) nanocomposite fibers by *in situ* polymerization: The thermomechanical properties and morphology. Journal of Applied Polymer Science, **98**, 2009–2016 (2005).
DOI: 10.1002/app.22382

[23] Cui W., Jiao Q., Zhao Y., Zhou M.: Preparation of carboxylate-intercalated layered double hydroxides using mixed hydroxides or oxides. Micro and Nano Letters, **6**, 832–835 (2011).
DOI: 10.1049/mnl.2011.0323

[24] Jiao Q., Cui W., Zhao Y.: A method for the preparation of organic acid anions intercalated layered double hydroxides. CN102009959A, P. R. China (2011).

[25] Chang J-H., Kim S. J., Joo Y. L., Im S.: Poly(ethylene terephthalate) nanocomposites by in situ interlayer polymerization: The thermo-mechanical properties and morphology of the hybrid fibers. Polymer, **45**, 919–926 (2004).
DOI: 10.1016/j.polymer.2003.11.037

[26] Newman S. P., Williams S. J., Coveney P. V., Jones W.: Interlayer arrangement of hydrated MgAl layered double hydroxides containing guest terephthalate anions: Comparison of simulation and measurement. Journal of Physical Chemistry B, **102**, 6710–6719 (1998).
DOI: 10.1021/jp981426r

[27] Prevot V., Forano C., Besse J. P.: Syntheses and thermal and chemical behaviors of tartrate and succinate intercalated Zn_3Al and Zn_2Cr layered double hydroxides. Inorganic Chemistry, **37**, 4293–4301 (1998)
DOI: 10.1021/ic9801239

[28] Zhang H., Zhang F., Ren L., Evans D. G., Duan X.: Synthesis of layered double hydroxide anionic clays intercalated by carboxylate anions. Materials Chemistry and Physics, **85**, 207–214 (2004)
DOI: 10.1016/j.matchemphys.2004.01.020

[29] Acharya H., Srivastava S. K., Bhowmick A. K.: Synthesis of partially exfoliated EPDM/LDH nanocomposites by solution intercalation: Structural characterization and properties. Composites Science and Technology, **67**, 2807–2816 (2007).
DOI: 10.1016/j.compscitech.2007.01.030

[30] Morgan A. B., Gilman J. W.: Characterization of polymer-layered silicate (clay) nanocomposites by transmission electron microscopy and X-ray diffraction: A comparative study. Journal of Applied Polymer Science, **87**, 1329–1338 (2003).
DOI: 10.1002/app.11884

[31] Yu Z-Z., Yang M. S., Zhang Q., Zhao C., Mai Y-W.: Dispersion and distribution of organically modified montmorillonite in nylon-66 matrix. Journal of Polymer Science Part B: Polymer Physics, **41**, 1234–1243 (2003).
DOI: 10.1002/polb.10480

[32] He J-P., Li H-M., Wang X-Y., Gao Y.: In situ preparation of poly(ethylene terephthalate)–SiO_2 nanocomposites. European Polymer Journal, **42**, 1128–1134 (2006).
DOI: 10.1016/j.eurpolymj.2005.11.002

[33] Ou C. F., Ho M. T., Lin J. R.: Synthesis and characterization of poly(ethylene terephthalate) nanocomposites with organoclay. Journal of Applied Polymer Science, **91**, 140–145 (2004).
DOI: 10.1002/app.13158

[34] Jandali M. Z., Widmann G.: Application handbook of thermal analysis: Thermoplastics. Donghua University Press, Shanghai (2008).

eXPRESS Polymer Letters Vol.6, No.6 (2012) 494–502
Available online at www.expresspolymlett.com
DOI: 10.3144/expresspolymlett.2012.52

Electrical resistivity and thermal properties of compatibilized multi-walled carbon nanotube/polypropylene composites

A. Szentes[1*], *Cs. Varga*[2], *G. Horváth*[1], *L. Bartha*[2], *Z. Kónya*[3], *H. Haspel*[3], *J. Szél*[3], *Á. Kukovecz*[3]

[1]University of Pannonia, Institutional Department of Chemical Engineering Science, H-8200 Veszprém, Egyetem u. 10, Hungary
[2]University of Pannonia, Institutional Department of MOL Hydrocarbon and Coal Processing, H-8200 Veszprém, Egyetem u. 10, Hungary
[3]University of Szeged, Department of Applied and Environmental Chemistry, H-6720 Szeged, Rerrich Béla tér 1, Hungary

Received 26 October 2011; accepted in revised form 15 January 2012

Abstract. The electrical resistivity and thermal properties of multi-walled carbon nanotube/polypropylene (MWCNT/PP) composites have been investigated in the presence of coupling agents applied for improving the compatibility between the nanotubes and the polymer. A novel olefin-maleic-anhydride copolymer and an olefin-maleic-anhydride copolymer based derivative have been used as compatibilizers to achieve better dispersion of MWCNTs in the polymer matrix. The composites have been produced by extrusion followed by injection moulding. They contained different amounts of MWCNTs (0.5, 2, 3 and 5 wt%) and coupling agent to enhance the interactions between the carbon nanotubes and the polymer. The electrical resistivity of the composites has been investigated by impedance spectroscopy, whereas their thermal properties have been determined using a thermal analyzer operating on the basis of the periodic thermal perturbation method. Rheological properties, BET-area and adsorption-desorption isotherms have been determined. Dispersion of MWCNTs in the polymer has been studied by scanning electron microscopy (SEM).

Keywords: *polymer composites, multi-walled carbon nanotubes, polypropylene, electrical resistivity, thermal conductivity*

1. Introduction

Carbon nanotubes (CNTs) are promising reinforcing fillers for polymers due to their excellent mechanical, electrical and thermal properties [1]. Recently the coupling of physical and mechanical properties particularly has achieved widespread interest in the area of carbon nanotube composites. Although polymer matrices of composites are generally considered as non-conductive materials because of their extremely low electrical conductivity, conductive polymer composites can be formed by application of conductive fillers, like CNTs [2–6]. Electrical conductivity of the composite is highly dependent on the volume fraction of the conductive phase. There is a lower limit for volume fraction of the filler, called percolation threshold, at which conductivity of the composite increases by many orders of magnitude. Depending on the matrix, the processing technique, and the nanotube type, wide (0.001 to 10 wt%) range of percolation thresholds has been reported in the literature so far [6]. Low values for percolation threshold can be achieved by a well-dispersed structure of CNTs in the polymer matrix.

However, commercial application of CNTs by the plastics industry has been limited so far because they are difficult to disperse in polymer matrices. Inhomogeneous CNT dispersion results in the sig-

---

[*]Corresponding author, e-mail: szentesa@almos.uni-pannon.hu

nificant deterioration of the mechanical properties of the end-product [1], therefore, it is important to reduce the agglomeration and increase the dispersion of carbon nanotubes, thus achieving a homogeneous distribution of the nanotubes in the polymer matrix. The latter is important in order to avoid the deterioration of the mechanical and functional properties of carbon nanotube polymer composites [7, 8].

Carbon nanotubes are non-polar materials containing only a few functional groups that could react with polymers, therefore, different methods have been developed to achieve stronger interaction between carbon nanotubes and polymers. Modification methods of CNTs can be divided into two main categories based on the type of bonding to the nanotube surface. Non-covalent modification means the physical adsorption and/or wrapping of polymers to the surface of CNTs. The graphitic walls of CNTs provide the possibility for π-stacking interactions with conjugated polymers as well as with polymers containing heteroatoms possessing at least one free electron pair. On the other hand, covalent bonding (grafting) of polymer chains to the CNTs corresponds to establishing strong chemical bonds between the nanotubes and the polymer. Grafting is either ‘grafting to’ or ‘grafting from’. In the first case a polymer with reactive end-groups can be bonded to the CNT, whereas in the latter case monomers can be reacted with the surface in the presence of radical initiators followed by the polymerization reaction of the monomers.

The advantage of non-covalent functionalization is that the interaction does not perturb the structure of the carbon nanotubes, because additives only adhere to the surface of the nanotubes, therefore, the advantageous CNT properties originating from the continuous sp^2 hybrid structure are retained [9–11]. Additives used for non-covalent functionalization of CNTs are referred to as coupling agents or compatibilizers. Their function is to establish proper interaction between carbon nanotubes and polymer matrix and to prevent the formation of nanotube agglomerates, therefore, they are chosen on the basis of the chemical composition of the reinforcing material and the polymer.

There are several well-known types of compatibilizers, for example maleic-anhydride grafted polyolefins (MA-g-PO) or silane type additives are generally applied to enhance the compatibility of glass or carbon fibers both with thermoplastics and thermosets [12–14]. Maleic-anhydride grafted polymers can be only blended to the polymer/nanotube mixture, therefore only the dispersion of the CNTs can be improved [15, 16] but CNT/polymer interaction cannot be significantly modified. For improving the bonding between them special methods are required that are able to establish strong connection between functional groups.

In this contribution we report on the applicability of a new olefin-maleic-anhydride copolymer and its ester-amide derivative for enhancing the compatibility of multi-walled carbon nanotubes with a polypropylene matrix based on previously successful results in carbon fiber reinforced polyolefin and glass fiber reinforced polyester composites [17–19]. The novel aspect of our work is that the MWCNTs were synthesized by our proprietary heterogeneous catalytic method which has been scaled up successfully at the University of Pannonia, Hungary. This method has been specifically designed to produce large quantities of cheap MWCNTs for polymer filler applications and therefore, the catalyst support talc (approx. 10 wt%) is not removed from the product at all. The electrical and thermal properties of the synthesized composites are compared with reference samples containing carbon black, commercial Nanocyl MWCNTs and carbon-free talc. We will demonstrate that the behavior of composites containing cheap MWCNT/talc nanotubes compares favourably with that of composites based on more expensive commercial carbon nanotubes.

2. Experimental

2.1. Materials

Multi-walled carbon nanotubes (MWCNT) were produced at 700°C by chemical vapor deposition (CVD) process over Fe–Co bimetallic catalyst at the Institutional Department of Chemical Engineering (Institute of Chemical and Process Engineering, University of Pannonia, Veszprém, Hungary) [20]. Their diameter was between 10 and 20 nm and their average length was above 30 µm. The synthesized nanotubes were not separated from the talc support, thus the produced filler material (denoted as UPNT from now on) consisted of 90 wt% MWCNTs and 10 wt% talc. Polypropylene (PP) homopolymer (H116F, TVK Plc, Tiszaújváros, Hungary melt flow

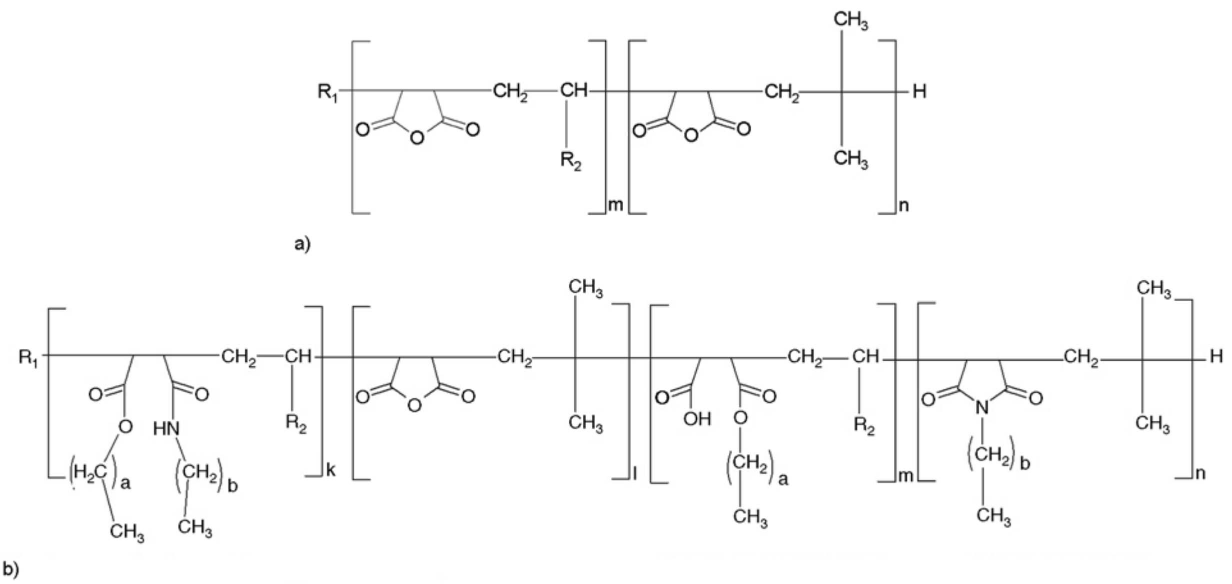

Figure 1. Structure of the olefin-maleic-anhydride copolymer (OMA) where R_1: alkyl chain with length of the olefinic monomer; R_2: alkyl chain with R_{1-2} carbon number; *m*, *n*: 5–9 (a) and structure of the olefin-maleic-anhydride-ester-amide copolymer (OMAEA) where R_1: alkyl chain with length of the olefinic monomer; R_2: alkyl chain with R_{1-2} carbon number; *a*, *b*: 2–21; *k*: 0.2–2; l: 1–7; *m*: 1–7 and *n*: 0.3–2 (b)

rate 28.0 g/10 min at 190°C, 2.16 kg) was used as the matrix material. An olefin-maleic-anhydride copolymer (OMA) (Figure 1a) and an olefin-maleic-anhydride-ester-amide (OMAEA) (Figure 1b) were used as compatibilizers. Both were synthesized at the Institutional Department of MOL Hydrocarbon and Coal Processing (Institute of Chemical and Process Engineering, University of Pannonia).

Multi-walled carbon nanotubes from Nanocyl S. A. Belgium (NC7000: MWCNT 90 wt% carbon purity for industrial applications, signed by 'NC' in the followings), talc (Thomasker Finechemicals Ltd, Hungary) and carbon black (denoted as CB, type K-354, purchased from Carbon Black Ltd, Hungary) were used as reference materials.

Table 1. Composition of the compatibilizer-free PP composites

Sample	PP [wt%]	MWCNT [wt%]	Carbon black [wt%]	Talc (or *other) [wt%]
PP	100			
PP/UPNT/0.5	99.5	0.45		0.05
PP/UPNT/2	98	1.8		0.2
PP/UPNT/3	97	2.7		0.3
PP/UPNT/5	95	4.5		0.5
PP/NC/0.5	99.5	0.45		*0.05
PP/NC/2	98	1.8		*0.2
PP/NC/3	97	2.7		*0.3
PP/NC/5	95	4.5		*0.5
PP/CB/talc/0.5	99.5		0.45	0.05
PP/CB/talc/2	98		1.8	0.2
PP/CB/talc/3	97		2.7	0.3
PP/CB/talc/5	95		4.5	0.5

2.2. Preparation of composites

The composition of all compatibilizer-free PP composites is summarized in Table 1. In order to compare composites filled with carbon materials in different forms, not only our CNT product (UPNT) was introduced into PP matrix but also carbon black (CB) and commercially available CNT (NC) were applied. As UPNT contained talc as a catalyst carrier in 10 wt%, composites filled with that talc content were also produced. Nanocyl MWCNTs contained 10 wt% undisclosed catalyst support material according to the product datasheet. This was also taken into account in Table 1 in the rows marked with an asterisk (*other).

Coupling agents (OMA and OMAEA) were tested in PP/UPNT composites using two different application methods. In the masterbatch method (MB) a masterbatch was produced from the coupling agent and PP in 1:9 mass ratio then the masterbatch was mixed with the neat PP and UPNT in a twin-screw extruder.

In the impregnation method (IM) the surface of UPNT was covered by the coupling agent from the

Table 2. Composition of the compatibilized carbon nanotube/polypropylene composites

Sample	PP [wt%]	UPNT [wt%]	OMA [wt%]	OMAEA [wt%]
OMA/MB/0.5	99.45	0.5	0.05	
OMA/MB/2	97.8	2	0.2	
OMA/MB/3	96.7	3	0.3	
OMA/MB/5	94.5	5	0.5	
OMAEA/MB/0.5	99.45	0.5		0.05
OMAEA/MB/2	97.8	2		0.2
OMAEA/MB/3	96.7	3		0.3
OMAEA/MB/5	94.5	5		0.5
OMA/IM/0.5	99.45	0.5	0.05	
OMA/IM/2	97.8	2	0.2	
OMA/IM/3	96.7	3	0.3	
OMA/IM/5	94.5	5	0.5	
OMAEA/IM/0.5	99.45	0.5		0.05
OMAEA/IM/2	97.8	2		0.2
OMAEA/IM/3	96.7	3		0.3
OMAEA/IM/5	94.5	5		0.5

hydrocarbon solution of the additive with stirring of the mixture for 1 hour at 60°C. The solvent was subsequently evaporated; the treated UPNTs were dried at 110°C for 2 hours in air and were finally introduced into the neat polymer in the twin-screw extruder. Compounds were prepared by extrusion. A twin-screw extruder was applied with different zone temperatures (195, 200, 205, 210°C) for introducing the fillers into the polymer. Dog-bone samples for testing were injection-moulded.

Specimens for electrical and thermal measurements were also injection-moulded. Compositions of the PP/UPNT composites containing coupling agents are summarized in Table 2.

2.3. Characterization

The electrical resistivity (ρ [Ωm]) of the composites was determined in the 10^{-1}–10^{7} Hz frequency range using a Novocontrol Alpha-A (Novocontrol, Hundsangen, Germany) modular measurement system connected to a ZG2 2-wire impedance interface and a BDS1200 sample holder. The electrical contact between the sample and the instrument was improved by sputtering a 20 nm thick silver film onto both sides of the thin sample disks using a Polaron SC7620 Mini Sputter Coater (Quorum Technologies, Ashford, UK). The complex impedance of the samples was measured in capacitor geometry and converted to specific electrical resistance by taking the geometry of the sample into account.

The thermal conductivity and thermal diffusivity of thin sample disks were determined simultaneously in a purpose-built instrument utilizing the periodic thermal perturbation method. In this technique the sample disk is sandwiched between two copper blocks in vacuum and the temperature of the bottom block is continuously modulated by a sum of several sinusoid thermal waves of different frequencies. As these waves travel across the sample their amplitude is reduced and their phase is shifted as determined by the thermal properties of the studied material. By monitoring the temperature of the upper block as a function of time and Fourier transforming this signal to obtain the propagation properties of the individual thermal waves it is possible to calculate the heat transfer function of the sample, which in turn can be used to calculate the thermal conductivity and thermal diffusivity [21].

The specific surface area and pore size distribution in the micropore, mesopore, and macropore diameter ranges were determined by nitrogen adsorption/desorption isotherms measured with a Micromeritics ASAP 2000-type instrument (Micromeritics, Aachen, Germany). The samples previously gassed out in vacuum at the temperature of 100°C. The surface areas of the samples were determined by the BET method from the corresponding nitrogen adsorption isotherm [22]. The meso and macropore volume values were calculated from the nitrogen desorption isotherms using the BJH (Barret–Joyner–Halenda) theory [23].

Rheological measurements were carried out by a Smart Rheo 2000 (CEAST, Italy) capillary rheometer at 210°C in 2 to 1500 1/s shear rate range.

The composite fracture surfaces were characterized by scanning electron microscopy (SEM) using a Hitachi S-4700 Type II cold field emission instrument (Hitachi, Tokyo, Japan). Samples for SEM were coated with a thin (<4 nm) gold-palladium layer deposited by argon plasma sputter coating to avoid charging effects.

3. Results and discussion

3.1. Electrical resistivity of the composites

The electrical resistivity of a MWCNT/polymer composite depends on the size, shape, concentration, distribution and surface treatment of nanotubes [24]. In Figure 2 the effect of all tested fillers on the electrical resistivity of compatibilizer-free

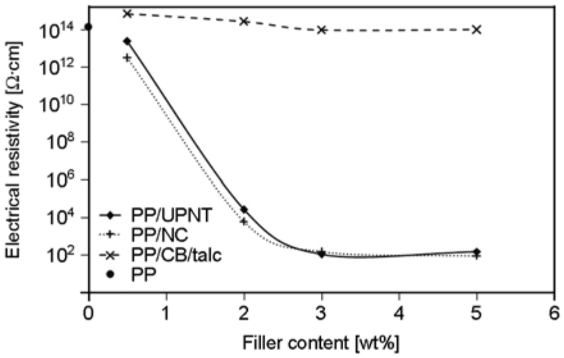

Figure 2. Electrical resistivity of the compatibilizer-free polypropylene composites

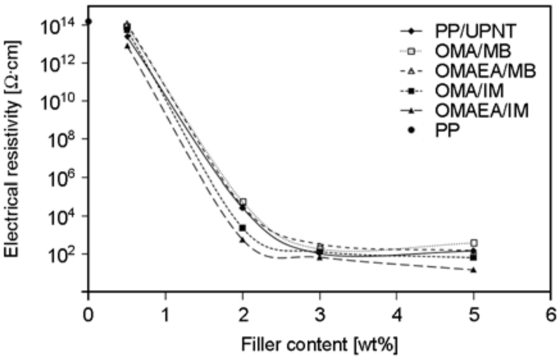

Figure 3. Electrical resistivity of compatibilized carbon nanotube/polypropylene composites

polypropylene is depicted for various filler concentrations (0.5, 2, 3 and 5 wt%).

It is evident from Figure 2 that while neat PP exhibits very high electrical resistivity ($1.43\cdot10^{14}$ Ω cm), this can be decreased significantly by introducing CNTs into the polymer. At low nanotube contents a proper percolating network structure could not be established in the polymer matrix, therefore, the electrical resistivity of those samples remained high. When increasing the filler content above 2 wt% a continuous nanotube network was obtained as indicated by the significant drop in the resistivity. The electrical resistivity of 2 wt% UPNT containing composite was $2.61\cdot10^{4}$ Ω cm. It is worth noting that adding more MWCNTs to the composite above the threshold concentration level of approx. 3 wt% cannot improve the conductivity any further. The PP/UPNT and PP/NC composites exhibited very similar behavior in the whole concentration range. The nanotube-related origin of the improved electrical conductivity was confirmed by the lack of resistivity decrease in the case of PP/carbon black/talc composites. Further studies would be necessary to uncover the reasons of the minor resistivity increase relative to PP observed for low carbon black/talc concentration levels. The most plausible explanation is that although the filler did not actually modify the electrical conductivity of the composite, it affected the density of the samples and this translated into a slight resistivity increase when calculating the specific resistivity from the raw impedance data.

In Figure 3 the effect of the coupling agents on the electrical resistivity of PP/CNT composites is depicted. The general trends identified for compatibilizer-free samples can be observed here as well. However, composites produced by the masterbatch method (OMA/MB and OMAEA/MB) exhibited resistivities that were several times higher than those measured on the corresponding impregnation method samples or compatibilizer-free PP/CNT composites. On the other hand, the impregnation method offered approx. one order of magnitude improvement in electrical conductivity over the corresponding pristine PP/CNT composites. Summarizing, it appears that simply blending the coupling agent into the polymer matrix hinders the nanotube-to-nanotube electron transfer, whereas immobilizing it on the carbon nanotube surface (impregnation method) actually promotes conduction.

The electrical resistivity of masterbatch samples was practically independent of the chemical structure of the coupling agent. This was not the case for impregnated samples, as the conductivity of OMAEA/IM samples was higher than that of OMA/IM samples. The electrical resistivity of the OMAEA/IM sample was 570 Ω cm, while that of OMA/IM samples was 2250 Ω cm in case of 2 wt% CNT content. Further investigations are necessary to uncover the exact role of the anhydride, half-ester, imide and ester-amide functional groups in the conductivity improvement process.

3.2. Thermal properties of the composites

The thermal conductivity coefficient (k [W/(mK)]) of polypropylene was found to be independent of the carbon black and talc concentration (Figure 4). On the other hand, adding carbon nanotubes to the polymer improved its thermal conductivity as a linear function of CNT content. UPNT nanotubes performed significantly better than the reference NC nanotubes as indicated by the steeper slope of the

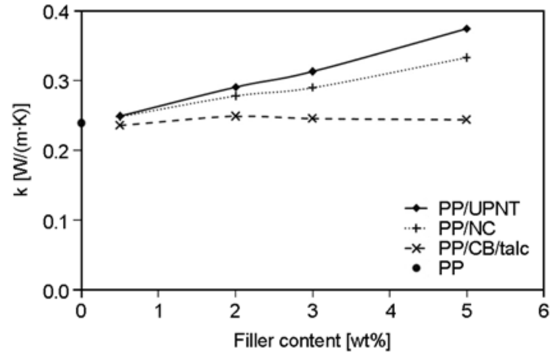

Figure 4. The thermal conductivity coefficient of compatibilizer-free polypropylene composites

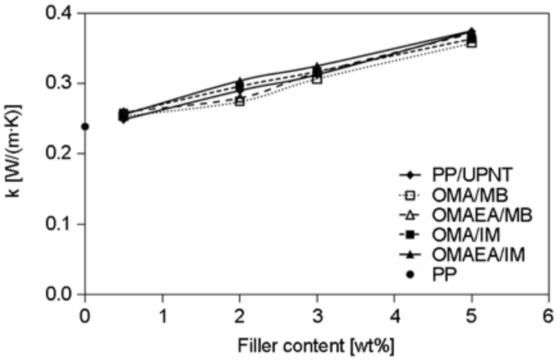

Figure 5. The thermal conductivity coefficient of compatibilized carbon nanotube/polypropylene composites

corresponding curve in Figure 4. For example, the thermal conductivity coefficient was 0.332 W/(mK) for NC and 0.374 W/(mK) for UPNT at 5 wt% nanotube concentration, which meant 40 and 57% thermal conductivity increase relative to PP (0.238 W/(mK)).

Neither the chemical structure nor the application method of the coupling agent affected the thermal conductivity of the composites. Figure 5 shows that thermal conductivity coefficient values measured for different materials at the same CNT content agreed within ±5%.

3.3. Effects of surface treatment

Effects of treatment on the properties of CNTs were also studied. BET-area and adsorption-desorption isotherms of untreated UPNT and additive treated UPNT (OMAEA/IM) were determined (Figure 6). BET-area of the pristine UPNT was 180.9 m^2/g, whereas for surface treated UPNT 91.1 m^2/g value was measured. Treatment with the coupling agent had a significant influence on the isotherms of the CNTs unambiguously due to the coupling agent. Capability of CNT for gas adsorption decreased by 40% when the additive was connected to the surface. Difference between the isotherms of pristine CNT and additive treated CNT did not change in the whole investigated pressure range. Additive sizing on the CNT was stable even at 100°C temperature since the coupling agent could not be removed from the surface even in vacuum.

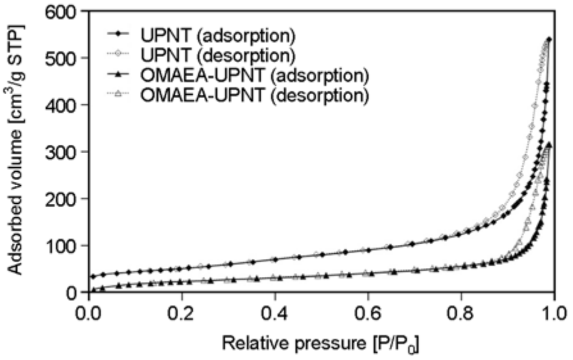

Figure 6. Adsorption-desorption isotherms of UPNT and OMAEA additive treated UPNT

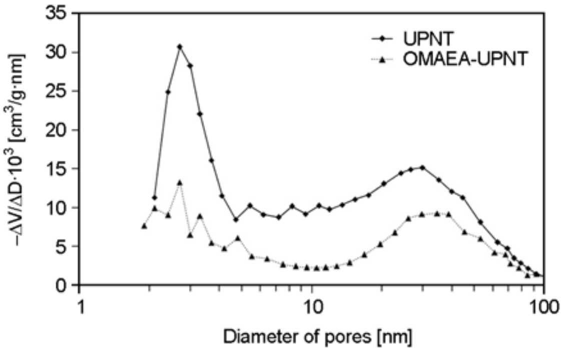

Figure 7. Distribution of diameter of mesopores

Regarding the distribution of diameter of mesopores (Figure 7) the additive seemed to shield the smaller pores with diameter of 2.5–4.0 nm. That could be one reason for the additive treated CNT not to hinder the transfer of the electrons in the composites because the additive could be found on the surface. The connection of the additive to the surface could be one reason for better electron transfer in treated PP/CNT composites.

3.4. Rheological properties of composites

Rheological properties can reflect the structure of nanotube-containing composites and provide information about the interaction between the nanoparticles and the polymer matrix. Therefore evaluation of rheological behaviour of the composites is important in order to understand the effect of nanotubes on the structure [24].

We measured the viscosity of PP composites containing 2 wt% UPNT nanotubes and depicted the results in Figure 8. In agreement with received wisdom, adding nanotubes to PP without a coupling agent increased its viscosity [24–28]. Composites produced with nanotubes and OMAEA compatibilizer (OMAEA/MB) all featured lower viscosities than their compatibilizer-free counterparts (PP/UPNT) because of the plasticizing effect of the additive. At low shear rates the effect was observable for both composite preparation methods. Whereas the masterbatch samples maintained this viscosity decrease in the whole studied shear rate range, composites prepared by OMAEA impregnation exhibited a more complex behaviour. They resembled masterbatch samples at low shear rates and compatibilizer-free PP/UPNT composites at high shear rates.

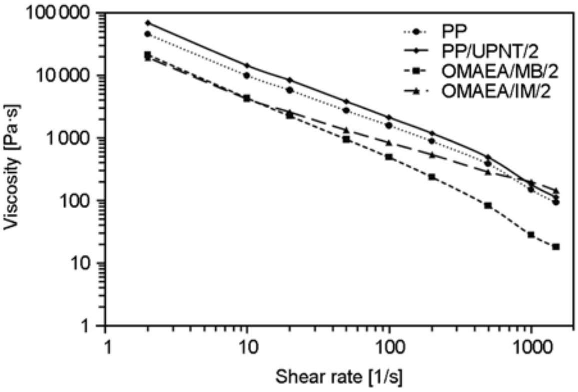

Figure 8. Comparison of rheological properties of composites containing coupling agents

3.5. Investigation by SEM

Dispersion state of carbon nanotubes in the PP matrix was investigated by scanning electron microscopy (SEM). SEM images were taken of the composites filled with 2 wt% carbon nanotubes. Pristine carbon nanotubes (UPNT) seemed to form agglomerates (Figure 9a–9c). Lumps can be seen in certain locations at the surface of the composites. In

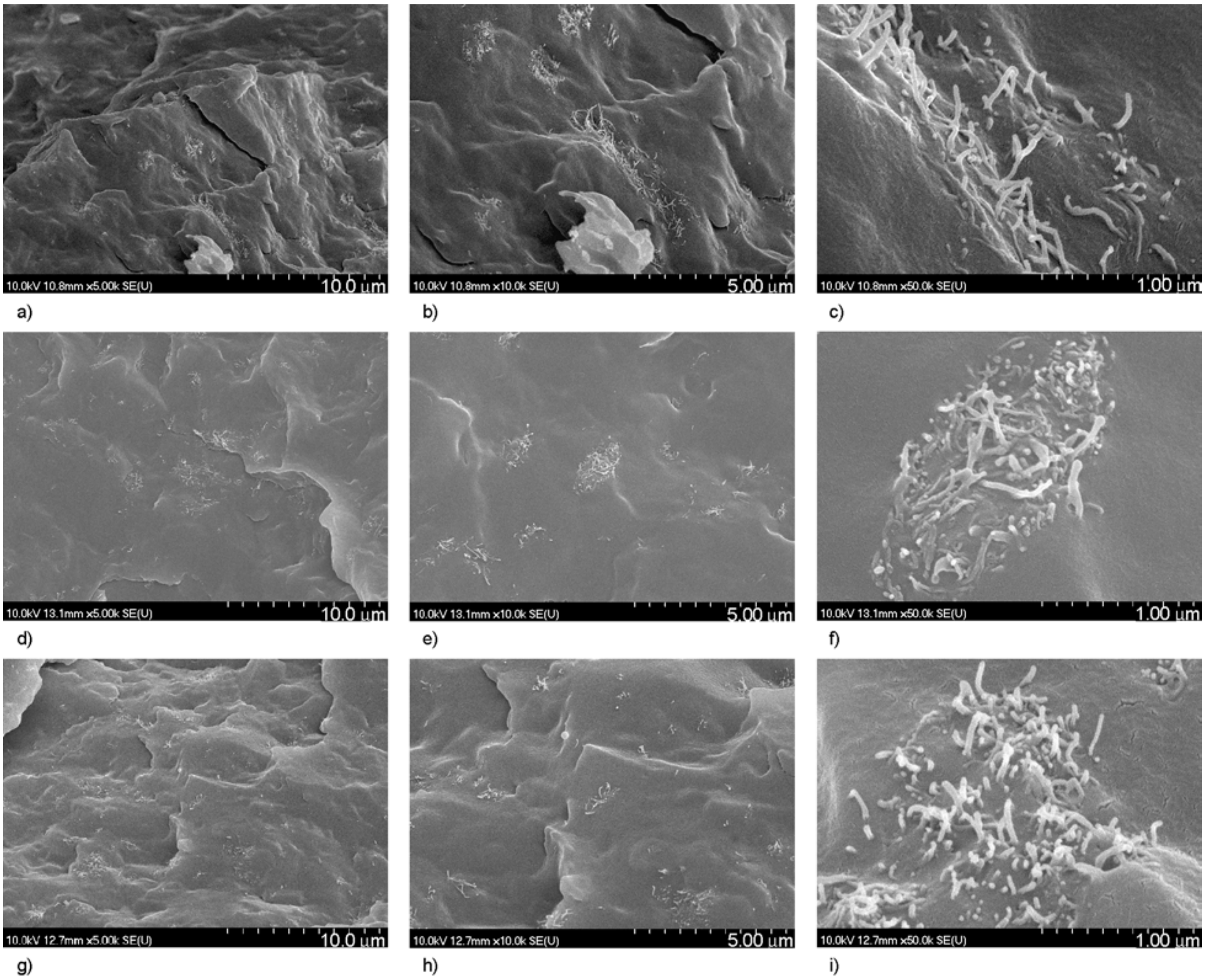

Figure 9. SEM image of samples PP/UPNT/2 (a, b, c), OMAEA/MB/2 (d, e, f), OMAEA/IM/2 (g, h, i)

case of PP/CNT composites produced by masterbatch preparation method, tendency of the CNTs to agglomerate seemed to be lower as lumps were smaller, and more homogeneous dispersion of CNTs in the polymer could be achieved (Figure 9d–9f). Slightly better dispersion could be obtained by application of surface-treated CNTs as significantly smaller aggregates could be observed on the surface of the composite (Figure 9g–9i).

4. Conclusions

New types of coupling agents were synthesized and applied for enhancing the interaction between talc supported multi-walled carbon nanotubes and PP. In this first presentation of the research basic electrical, thermal and rheological properties of the PP/CNT composites were investigated. The following conclusions were drawn on the basis of the measured data:

- Electrically, the UPNT (talc supported MWCNT produced at University of Pannonia) and the NC (industrial grade commercial MWCNT produced by Nanocyl) carbon nanotubes exhibited very similar behaviour as polypropylene fillers. Carbon nanotubes can lower the electrical resistivity of polypropylene considerably. The electrical conductivity percolation threshold in the polymer matrix is approx. 2 wt% for both nanotube types.
- Introducing the coupling agent into the composite by the impregnation method is advantageous from the electrical resistivity point of view, but the way of blending the additives with the CNT and the polymer was not a successful method for improving the properties.
- The properties of OMAEA-compatibilized PP/MWCNT composites are either superior (e.g. electrical conductivity) to those prepared by OMA coupling or are at least at the same level (e.g. thermal conductivity increase). Therefore, OMAEA appears to be a better overall coupling agent choice for polypropylene and talc-supported MWCNTs.
- The thermal conductivity of polypropylene can be improved by adding carbon nanotubes into the matrix. UPNT nanotubes outperformed commercial NC nanotubes by 17% in this respect. Unlike in the case of electrical conductivity, thermal conductivity does not saturate at approx. 2 wt% CNT concentration but rather, it keeps increasing as a quasi linear function of the nanotube contents of the sample. Neither the introduction method nor the chemical structure of the compatibilizer affects the thermal conductivity of the PP/coupling agent/MWCNT composites significantly.
- The tendency to agglomeration of CNTs decreased due to surface treatment according to SEM graphs of the composites, which could probably be related to the coupling agent interacting in the smaller diameter of pores on the CNT surface.

Acknowledgements

We acknowledge the financial support of this work by the Hungarian State and the European Union under the TAMOP-4.2.1/B-09/1/KONV-2010-0003 project.

References

[1] Coleman J. N., Khan U., Blau W. J., Gun'ko Y. K.: Small but strong: A review of the mechanical properties of carbon nanotube–polymer composites. Carbon, **44**, 1624–1652 (2006).
DOI: 10.1016/j.carbon.2006.02.038

[2] Krause B., Pötschke P., Häußler L.: Influence of small scale melt mixing conditions on electrical resistivity of carbon nanotube-polyamide composites. Composites Science and Technology, **69**, 1505–1515 (2009).
DOI: 10.1016/j.compscitech.2008.07.007

[3] Bao H-D., Guo Z-X., Yu J.: Effect of electrically inert particulate filler on electrical resistivity of polymer/multi-walled carbon nanotube composites. Polymer, **49**, 3826–3831 (2008).
DOI: 10.1016/j.polymer.2008.06.024

[4] Spitalsky Z., Tasis D., Papagelis K., Galiotis C.: Carbon nanotube–polymer composites: Chemistry, processing, mechanical and electrical properties. Progress in Polymer Science, **35**, 357–401 (2009).
DOI: 10.1016/j.progpolymsci.2009.09.003

[5] Ounaies Z., Park C., Wise K. E., Siochi E. J., Harrison J. S.: Electrical properties of single wall carbon nanotube reinforced polyimide composites. Composites Science and Technology, **63**, 1637–1646 (2003).
DOI: 10.1016/S0266-3538(03)00067-8

[6] Li C., Thostenson E. T., Chou T-W.: Sensors and actuators based on carbon nanotubes and their composites: A review. Composites Science and Technology, **68**, 1227–1249 (2008).
DOI: 10.1016/j.compscitech.2008.01.006

[7] Breuer O., Sundararaj U.: Big returns from small fibers: A review of polymer/carbon nanotube composites. Polymer Composites, **25**, 630–645 (2004).
DOI: 10.1002/pc.20058

[8] Moniruzzaman M., Winey K. I.: Polymer nanocomposites containing carbon nanotubes. Macromolecules, **39**, 5194–5205 (2006).
DOI: 10.1021/ma060733p

[9] Wang C., Guo Z-X., Fu S., Wu W., Zhu D.: Polymers containing fullerene or carbon nanotube structures. Progress in Polymer Science, **29**, 1079–1141 (2004).
DOI: 10.1016/j.progpolymsci.2004.08.001

[10] Liu P.: Modifications of carbon nanotubes with polymers. European Polymer Journal, **41**, 2693–2703 (2005).
DOI: 10.1016/j.eurpolymj.2005.05.017

[11] Homenick C. M., Lawson G., Adronov A.: Polymer grafting of carbon nanotubes using living free–radical polymerization. Polymer Reviews, **47**, 265–290 (2007).
DOI: 10.1080/15583720701271237

[12] Dutra R. C. L., Soares B. G., Campos E. A., Silva J. L. G.: Hybrid composites based on polypropylene and carbon fiber and epoxy matrix. Polymer, **41**, 3841–3849 (2000).
DOI: 10.1016/S0032-3861(99)00552-2

[13] Wonderly C., Grenestedt J., Fernlund G., Cěpus E.: Comparison of mechanical properties of glass fiber/vinyl ester and carbon fiber/vinyl ester composites. Composites Part B: Engineering, **36**, 417–426 (2005).
DOI: 10.1016/j.compositesb.2005.01.004

[14] Yang Y., Lu C-X., Su X-L., Wu G-P., Wang X-K.: Effect of nano-SiO_2 modified emulsion sizing on the interfacial adhesion of carbon fibers reinforced composites. Materials Letters, **61**, 3601–3604 (2007).
DOI: 10.1016/j.matlet.2006.11.121

[15] Xie X. L., Aloys K., Zhou X. P., Zeng F. D.: Ultrahigh molecular mass polyethylene/carbon nanotube composites crystallization and melting properties. Journal of Thermal Analysis and Calorimetry, **74**, 317–323 (2003).
DOI: 10.1023/A:1026362727368

[16] Zhou X. P., Xie X. L., Zeng F., Li R. K. Y., Mai Y. W.: Properties of polypropylene/carbon nanotube composites compatibilized by maleic anhydride grafted SEBS. Key Engineering Materials, **312**, 223–228 (2006).
DOI: 10.4028/www.scientific.net/KEM.312.223

[17] Varga Cs., Miskolczi N., Szakács H., Lipóczi G.: Effects of industrial scale production on the chemical composition of novel coupling agents and its relationship to the mechanical properties of chopped glass fibre mat reinforced thermoset composites. Materials and Design, **32**, 12–20 (2011).
DOI: 10.1016/j.matdes.2010.06.046

[18] Varga Cs., Miskolczi N., Bartha L., Lipóczi G., Falussy L.: Improving the compatibility of man-made fibre reinforced composites. Hungarian Journal of Industrial Chemistry, **36**, 137–142 (2008).

[19] Varga Cs., Miskolczi N., Bartha L., Lipóczi G.: Improving the mechanical properties of glass-fibre-reinforced polyester composites by modification of fibre surface. Materials and Design, **31**, 185–193 (2010).
DOI: 10.1016/j.matdes.2009.06.034

[20] Szentes A., Horváth G.: Role of catalyst support int he growth of multi-walled carbon nanotubes. Hungarian Journal of Industrial Chemistry, **36**, 113–117 (2008).

[21] Boudenne A., Ibos L., Gehin E., Candau Y.: A simultaneous characterization of thermal conductivity and diffusivity of polymer materials by a periodic method. Journal of Physics D: Applied Physics, **37**, 132–139 (2004).
DOI: 10.1088/0022-3727/37/1/022

[22] Brunauer S., Emmett P. H., Teller E.: Adsorption of gases in multimolecular layers. Journal of the American Chemical Society, **60**, 309–319 (1938).
DOI: 10.1021/ja01269a023

[23] Barrett P., Joyner L. G., Halenda P. P.: The determination of pore volume and area distributions in porous substances. I. Computations from nitrogen isotherms. Journal of the American Chemical Society, **73**, 373–380 (1951).
DOI: 10.1021/ja01145a126

[24] Lee S. H., Cho E. N. R., Jeon S. H., Youn J. R.: Rheological and electrical properties of polypropylene composites containing functionalized multi-walled carbon nanotubes and compatibilizers. Carbon, **45**, 2810–2822 (2007).
DOI: 10.1016/j.carbon.2007.08.042

[25] Jin S. H., Park Y-B., Yoon K. H.: Rheological and mechanical properties of surface modified multi-walled carbon nanotube-filled PET composite. Composites Science and Technology, **67**, 3434–3441 (2007).
DOI: 10.1016/j.compscitech.2007.03.013

[26] Xiao K. Q., Zhang L. C., Zarudi I.: Mechanical and rheological properties of carbon nanotube-reinforced polyethylene composites. Composites Science and Technology, **67**, 177–182 (2007).
DOI: 10.1016/j.compscitech.2006.07.027

[27] Pötschke P., Fornes T. D., Paul D. R.: Rheological behavior of multiwalled carbon nanotube/polycarbonate composites. Polymer, **43**, 3247–3255 (2002).
DOI: 10.1016/S0032-3861(02)00151-9

[28] Prashantha K., Soulestin J., Lacrampe M. F., Krawczak P., Dupin G., Claes M.: Masterbatch-based multi-walled carbon nanotube filled polypropylene nanocomposites: Assessment of rheological and mechanical properties. Composites Science and Technology, **69**, 1756–1763 (2009).
DOI: 10.1016/j.compscitech.2008.10.005

eXPRESS Polymer Letters Vol.6, No.6 (2012) 503–510
Available online at www.expresspolymlett.com
DOI: 10.3144/expresspolymlett.2012.53

Effects of SEBS-g-MAH on the properties of injection moulded poly(lactic acid)/nano-calcium carbonate composites

W. S. Chow[1,2,3*], *Y. Y. Leu*[1], *Z. A. Mohd Ishak*[1,2]

[1]School of Materials and Mineral Resources Engineering, Engineering Campus, Universiti Sains Malaysia, Nibong Tebal 14300 Penang, Malaysia
[2]Cluster for Polymer Composites, Engineering and Technology Research Platform, Engineering Campus, Universiti Sains Malaysia, 14300 Nibong Tebal, Pulau Pinang, Malaysia
[3]Institut für Verbundwerkstoffe GmbH (Institute for Composite Materials), Kaiserslautern University of Technology, D-67663 Kaiserslautern, Germany

Received 8 November 2011; accepted in revised form 15 January 2012

Abstract. Poly(lactic acid)/nano-precipitated calcium carbonate (PLA/NPCC) composites toughened with maleated styrene-ethylene/butylene-styrene (SEBS-g-MAH) were prepared by melt-compounding on a co-rotating twin-screw extruder followed by injection moulding. The mechanical properties of the PLA nanocomposites were characterized by tensile, flexural and impact tests, while their morphology were investigated using transmission electron microscopy (TEM). The thermal properties of the composites were examined with differential scanning calorimeter (DSC) and thermogravimetric analyzer (TGA). The elongation at break and impact strength of the PLA/NPCC nanocomposites increased significantly after addition of SEBS-g-MAH. Both nano-dispersed NPCC and small NPCC clusters were found in PLA matrix. Also, some SEBS-g-MAH encapsulated NPCC can be observed. Thermal stability of PLA/NPCC was enhanced prominently by the addition of SEBS-g-MAH.

Keywords: *nanocomposites, poly(lactic acid), nano-precipitated calcium carbonate, thermal properties, mechanical properties*

1. Introduction

Organic/inorganic hybrid nanocomposites have received significant attentions from both academic and industrial sectors due to the excellent enhancement in certain physical and chemical properties compared to the pure material. The addition of nanofillers such as nanoclays, nano-calcium carbonate and nano-silica improve the mechanical performance of polymers significantly [1–3]. The addition of inorganic fillers has been proved to be an effective approach for the enhancement of the mechanical properties (e.g. stiffness and toughness). Nano- and micro-sized calcium carbonate ($CaCO_3$) particles have been used to improve the impact toughness of several thermoplastics, e.g. polypropylene, polyethylene and aliphatic polyketone [4–7].

Poly(lactic acid) (PLA) derived from renewable resources has become popular owing to their sustainability, biodegradability and superior transparency [8]. In recent reports, PLA-based nanocomposites, prepared by the addition of nanofillers such as nanoclay, nano-calcium carbonate, titanium oxide nanoparticles, cellulose nanofiber and carbon nanotube, exhibited remarkable improvement in mechanical and thermal properties, dimensional stability, barrier and physicochemical behaviours [9–13].

Though the hybridization of polymer and nanoparticle can be a potential class of materials, there are

---

[*]Corresponding author, e-mail: shyang@eng.usm.my

few issues always need to be considered, e.g. compatibility between polymer and nanoparticles, dispersion and distribution of nanoparticles, brittleness and toughness of the polymer nanocomposites, as well as their processability. Therefore, chemical and physical modifications are often applied to achieve these objectives. Maleic anhydride grafted styrene-ethylene/butylene-styrene copolymers (SEBS-g-MAH) has been used as polymeric compatibilizer, interfacial modifier and toughening agent. In our previous work, the impact strength, elongation at break and thermal stability of PLA/organo-montmorillonite nanocomposites was enhanced significantly by the addition of SEBS-g-MAH [14]. SEBS-g-MAH improved the dispersion of nano-magnesium hydroxide (MH) and interfacial adhesion in polypropylene/MH nanocomposites [15]. The impact strength and ductility of polyamide 6/polypropylene/organoclay nanocomposites was improved significantly by the addition of SEBS-g-MAH [16]. Super-tough polyamide 6/organo-montmorillonite nanocomposite was obtained with 30 wt% of maleinated styrene-ethylene/butylene-styrene copolymers [17]. It has also been documented that the essential work of fracture for high density polyethylene/organo-montmorillonite and polypropylene/organo-montmorillonite were improved in the presence of SEBS [18]. The goal of present work is to improve the thermal and mechanical properties (especially elongation at break and impact strength) of PLA/NPCC nanocomposites by incorporation of SEBS-g-MAH. For this purpose, PLA/NPCC nanocomposites with and without SEBS-g-MAH were produced using melt mixing followed by injection moulding. Accordingly, the mechanical and thermal properties of the PLA nanocomposites were determined and discussed.

2. Experimental

2.1. Materials

PLA (Ingeo™ 3051D) was purchased from NatureWorks LLC® (Minnetonka, USA). The specific gravity and melt flow index of the PLA are 1.25 and 25 g/10 min (2.16 kg load, 210°C). The stearic acid treated NPCC (Zancarb CC-R; particle size: 40–80 nm; specific gravity: 2.50) was supplied by Zantat Sdn. Bhd (Kuala Lumpur, Malaysia). SEBS-g-MAH with a MAH grafting level of 1.4–2.0 wt% and styrene/rubber ratio of 30/70 (wt/wt) was purchased from Shanghai Jianqiao Plastic Co. Ltd., (Shanghai, China). The melt flow index and specific gravity of the SEBS-g-MAH are 1.0 g/10 min (2.16 kg load, 230°C) and 0.91, respectively. The designation and composition for PLA/NPCC nanocomposites are shown in Table 1.

Table 1. Materials designation and composition for PLA/NPCC composites

Materials designation	Composition		
	PLA [wt%]	NPCC [wt%]	SEBS-g-MAH [phr]
PLA	100	–	–
PLA/NPCC	98	2	–
PLA/NPCC/S5	98	2	5
PLA/NPCC/S10	98	2	10
PLA/NPCC/S15	98	2	15
PLA/NPCC/S20	98	2	20

2.2. Preparation of PLA/NPCC nanocomposites

Prior to extrusion, all the materials were dried at 80°C for 15 h in vacuum oven (Memmert GmbH, Schwabach, Germany). PLA nanocomposites were melt-compounded using a PSM30 co-rotating twin-screw extruder (Sino-Alloy Machinery, Taoyuan County, Taiwan) with temperature zone set up in the range of 160–190°C. The screw speed was set at 150 rpm. PLA nanocomposite specimens [tensile (ASTM D638 type I), flexural (ASTM D790) and impact (ASTM D4812)], were moulded using an injection moulding machine (HTF86X1, Haitian Plastics Machinery, Ningbo, China). The barrel temperatures were set in the range of 165–190°C, from the feeding section to the nozzle.

2.3. Transmission electron microscopy (TEM)

TEM specimens of PLA nanocomposites were prepared using a PT-PC PowerTome ultramicrotome (Boeckeler Instruments, Arizona, USA). Ultra-thin sections of about 50 nm in thickness of the PLA specimen was cut with a diatome diamond knife (45°) at room temperature. The specimen was stained with osmium tetroxide for an hour prior TEM measurements. TEM measurements were conducted using a Zeiss Libra 120 Plus energy filtering transmission electron microscope (Carl Zeiss, Jena, Germany) operating at an accelerating voltage of 120 kV.

2.4. Thermal characterization (TGA and DSC)

Thermal decomposition temperature of the PLA nanocomposites was characterized using a Pyris 6 thermogravimetric analyzer (Perkin Elmer, Massachusetts, USA). The specimens were heated from room temperature to 600°C at a heating rate of 10°C/min in nitrogen atmosphere. Differential scanning calorimeter DSC 6 (Perkin Elmer, Massachusetts, USA) was used to evaluate the thermal behaviour of the PLA/NPCC nanocomposite. The specimens were scanned from 30 to 190°C at a heating rate of 10°C/min. Then, they were cooled from 190 to 30°C at a cooling rate of 10°C/min. Second scanning was performed similar to the first scanning in order to erase the thermal history. The glass transition temperature (T_g), melting temperature (T_m), and crystallization temperature (T_c) were determined. The degree of crystallinity (χ_c) of PLA nanocomposites was calculated according to Equation (1):

$$\chi_c = \frac{\Delta H_m}{\Delta H_f \cdot w_{PLA}} \cdot 100\% \qquad (1)$$

where χ_c is the degree of crystallinity; ΔH_m is the heat of fusion of the sample; ΔH_f corresponds to the heat of fusion for 100% crystalline material, and w_{PLA} is the net weight fraction of the PLA. The heat of fusion of 100% crystalline PLA (ΔH_f) is approximately 93.6 J/g [19].

2.5. Mechanical testing

Tensile and flexural tests were performed using an Instron 3366 (Instron, Massachusetts, USA) according to ASTM D638 and ASTM D790, respectively. Tensile tests were conducted at a crosshead speed of 5 mm/min. Flexural tests were performed using three-point bending configuration at crosshead speed of 1.5 mm/min and support span length of 50 mm. Charpy impact test was carried out on both notched and un-notched specimens using a Zwick analogue Charpy Pendulum Impact Tester (Zwick Roell, Ulm, Germany) with a pendulum of 7.5 J.

3. Results and discussion

3.1. Transmission electron microscopy (TEM)

Figure 1a–1f shows the TEM images of the PLA/NPCC composites (with and without SEBS-g-MAH) taken at low and high magnification. It can be seen that the NPCC nanoparticles are in cubic shape with dimension of 40–80 nm. Nano-dispersed NPCC and small clusters of NPCC can be observed in the PLA matrix (c.f. Figure 1a–1b). In Figure 1c and 1e, the dark grey region (i.e. region that stained by osmium tetroxide) with dimension of approximately 1–2 µm can be ascribed to the SEBS-g-MAH. Interesting to note that some of the NPCC are encapsulated by SEBS-g-MAH (c.f. Figure 1d and 1f), which can be associated to the affinity between NPCC and SEBS-g-MAH. Also, one may find that more NPCC were encapsulated by SEBS-g-MAH for the PLA/NPCC composites which contain higher loading of SEBS-g-MAH (i.e. PLA/NPCC/S20).

3.2. Thermogravimetric analysis (TGA)

TGA curves for NPCC, SEBS-g-MAH, PLA and PLA/NPCC/SEBS-g-MAH composites are displayed in Figure 2. The decomposition temperatures, T_{95}, T_{50} and T_5 are summarized in Table 2. T_{95}, T_{50} and T_5 are corresponding to the temperature at which the remaining mass of the materials is 95, 50 and 5% respectively. The decomposition temperature in the range of 335–362°C is related to the thermal dissociation of the PLA. From the TGA curves, it can be seen that the decomposition temperature of NPCC starts at 250°C and the char residue is approximately 96.9% at the temperature

Table 2. TGA data of PLA and PLA/NPCC composites

Materials designation	Decomposition temperature [°C]		T_{95} [°C]	T_{50} [°C]	T_5 [°C]	Char residue [%]
	T_{d1}	T_{d2}				
PLA	353.4	–	346.0	370.0	390.8	0
PLA/NPCC	334.6	–	327.2	352.4	376.9	2.8
PLA/NPCC/S5	354.7	446.0	337.1	368.7	464.8	2.7
PLA/NPCC/S10	359.1	451.0	342.8	372.7	483.8	2.8
PLA/NPCC/S15	360.8	451.7	343.7	374.7	486.9	2.2
PLA/NPCC/S20	361.9	451.6	345.3	375.2	493.7	2.3
NPCC	250.0	–	–	–	–	96.9
SEBS-g-MAH	444.0	–	424.8	469.9	498.9	0

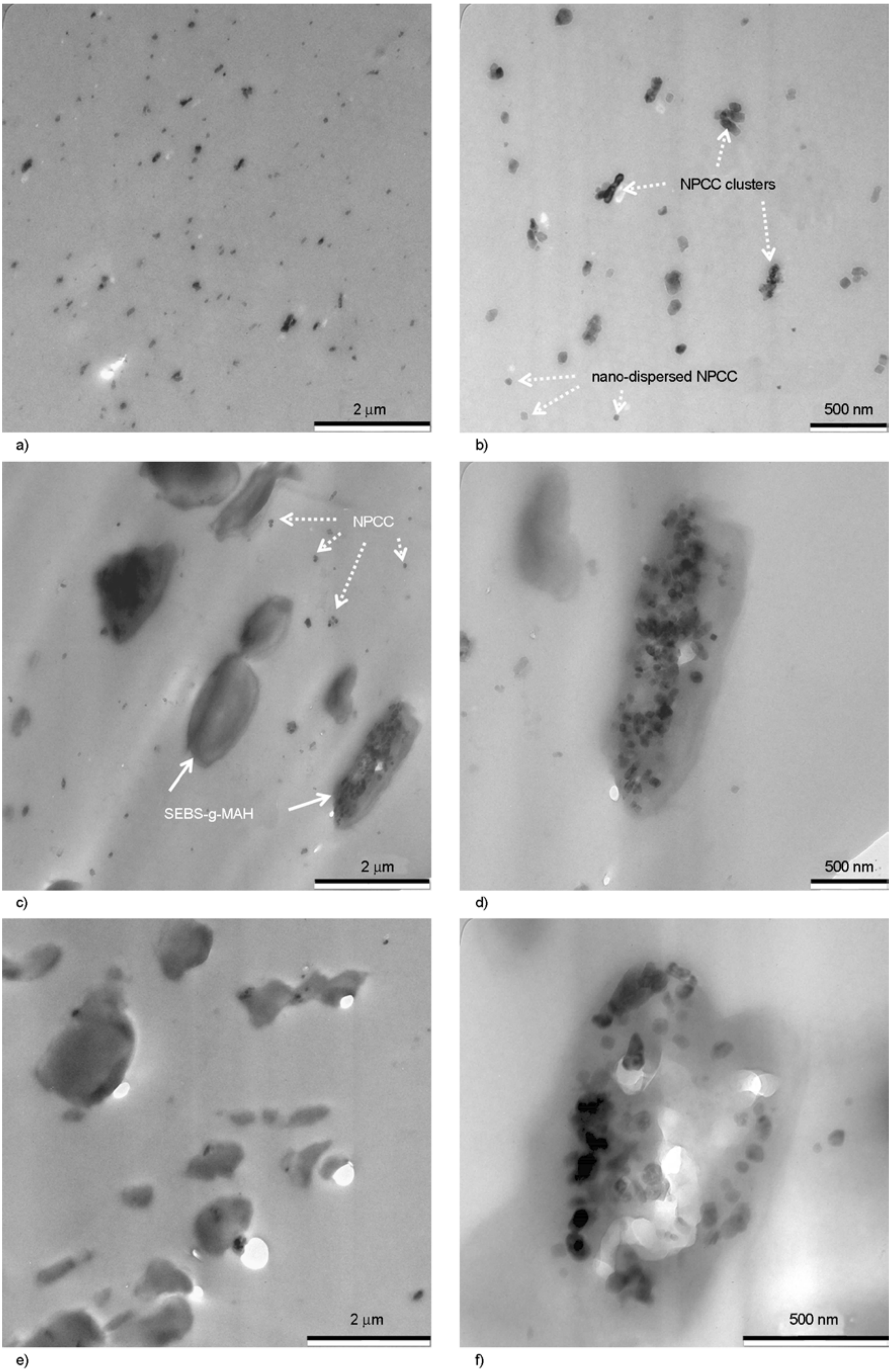

Figure 1. a) TEM image of PLA/NPCC composites taken at low magnification, b) TEM image of PLA/NPCC composites taken at high magnification, c) TEM image of PLA/NPCC/S5 composites taken at low magnification, d) TEM image of PLA/NPCC/S5 composites taken at high magnification, e) TEM image of PLA/NPCC/S20 composites taken at low magnification, f) TEM image of PLA/NPCC/S20 composites taken at high magnification.

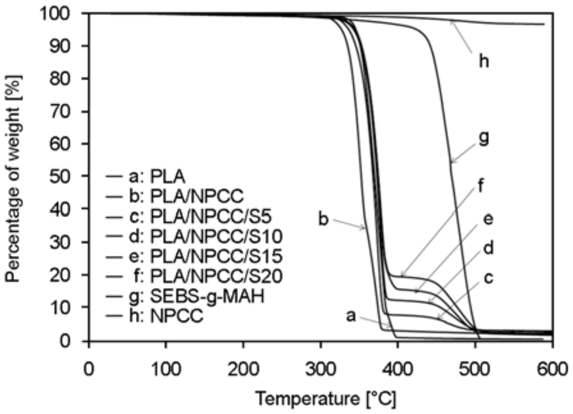

Figure 2. TGA curves of PLA, NPCC, SEBS-g-MAH and PLA/NPCC composites

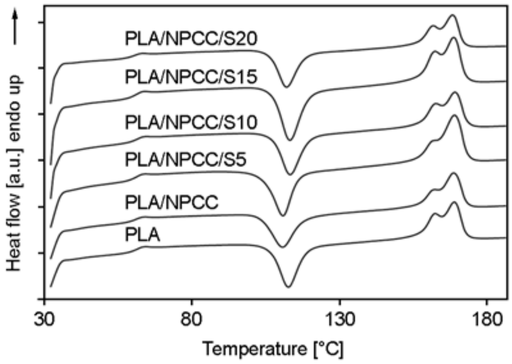

Figure 3. DSC thermograms of PLA and PLA/NPCC composites

of 600°C. The mass loss of NPCC is attributed to the decomposition of stearic acid (i.e. surface modifier). It is also found that the decomposition of organic modifier may accelerate thermal decomposition for the PLA/NPCC composites. According to Kim and Michler [20], the basic nature of calcium carbonate may catalyze the depolymerisation of the ester bonds of PLA which led to a decrease in thermal stability of the respective composite. It can be seen that the decomposition temperatures, T_{95}, T_{50} and T_5 values of PLA/NPCC nanocomposites improved significantly by the addition of SEBS-g-MAH. Note that the highest mass loss of SEBS-g-MAH occurred at temperature of approximately 444°C. Also, the thermal stability of PLA/NPCC nanocomposites increased marginally with the increasing loading of SEBS-g-MAH. Similar finding was also observed in our previous works on PLA/OMMT [14] and PA6/PP/organoclay nanocomposites [16].

3.3. Differential scanning calorimetry (DSC)

Figure 3 shows the DSC thermograms of PLA and PLA/NPCC nanocomposites. The thermal characteristics (e.g. T_g, T_c, T_m) of the PLA and its nanocomposites are summarized in Table 3. In Figure 3, PLA shows a melting temperature peak (T_{m1}) at 168.8°C with a shoulder peak (T_{m2}) at 161.2°C. Bimodal melting peaks are observed in all PLA/NPCC composites with and without SEBS-g-MAH. Multiple melting behaviour of PLA is depends on crystallization conditions (thermal prehistory) and T_c value [21]. Double melting endotherms are commonly found in PLA which crystallized at T_c in the temperature range of 110–130°C [22]. The multiple melting endotherms can be attributed to the melt-recrystallization mechanism [23]. From Table 3, it can be seen that, the presence of NPCC does not changes the T_g, T_c, T_{m1} and T_{m2} values of PLA significantly, this may related to the weak interaction between the polymer and the mineral filler [24]. However, PLA/NPCC nanocomposite exhibits higher degree of crystallinity than that of neat PLA. Such behaviour is reasonable due to the fact that NPCC can act as nucleating agent. Similar finding was reported by Suksut and Deeprasertkul [25], who found that the degree of crystallinity of PLA was increased prominently in the presence of $CaCO_3$. On the contrary, the incorporation of SEBS-g-MAH reduces the degree of crystallinity of PLA/NPCC nanocomposites. This is attributed to the encapsulation of NPCC by SEBS-g-MAH (evidenced by TEM, as discussed previously), which may retard the efficiency of NPCC as nucleating agent in the crystallization of PLA. This is in line with the finding from Tjong *et al.* [1], who reported that SEBS-

Table 3. Thermal characteristics of PLA and PLA/NPCC composites recorded from DSC

Materials designation	Thermal characteristics						
	T_g [°C]	T_c [°C]	T_{m1} [°C]	T_{m2} [°C]	ΔH_c [J/g]	ΔH_m [J/g]	χ_c [%]
PLA	60.9	112.7	168.8	161.2	27.3	31.2	33.3
PLA/NPCC	60.6	110.8	168.6	160.1	33.3	34.9	38.0
PLA/NPCC/S5	60.8	110.8	169.0	160.2	24.8	32.2	36.8
PLA/NPCC/S10	61.3	113.3	169.1	163.2	24.7	28.0	33.5
PLA/NPCC/S15	60.6	113.2	168.7	162.0	27.5	29.1	36.4
PLA/NPCC/S20	59.7	112,5	168.2	161.0	21.3	24.9	32.5

g-MAH reduced the degree of crystallinity of polypropylene/montmorillonite nanocomposites.

3.4. Mechanical properties

The tensile stress-strain curves of neat PLA and PLA/NPCC composites are shown in Figure 4. PLA fractured in brittle mode with 8.4% elongation at break. It can be seen that PLA/NPCC nanocomposite achieved 12.4% of elongation at break, which suggesting an improvement in ductility of the material. Furthermore, PLA/NPCC/SEBS-g-MAH composites experienced significant cold drawing and yielding implying that further enhancement in ductility of the nanocomposites. Mechanical properties of PLA and PLA/NPCC nanocomposites are summarized in Table 4. It can be seen that the NPCC does not have significant effect on the tensile and flexural modulus of PLA. This is due to the non-reinforcing behaviour of this NPCC. However, the elongation at break of PLA increased of about 48% by the addition of NPCC, implying an improvement in toughness of PLA. This is due to the fact that NPCC can act as stress concentrator and induce microvoids by debonding at the NPCC-PLA interface during the tensile deformation. The cavitational process promotes shear-banding mechanism in the plane-stress region and triggers matrix shearing in PLA during fracture. Accordingly, the shear yielding mechanism becomes operative and the PLA composites are able to absorb large quantities of energy when subjected to fracture deformation. This is in line with the micro-mechanistic model for toughening using filler particles as proposed by Kim and Michler [20]. According to Weon *et al.* [26], toughenability of PP has been positively altered by the incorporation of calcium carbonate, which is also related to the massive crazing and shear banding of the PP matrix in the presence of the filler. From Table 4, it can be seen that the modulus and strength of PLA/NPCC composites reduced marginally with the increasing content of SEBS-g-MAH. This is attributed to the lower modulus and elastomeric nature of SEBS-g-MAH [1, 17, 27]. Note that the elongation at break of PLA/NPCC composites increased drastically with increasing loading of SEBS-g-MAH. SEBS-g-MAH acts as stress concentrators upon the application of tensile stress and formed micro-voids that able to trigger micro-deformation mechanisms. This will lead to an increase of ductility and toughness in the nanocomposites.

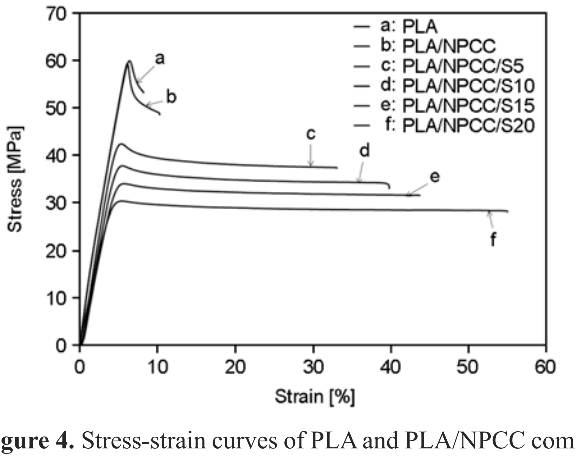

Figure 4. Stress-strain curves of PLA and PLA/NPCC composites

The Charpy impact strength for notched and un-notched specimens of neat PLA and PLA/NPCC nanocomposites are summarized in Table 4. The impact strength for both notched and un-notched PLA/NPCC nanocomposite increased significantly by the incorporation of SEBS-g-MAH. The impact strength of PLA/NPCC nanocomposite increased 268 and 138% for un-notched and notched specimens, respectively with the addition of 20 phr of SEBS-g-MAH. According to Collyer [28], the toughening mechanism of rubber particles dispersed within a glassy polymer includes energy absorption

Table 4. Mechanical properties of PLA and PLA/NPCC composites

Mechanical properties	Materials designation					
	PLA	PLA/NPCC	PLA/NPCC/S5	PLA/NPCC/S10	PLA/NPCC/S15	PLA/NPCC/S20
Tensile modulus [GPa]	1.2±0.02	1.2±0.03	1.1±0.03	1.0±0.01	0.9±0.02	0.9±0.03
Tensile strength [MPa]	59.4±0.4	58.7±1.3	36.9±0.5	33.7±0.5	30.5±1.1	27.7±0.3
Elongation at break [%)]	8.4±0.2	12.4±2.1	32.6 ±1.7	42.9±2.0	44.0±0.3	56.8±1.8
Flexural modulus [GPa]	3.6±0.1	3.8±0.1	3.5±0.1	3.2±0.1	2.8±0.1	2.5±0.1
Flexural strength [MPa]	97.0±0.2	96.1±1.5	81.2±1.2	68.8±0.5	63.3±1.1	55.4±1.3
Impact strength [kJ/m^2] [Un-notched]	22.6±1.5	22.5±1.0	38.6±1.5	51.7±0.55	73.5±2.0	82.9±1.4
Impact strength [kJ/m^2] [Notched]	4.0±0.6	3.2±0.9	6.0±0.7	6.4±0.5	6.6±0.3	7.6±1.1

by rubber particles, debonding at the rubber-matrix interface, matrix crazing, shear yielding or a combination of shear yielding and crazing. Upon the application of impact stress, the rubber particles in the composite acted as stress concentrators and cavitate and/or debond at the rubber-matrix interface, leading to a relief of the triaxial stress state ahead of the notch or crack, thus creating a stress state beneficial for the initiation of multiple matrix shear yielding [29].

4. Conclusions

The PLA/NPCC nanocomposites were successfully produced by using melt compounding technique. Nano-dispersed NPCC (ca. 40 nm) and small NPCC clusters (containing 3–6 NPCC particles) were distributed in PLA matrix. Also, NPCC can act as nucleating agent for PLA. However, NPCC does not enhance the modulus and strength of PLA. It was also found that the thermal stability of PLA/NPCC is lower than that of PLA. SEBS-g-MAH encapsulated NPCC may suppress the nucleating effects of NPCC. The main objectives of this works have been achieved, i.e. (1) significant enhancement of elongation at break and impact strength of PLA/NPCC nanocomposites, and (2) the thermal stability of PLA/NPCC/SEBS-g-MAH is higher than that of PLA/NPCC nanocomposites.

Acknowledgements

Authors would like to thank Universiti Sains Malaysia for the Research University (RU) Grant (814070), Incentive Grant (8021013) and USM Postgraduate Research Grant Scheme (USM-RU-PGRS 8033002) financial support.

References

[1] Tjong S. C., Bao S. P., Liang G. D.: Polypropylene/montmorillonite nanocomposites toughened with SEBS-*g*-MA: Structure–property relationship. Journal of Polymer Science Part B: Polymer Physics, **43**, 3112–3126 (2005).
DOI: 10.1002/polb.20596

[2] Petersson L., Oksman K.: Biopolymer based nanocomposites: Comparing layered silicates and microcrystalline cellulose as nanoreinforcement. Composites Science and Technology, **66**, 2187–2196 (2006).
DOI: 10.1016/j.compscitech.2005.12.010

[3] Ray S. S., Bousmina M.: Biodegradable polymers and their layered silicate nanocomposites: In greening the 21st century materials world. Progress in Materials Science, **50**, 962–1079 (2005).
DOI: 10.1016/j.pmatsci.2005.05.002

[4] Zuiderduin W. C. J., Westzaan C., Huétink J., Gaymans R. J.: Toughening of polypropylene with calcium carbonate particles. Polymer, **44**, 261–275 (2003).
DOI: 10.1016/S0032-3861(02)00769-3

[5] Bartczak Z., Argon A. S., Cohen R. E., Weinberg M.: Toughness mechanism in semi-crystalline polymer blends: II. High-density polyethylene toughened with calcium carbonate filler particles. Polymer, **40**, 2347–2365 (1999).
DOI: 10.1016/S0032-3861(98)00444-3

[6] Zuiderduin W. C. J., Huétink J., Gaymans R. J.: Rigid particle toughening of aliphatic polyketone. Polymer, **47**, 5880–5887 (2006).
DOI: 10.1016/j.polymer.2006.05.077

[7] Lin Y., Chen H., Chan C-M., Wu J.: The toughening mechanism of polypropylene/calcium carbonate nanocomposites. Polymer, **51**, 3277–3284 (2010).
DOI: 10.1016/j.polymer.2010.04.047

[8] Auras A., Lim L-T., Selke S. E. M., Tsuji H.: Poly(lactic acid): Synthesis, structures, properties, processing and applications. Wiley, New Jersey (2010).

[9] Zhou Q., Xanthos M.: Nanoclay and crystallinity effects on the hydrolytic degradation of polylactides. Polymer Degradation and Stability, **93**, 1450–1459 (2008).
DOI: 10.1016/j.polymdegradstab.2008.05.014

[10] Jiang L., Zhang J., Wolcott M. P.: Comparison of polylactide/nano-sized calcium carbonate and polylactide /montmorillonite composites: Reinforcing effects and toughening mechanisms. Polymer, **48**, 7632–7644 (2007).
DOI: 10.1016/j.polymer.2007.11.001

[11] Chen C. C., Gang L. V., Pan C., Song M., Wu C. H., Guo D. D., Wang X. M., Chen B. A., Gu Z. Z.: Poly (lactic acid) (PLA) based nanocomposites – A novel way of drug-releasing. Biomedical Materials, **2**, L1–L4 (2007).
DOI: 10.1088/1748-6041/2/4/L01

[12] Iwatake A., Nogi M., Yano H.: Cellulose nanofiber-reinforced polylactic acid. Composites Science and Technology, **68**, 2103–2106 (2008).
DOI: 10.1016/j.compscitech.2008.03.006

[13] Hapuarachchi T. D., Peijs T.: Multiwalled carbon nanotubes and sepiolite nanoclays as flame retardants for polylactide and its natural fibre reinforced composites. Composites Part A: Applied Science and Manufacturing, **41**, 954–963 (2010).
DOI: 10.1016/j.compositesa.2010.03.004

[14] Leu Y. Y., Mohd Ishak Z. A., Chow W. S.: Mechanical, thermal, and morphological properties of injection molded poly(lactic acid)/SEBS-*g*-MAH/organo-montmorillonite nanocomposites. Journal of Applied Polymer Science, **124**, 1200–1207 (2012).
DOI: 10.1002/app.35084

[15] Liu S-P., Ying J-R., Zhou X-P., Xie X-L., Mai Y-W.: Dispersion, thermal and mechanical properties of polypropylene/magnesium hydroxide nanocomposites compatibilized by SEBS-*g*-MA. Composites Science and Technology, **69**, 1873–1879 (2009).
DOI: 10.1016/j.compscitech.2009.04.004

[16] Kusmono, Mohd Ishak Z. A., Chow W. S., Takeichi T., Rochmadi: Influence of SEBS-g-MA on morphology, mechanical, and thermal properties of PA6/PP/organoclay nanocomposites. European Polymer Journal, **44**, 1023–1039 (2008).
DOI: 10.1016/j.eurpolymj.2008.01.019

[17] González I., Eguiazábal J. I., Nazábal J.: Rubber-toughened polyamide 6/clay nanocomposites. Composites Science and Technology, **66**, 1833–1843 (2006).
DOI: 10.1016/j.compscitech.2005.10.008

[18] Bárány T., Czigány T., Karger-Kocsis J.: Application of the essential work of fracture (EWF) concept for polymers, related blends and composites: A review. Progress in Polymer Science, **35**, 1257–1287 (2010).
DOI: 10.1016/j.progpolymsci.2010.07.001

[19] Wang H., Sun X., Seib P.: Strengthening blends of poly(lactic acid) and starch with methylenediphenyl diisocyanate. Journal of Applied Polymer Science, **82**, 1761–1767 (2001).
DOI: 10.1002/app.2018

[20] Kim G-M., Michler G. H.: Micromechanical deformation processes in toughened and particle-filled semicrystalline polymers: Part 1. Characterization of deformation processes in dependence on phase morphology. Polymer, **39**, 5689–5697 (1998).
DOI: 10.1016/S0032-3861(98)00089-5

[21] Di Lorenzo M. L.: Calorimetric analysis of the multiple melting behavior of poly(L-lactic acid). Journal of Applied Polymer Science, **100**, 3145–3151 (2006).
DOI: 10.1002/app.23136

[22] Pan P., Inoue Y.: Polymorphism and isomorphism in biodegradable polyesters. Progress in Polymer Science, **34**, 605–640 (2009).
DOI: 10.1016/j.progpolymsci.2009.01.003

[23] Sarasua J-R., Rodríguez N. L., Arraiza A. L., Meaurio E.: Stereoselective crystallization and specific interactions in polylactides. Macromolecules, **38**, 8362–8371 (1998).
DOI: 10.1021/ma051266z

[24] Deshmane C., Yuan Q., Misra R. D. K.: On the fracture characteristics of impact tested high density polyethylene–calcium carbonate nanocomposites. Material Science and Engineering: A, **452–453**, 592–601 (2007).
DOI: 10.1016/j.msea.2006.11.059

[25] Suksut B., Deeprasertkul C.: Effect of nucleating agents on physical properties of poly(lactic acid) and its blend with natural rubber. Journal of Polymers and the Environment, **19**, 288–296 (2011).
DOI: 10.1007/s10924-010-0278-9

[26] Weon J-I., Gam K-T., Boo W-J., Sue H-J., Chan C-M.: Impact-toughening mechanisms of calcium carbonate-reinforced polypropylene nanocomposite. Journal of Applied Polymer Science, **99**, 3070–3076 (2006).
DOI: 10.1002/app.22909

[27] Kusmono, Mohd Ishak Z. A., Chow W. S., Takeichi T., Rochmadi: Compatibilizing effect of SEBS-g-MA on the mechanical properties of different types of OMMT filled polyamide 6/polypropylene nanocomposites. Composites Part A: Applied Science and Manufacturing, **39**, 1802–1814 (2008).
DOI: 10.1016/j.compositesa.2008.08.009

[28] Collyer A. A.: Rubber toughened engineering plastics. Chapman and Hall, London (1994).

[29] Loyens W., Groeninckx G.: Deformation mechanisms in rubber toughened semicrystalline polyethylene terephthalate. Polymer, **44**, 4929–4941 (2003).
DOI: 10.1016/S0032-3861(03)00478-6

eXPRESS Polymer Letters Vol.6, No.6 (2012) 511–518
Available online at www.expresspolymlett.com
DOI: 10.3144/expresspolymlett.2012.54

Preparation and characterization of nanocomposites of natural rubber with polystyrene and styrene-methacrylic acid copolymer nanoparticles

*P. Chaiyasat, C. Suksawad, T. Nuruk, A. Chaiyasat**

Department of Chemistry, Faculty of Science and Technology, Rajamangala University of Technology Thanyaburi,
Klong 6, Thanyaburi, 12110 Pathumthani, Thailand

Received 5 November 2011; accepted in revised form 16 January 2012

Abstract. Composites of natural rubber (NR)/vinyl polymer nanoparticles as polystyrene (PS) and poly(styrene-methacrylic acid) (P(S-MAA)) were prepared by heterocoagulation technique. The polymer nanoparticles were prepared by emulsifier-free emulsion polymerizations at 70°C using potassium persulfate as initiator. Under acidic condition where positive charge was present on the NR latex (NRL) surface, the nanoparticles having negative charge mainly from sulfate group of initiator were able to adsorb on the NRL surface, the electrostatic interaction being the driving force. The scanning electron micrographs showed that the polymer nanoparticles are homogenously distributed throughout NR matrix as nano-clusters with an average size of about 500 and 200 nm for PS and P(S-MAA), respectively. The mechanical properties of NR/PS and NR/P(S-MAA) composite films were compared with the NR host. The nanocomposites, particularly when the polymer nanoparticles are uniformly dispersed, possess significantly enhanced mechanical properties strongly depending on the morphology of the nanocomposites.

Keywords: *nanocomposites, heterocoagulation, natural rubber latex*

1. Introduction

Natural rubber (NR, Figure 1a) is one of the most important polymers characterized by excellent elasticity and flexibility, which is widely used in various applications such as medical glove and tubing [1–3]. Because of unsaturated bonds in its macromolecular backbone, it is weak in oil and ozone-resistance due to oxidative or thermal degradation. Thus, short shelf lives and life cycles may be obtained from such NR products. To overcome these drawbacks, some chemical substances was used to treat NR such as tris(nonylated phenyl) phosphate [4] and non-water-soluble amino acids [5]. Moreover, loss of mechanical properties such as low tensile strength and poor tear resistance are also the drawbacks of NR. Many techniques were investigated in order to improve such disadvantages of NR without reducing its wonderful properties. The concept of nano-matrix-dispersed polymer was applied using a small amount of functional polymer polymerized on NR latex (NRL) and then forming matrix. The nano-matrix-dispersed polymer may be prepared by graft copolymerization of natural rubber in latex form. However, side reactions during the graft copolymerization were obtained due to the presence of proteins on the NRL surface [6]. Thus, removal of the protein before graft copolymerization of NR to prepare nano-matrix was carried out [1].

In addition, the conventional reinforcement by adding inorganic materials such as carbon black [7], ultra-fine calcium carbonate [8] and modified montmorillonite [9] were used to strengthen NR. How-

---

*Corresponding author, e-mail: a_chaiyasat@mail.rmutt.ac.th

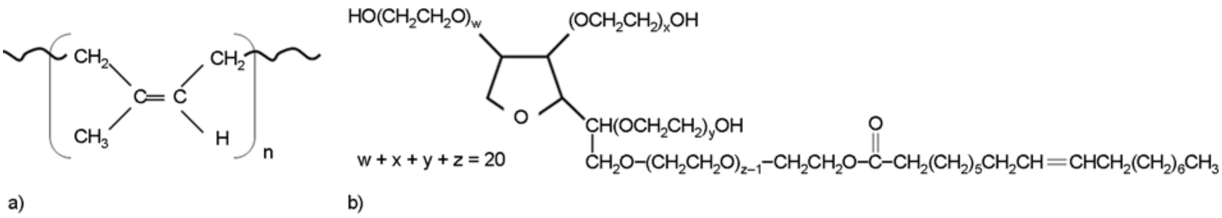

Figure 1. Structure of NR (a) and tween 80 (b)

ever, they have low efficiency to improve NR properties due to the increasing of the compound density or reducing light transmission. Alternative reinforcement such as nano-fillers have recently attracted attention because using only low amount of nanofillers can maintain and control the beneficial properties of NR (flexibility, toughness and etc.) and the fillers (hardness, thermal stability and etc.). Clay minerals are useful to reinforce NR via well-known techniques as melt processing [10, 11], latex-compounding [12] and solution-mixing methods [13]. Moreover, mechanical properties of polymer composite of NR are also improved using nano crab chitin whiskers [14] and surface modified nanocrystalline cellulose [15].

Heterocoagulation is the common interaction of two particles, small and large particles, of a dissimilar nature upon collision. The smaller particles adsorb onto the larger particle surface with various forces such as electrostatic, hydrophobic and secondary molecular interactions as (multiple) hydrogen bonding [16]. This technique is interesting to prepare polymer composite because the polymers are directly blended in emulsion state which would consume less energy and time without grinding. Generally, it is used to prepare polymer composite such as inorganic-inorganic [17], inorganic-organic [3, 18] and organic-organic [19–23] composites. Moreover, to improve NR properties, nanocomposites including NR and inorganic or polymer nanoparticles have been prepared by this technique. The oil resistance of NR film was improved by using small organic particle, polychloroprene (CR), adsorbed onto large NR particle with the heterocoagulation technique [24]. CR would adsorb onto the NR particle surface via hydrogen bonding between carboxylic groups of the protein molecules existing on the NR surface and the polyethylene oxide chains of Tween 80 adsorbed on the CR particles. In addition, the mechanical properties of NR were improved with inorganic particle as SiO_2 nanoparticles [3]. SiO_2 nanoparticles having negative charge on their surfaces were pre-adsorbed with positively charged poly (diallyldimethylammonium chloride) chain before heterocoagulation with NR particle having negative charge of protein existing on the NR surface.

In this work, the simple blending of NRL with polymer nanoparticles using heterocoagulation technique without using any pre-polymer is studied. NRL emulsion is added with a small amount of hard polymer nanoparticles emulsion of polystyrene (PS) or poly(styrene-methacrylic acid) (P(S-MAA)). The nanoparticles having negative charge deriving from initiator adsorbed on NRL surface containing protein-lipid via electrostatic interaction to form composite polymer at the appropriate pH. The mechanical properties of the obtained composite polymer may improve.

2. Experimental

2.1. Materials

Styrene (S) (Aldrich, Wisconsin, USA; purity, 99%) was purified by pass through the column packed with basic Aluminium oxide. Methacrylic acid (MAA) (Merck, Munich, Germany; purity, 99%) was purified by distillation under reduced pressure in a nitrogen atmosphere. The purified monomers were stored in a refrigerator. Potassium persulfate (KPS; Aldrich, Wisconsin, USA) was purified by recrystallization. High ammonia NR latex (ca. 60% dry rubber content; donated from Thai Rubber Latex Co., Ltd., Bangkok, Thailand) was used as received. Analytical grade of sodium hydroxide (NaOH; BDH Prolabo, Leuven, Belgium) and hydrochloric acid (HCl; Ajax Finechem Pty. Ltd., Sydney, Australia) were used as received. Polyoxyethylene (20) sorbitan monooleate (Tween 80; Aldrich, Wisconsin, USA; Figure 1b) was used as received. Deionized water with a specific resistance of $5\cdot10^6$ Ω·cm was distilled before used.

2.2. Polymer nanocomposites preparation

The polymer nanoparticles were prepared by emulsifier-free emulsion polymerization under the conditions listed in Table 1. The polymerizations were carried out at 70°C with a stirring rate of 200 rpm. The monomer (30 and 10 g for P(S-MAA) and PS, respectively) and water (250 and 270 g for P(S-MAA) and PS polymerization, respectively) were charged into the reactors and then purged with N_2 for 30 min. The polymerizations were initiated by the addition (20 g) of KPS aqueous solution (1.2 wt%). The nanocomposites of NR/PS and NR/P(S-MAA) were prepared with heterocoagulation technique (Figure 2) according to the following procedures. The pH of NRL aqueous dispersion (solid content about 10 wt%) containing Tween 80 emulsifier (6 wt% of NR) was adjusted from approximately 11 to 7 with 0.3 M HCl. The polymer nanoparticle aqueous dispersion (10 wt% at pH 7) was gradually dropped to the NR dispersion with gentle mechanical stirring. The polymer composites of NR/PS and NR/P(S-MAA) were obtained when the pH of the mixture solutions were adjusted to 1 by adding 0.3 M HCl. The blending ratio was determined relating to the theoretical number (N_{max}) which is the maximum number of small particles [PS or P(S-MAA)] forming a close-packed monolayer on a large particle (NRL) as given by Equation (1) shown below [25]. To investigate the mechanical properties, NR/PS and NR/P(S-MAA) emulsions were dried in vacuum oven at 40°C to obtain composite films:

$$N_{\mathrm{max}} = \frac{2\pi}{3} \cdot \left[\frac{R_{\mathrm{L}} + R_{\mathrm{S}}}{R_{\mathrm{S}}}\right]^2 \tag{1}$$

where R_L radius of large particle, R_S radius of small particle.

Table 1. Recipes for the preparation of P(S-MAA) and PS particles by emulsifier-free emulsion polymerizations[a]

Ingredient	P(S-MAA)	PS
H_2O [g]	270.00	290.00
KPS [g]	0.24	0.86
S [g]	27.50	10.00
MAA [g]	2.50	–

[a] 200 rpm, 70°C, 24 h, purged by N_2

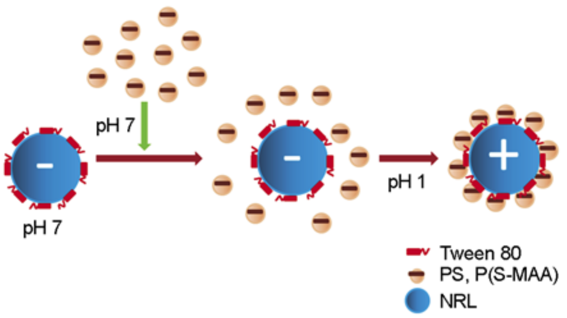

Figure 2. Schematic of the heterocoagulation of NRL and polymer nanoparticles

2.3. Characterizations

Particle diameters and zeta potential were measured by dynamic light scattering (DLS; Zetasizer nano ZS, Malvern, USA) at room temperature. Polymer emulsion samples (approximately 10 wt%) withdrawn from the reactor were directly measured by concentration mode of DLS. PS and P(S-MAA) particles were observed with transmission electron microscope (TEM; JEM-1230, JEOL Ltd., Japan). Each emulsion was diluted to approximately 50 ppm, and then a drop was placed on a carbon-coated copper grid before drying at room temperature in a desiccator. Scanning electron microscope (SEM; JSM-6510, JEOL Ltd., Japan) were used to investigate the morphology of the polymer nanocomposite. For SEM observation, one drop of the polymer dispersion was placed on a nickel SEM stub and dried before Au-coating. Tensile test experiments were conducted on a universal testing machine (Instron, 55R4502, S/N H3342, MA, USA) with a cross head speed of 50 mm/min and the sample length between the jaws is 65 mm, gauge length 25 mm and the thickness 2.0 mm. The measurement was done at room temperature.

3. Results and discussion

3.1. Polymer nanoparticles

PS and P(S-MAA) nanoparticles prepared by emulsifier-free emulsion polymerization were spherical particles as shown in Figure 3. Narrow particle size distribution was obtained for both of them which are characteristic of polymer particles obtained from emulsifier-free emulsion polymerization whereas the presence of emulsifiers results in a broader particle size distribution [26, 27]. In the case of the particle size, PS particles (500 nm) is much larger than P(S-MAA) (200 nm) as shown in Figure 4. Even though both particles are mainly stabilized with electrostatic repulsion of the sulfate ion generated from KPS initiator, in the case of P(S-MAA), carboxyl group in MAA molecule is also able to stabi-

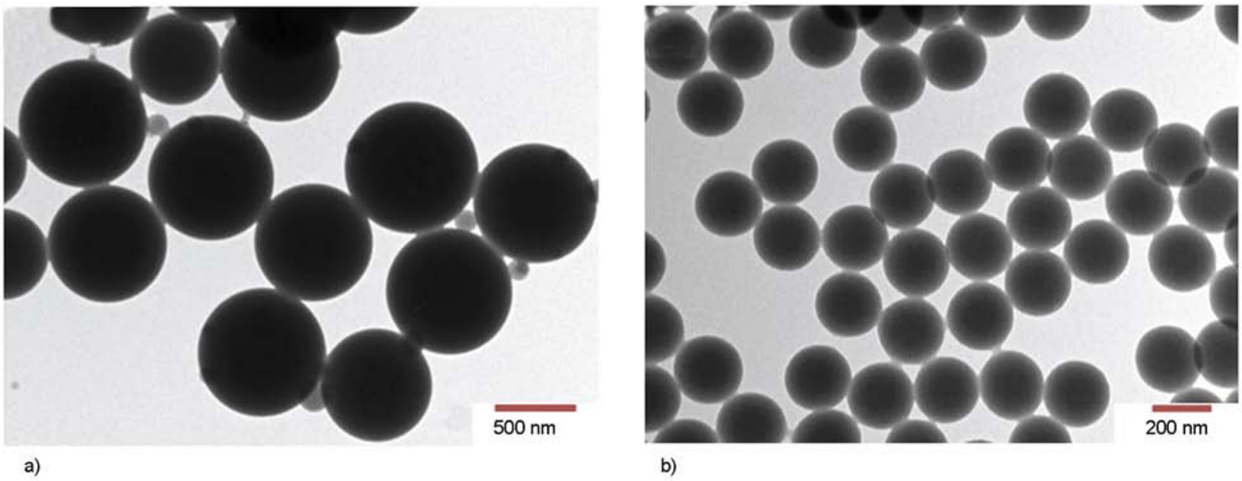

Figure 3. TEM micrographs of polymer nanoparticles prepared by emulsifier-free emulsion polymerizations: (a) PS and (b) P(S-MAA)

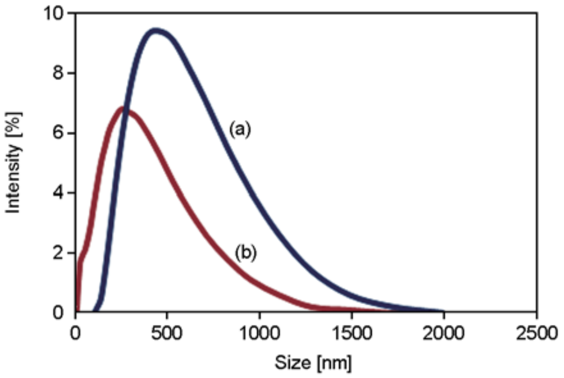

Figure 4. Particle size distribution of polymer nanoparticles prepared by emulsifier-free emulsion polymerizations: (a) PS and (b) P(S-MAA)

lize the particles resulting in the formation of smaller particle than PS.

3.2. Polymer nanocomposites

To prepare composite polymer with heterocoagulation technique where the smaller particle is adsorbed on the larger particle using electrostatic interaction, both particle surfaces should have opposite charges. This technique required the larger particle as core and smaller particle as shell [16]. Although, DLS distribution curve of NRL (Figure 5) giving bimodal peak with the particle size (number-average) of 330 and 1000 nm, NRL was still expected to be the core due to most of NRL weight is the larger size (by weight) while the smaller particles of PS or P(S-MAA) was the shell. Due to the presence of negative charge of smaller particles mainly derived from sulfate ion, NRL surface should contain the positive charge in order to achieve the blending.

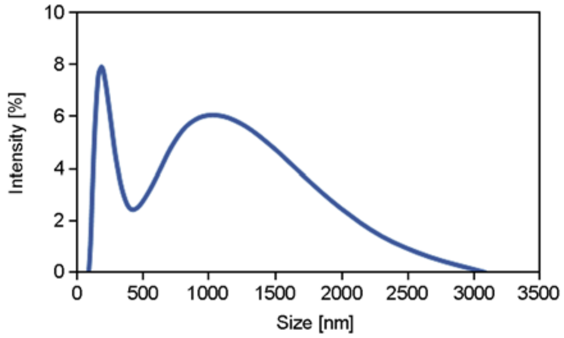

Figure 5. Particle size distribution of NRL

Generally, NRL surface is covered by protein molecules containing acidic and basic side groups described as carboxyl and amino groups, respectively, showing different charged forms depending on its pH. At the appropriate pH where the positive and negative charges on NRL surface are balanced, the net charge is zero, called isoelectric point. The net negative charge will be obtained due to deprotonation of more acidic group when the pH is higher than the isoelectric point. In contrast, if the pH is lower than its isoelectric point, NRL surface gives net positive charge with the protonation of the more basic group. The charge mechanism of protein adsorbed on the NRL surface is shown in Figure 6.

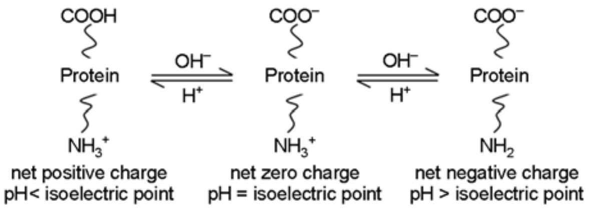

Figure 6. Charge mechanism of protein on the surface of NRL particle

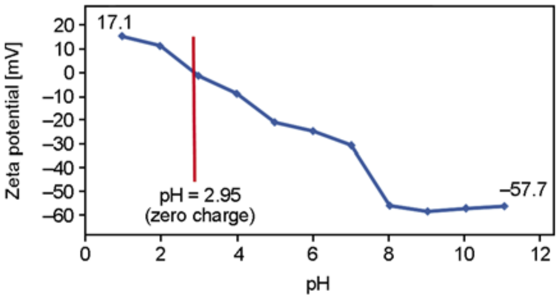

Figure 7. Zeta potential of NRL adsorbed with Tween 80 at various pH

Therefore, NRL surface charge was measured at various pHs in order to obtain the optimum pH giving positive charge. Before charge measurement, nonionic emulsifier (Tween 80) was added to NRL emulsion to maintain the colloidal stability of NRL throughout the experiment especially at the pH giving less charge or neutral. It is well known that Tween 80 contains alcohol, ketone, and ether groups which are able to be protonated under acidic conditions. Therefore, it may increase net positive charge on NRL surface. The zeta potentials of NRL surface at various pH was shown in Figure 7. It is found that the pH at the isoelectric point is 2.95. Therefore, pH of 1 giving the charge of +17.1 mV was selected for the blending condition.

In the case of PS and P(S-MAA) nanoparticles, the negative charge on their surfaces at pH 1 measured with zeta potential technique were –35.6 and –4.3 mV for PS and P(S-MAA), respectively. The difference of the charge between both polymers nanoparticles is due to the utilization of larger amount of KPS for PS than P(S-MAA) preparations. The emulsifier-free emulsion polymerization of less polar monomer as S needed much amount of ionic initiator to stabilize the polymer particles during polymerization. Moreover, carboxyl group which is the weak acid is not able to ionize in high acidic condition (pH 1) resulting in less negative charge of P(S-MAA).

For the blending of NRL and PS or P(S-MAA), large coagulation was formed when they were directly mixed at the optimum pH. This phenomenon is also observed with the blending of poly(styrene-co-butyl acrylate-co-methacrylic acid) and poly(styrene-co-methacryloyloxy ethyltrimethyl ammonium chloride) [20, 21]. To succeed blending, they were mixed at the pH where their surfaces gave the same charge and then change the pH to the optimum condition where both polymers show the opposite charge. Therefore, firstly, PS or P(S-MAA) emulsion at the Nmax calculated by Equation (1) adjusted pH to 7 with 1.0 M NaOH solution was added to NRL emulsion (pH 7) adsorbed with nonionic emulsifier. Secondly, the pH of the mixing emulsion was adjusted from 7 to 1 where NRL and nanoparticle surfaces act positive and negative charges, respectively. The nanoparticle would gradually adsorb on NRL particles during decreasing of the pH. Finally, the composite polymer (NR/PS or NR/P(S-MAA)) where NRL particle is core and nanoparticle [PS or P(S-MAA)] is shell dispersed in aqueous medium were obtained. The composite polymer of NR/PS and NR/P(S-MAA) were successfully prepared by heterocoagulation as the particles sizes distribution of the blending dispersions of NRL and polymer nanoparticles (PS: Figure 8 and P(S-MAA): Figure 9) are larger than those of the host NRL. The prepared NR/PS and NR/P(S-MAA) composite polymers were observed by SEM as shown in Figure 10. The polymer nanoparticles are adsorbed on NRL as nano-cluster (Figure 10c

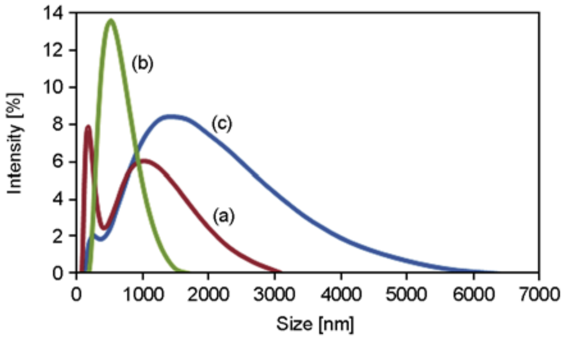

Figure 8. Particle size distributions of NRL (a), PS particle prepared by emulsifier-free emulsion polymerization (b) and NR/PS (c) prepared by heterocoagulation

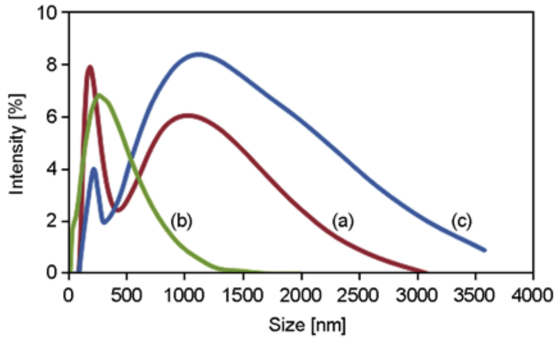

Figure 9. Particle size distributions of NRL (a); P(S-MAA) particle prepared by emulsifier-free emulsion polymerization (b) and NR/P(S-MAA) (c) prepared by heterocoagulation

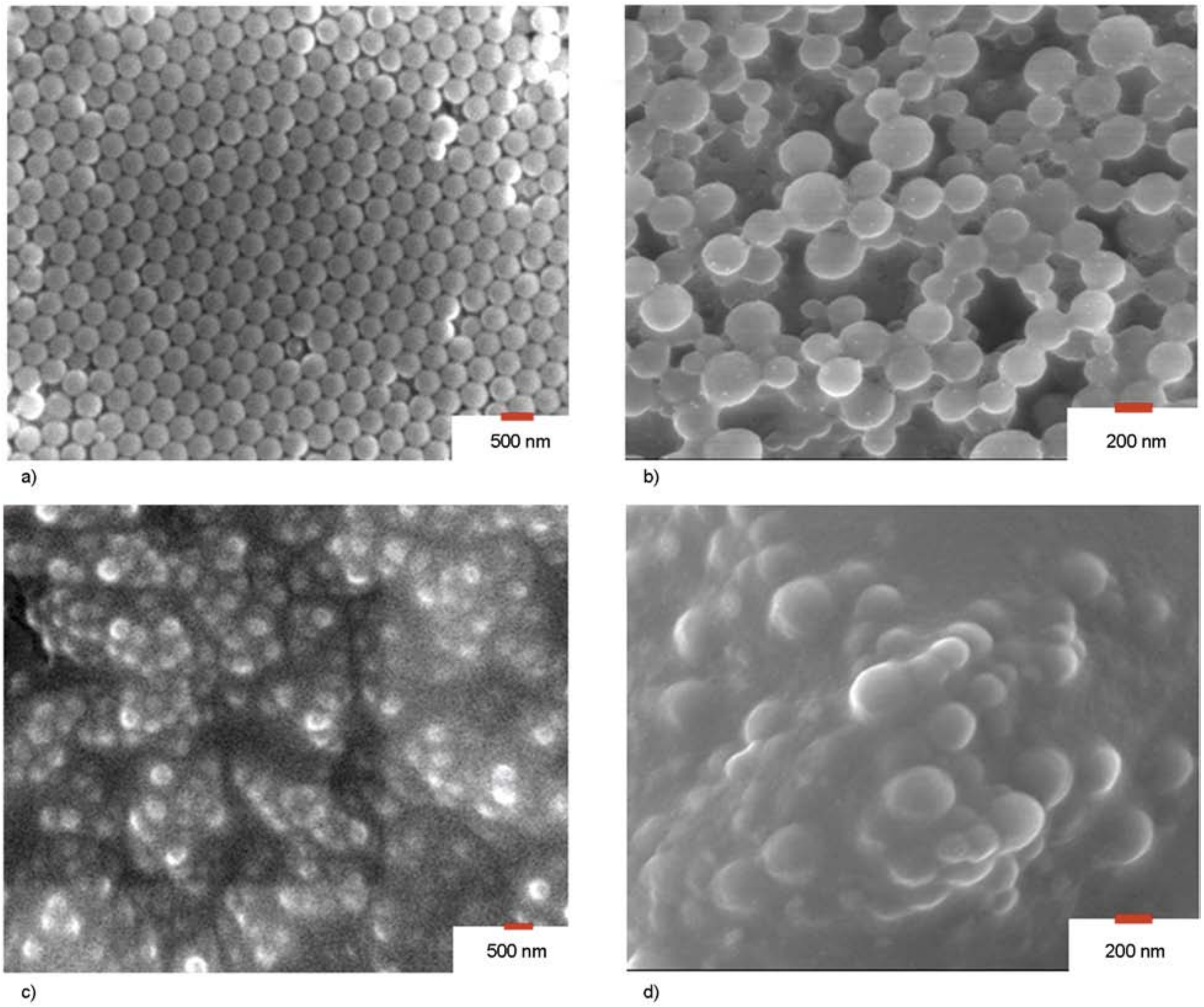

Figure 10. SEM micrographs of PS (a) and P(S-MAA) (b) particles prepared by emulsifier-free emulsion polymerization and NR/PS (c) and NR/P(S-MAA) (d) prepared by heterocoagulation

and 10d). This confirms that NR/PS and NR/P(S-MAA) nanocomposites were successfully prepared by heterocoagulation technique.

3.3. Mechanical properties of polymer nanocomposites

The mechanical properties of the polymer nanocomposites (NR/PS and NR/P(S-MAA)) were expectedly improved compared with the original NR according to the improvement of NR by incorporation of silica particles [3]. The mechanical properties of the composite films were shown in Table 2. NR film, the elastomeric polymer, shows good elasticity and flexibility as the elongation at break of 796% and low rigidity as the ultimate tensile strength and modulus of only 0.43 and 0.70 MPa, respectively. The ultimate tensile strength and modulus are greatly improved for NR/PS and NR/P(S-MAA) composite films which is affected by the reinforcement of the polymer nanoparticles. However, polymer nanoparticles reduced the film flexibility according to the reduction of their elongation at break because of the limitation in the polymer chain slipping beside the polymer nanoparticle surface. Therefore, for the applications, the amount of polymer nanoparticles should be varied in the heterocoagulation step corresponding to the appropriate mechanical properties.

Table 2. Mechanical properties of original NR, NR/PS and NR/P(S-MAA) composites

Samples	Ultimate tensile strenght [MPa]	Modulus [MPa]	Elongation at break [%]
NR	0.43	0.70	795.76
NR/PS	3.69	594.20	2.01
NR/P(S-MAA)	7.05	2553.91	0.57

4. Conclusions

The simple blending as heterocoagulation was successfully applied to produce polymer nanocomposite of NR/PS and NR/P(S-MAA). The polymers were mixed in the dispersed phase with controlling pH approximately 1 where the surface of NRL giving positive charge and negative charge of polymer nanoparticles surface. The adsorption of polymer nanoparticles on NRL surface took place via electrostatic interaction resulting in the formation of the composite polymer of NR/PS and NR/P(S-MAA). The mechanical properties of the polymer composites remarkably increase compared with the original NR affected from polymer nanoparticles filler. To improve the mechanical properties of polymer composite matched with the applications, it is easily handle by adding the appropriate amount of polymer nanoparticles.

Acknowledgements

This work was supported by The National Research Council, Thailand (No. 23666).

References

[1] Kawahara S., Kawazura T., Sawada T., Isono Y.: Preparation and characterization of natural rubber dispersed in nano-matrix. Polymer, **44**, 4527–4531 (2003). DOI: 10.1016/S0032-3861(03)00415-4

[2] Paiphansiri U., Tangboriboonrat P.: Prevulcanisation of skim latex: Morphology and its use in natural rubber based composite material. Colloid and Polymer Science, **284**, 251–257 (2005). DOI: 10.1007/s00396-005-1361-y

[3] Peng Z., Kong L. X., Li S-D., Chen Y., Huang M. F.: Self-assembled natural rubber/silica nanocomposites: Its preparation and characterization. Composites Science and Technology, **67**, 3130–3139 (2007). DOI: 10.1016/j.compscitech.2007.04.016

[4] Kurian J. K., Peethambaran N. R., Mary K. C., Kuriakose B.: Effect of vulcanization systems and antioxidants on discoloration and degradation of natural rubber latex thread under UV radiation. Journal of Applied Polymer Science, **78**, 304–310 (2000). DOI: 10.1002/1097-4628(20001010)78:2<304::AID-APP100>3.0.CO;2-G

[5] Abad L. V., Relleve L. S., Aranilla C. T., Aliganga A. K., San Diego C. M., dela Rosa A. M.: Natural antioxidants for radiation vulcanization of natural rubber latex. Polymer Degradation and Stability, **76**, 275–279 (2002). DOI: 10.1016/S0141-3910(02)00024-1

[6] Ho C. C., Kondo T., Muramatsu N., Ohshima H.: Surface structure of natural rubber latex particles from electrophoretic mobility data. Journal of Colloid and Interface Science, **178**, 442–445 (1996). DOI: 10.1006/jcis.1996.0139

[7] Busfield J. J. C., Deeprasertkul C., Thomas A. G.: The effect of liquids on the dynamic properties of carbon black filled natural rubber as a function of pre-strain. Polymer, **41**, 9219–9225 (2000). DOI: 10.1016/S0032-3861(00)00306-2

[8] Cai H-H., Li S-D., Tian G-R., Wang H-B., Wang J-H.: Reinforcement of natural rubber latex film by ultrafine calcium carbonate. Journal of Applied Polymer Science, **87**, 982–985 (2003). DOI: 10.1002/app.11410

[9] Arroyo M., López-Manchado M., Herrero B.: Organo-montmorillonite as substitute of carbon black in natural rubber compounds. Polymer, **44**, 2447–2453 (2003). DOI: 10.1016/S0032-3861(03)00090-9

[10] Teh P. L., Mohd Ishak Z. A., Hashim A. S., Karger-Kocsis J., Ishiaku U. S.: Effects of epoxidized natural rubber as a compatibilizer in melt compounded natural rubber–organoclay nanocomposites. European Polymer Journal, **40**, 2513–2521 (2004). DOI: 10.1016/j.eurpolymj.2004.06.025

[11] Lu Y-L., Ye F-Y., Mao L-X., Li Y., Zhang L-Q.: Microstructural evolution of rubber/clay nanocomposites with vulcanization process. Express Polymer Letters, **5**, 777–787 (2011). DOI: 10.3144/expresspolymlett.2011.76

[12] Varghese S., Karger-Kocsis J.: Natural rubber-based nanocomposites by latex compounding with layered silicates. Polymer, **44**, 4921–4927 (2003). DOI: 10.1016/S0032-3861(03)00480-4

[13] Magaraphan R., Thaijaroen W., Lim-ochakun R.: Structure and properties of natural rubber and modified montmorillonite nanocomposites. Rubber Chemistry and Technology, **76**, 406–418 (2003). DOI: 10.5254/1.3547751

[14] Nair K., Dufresne A.: Crab shell chitin whisker reinforced natural rubber nanocomposites. 2. Mechanical behavior. Biomacromolecules, **4**, 666–674 (2003). DOI: 10.1021/bm0201284

[15] Xu S. H., Gu J., Luo Y. F., Jia D. M.: Effects of partial replacement of silica with surface modified nanocrystalline cellulose on properties of natural rubber nanocomposites. Express Polymer Letters, **6**, 14–25 (2012). DOI: 10.3144/expresspolymlett.2012.3

[16] Teixeira R. F. A., Bon S. A. F.: Physical methods for the preparation of hybrid nanocomposite polymer latex particles. Advances in Polymer Science, **233**, 19–52 (2010). DOI: 10.1007/12_2010_65

[17] Han J., Kumacheva E.: Monodispersed silica–titanyl sulfate microspheres. Langmuir, **17**, 7912–7917 (2001). DOI: 10.1021/la010745y

[18] Fleming M. S., Mandal T. K., Walt D. R.: Nanosphere–microsphere assembly: Methods for core–shell materials preparation. Chemistry of Materials, **13**, 2210–2216 (2001).
DOI: 10.1021/cm010168z

[19] Taniguchi T., Ogawa T., Kamata Y., Kobaru S., Takeuchi N., Kohri M., Nakahira T., Wakiya T.: Preparation of core–shell coagulates by hydrophobic heterocoagulation of micron-sized poly(methyl methacrylate) and submicron-sized poly(styrene) particles. Colloids and Surfaces A: Physicochemical and Engineering Aspects, **356**, 169–175 (2010).
DOI: 10.1016/j.colsurfa.2010.01.015

[20] Okubo M., Lu Y., Wang Z.: Production of soft core/hard shell composite polymer particles by the stepwise heterocoagulation method with heat treatment. Colloid and Polymer Science, **276**, 833–837 (1998).
DOI: 10.1007/s003960050317

[21] Okubo M., Lu Y.: Estimation of surface morphology of composite polymer particles prepared by the stepwise heterocoagulation method with ζ-potential measurement. Colloid and Polymer Science, **276**, 282–285 (1998).
DOI: 10.1007/s003960050241

[22] Li G., Yang X., Wang J.: Raspberry-like polymer composite particles via electrostatic heterocoagulation. Colloids and Surfaces A: Physicochemical and Engineering Aspects, **322**, 192–198 (2008).
DOI: 10.1016/j.colsurfa.2008.03.006

[23] Kim J. S., Yun J. H., Kim I., Shim S. E.: Electrical properties of graphene/SBR nanocomposite prepared by latex heterocoagulation process at room temperature. Industrial and Engineering Chemistry, **17**, 325–330 (2011).
DOI: 10.1016/j.jiec.2011.02.034

[24] Sanguansap K., Suteewong T., Saendee P., Buranabunya U., Tangboriboonrat P.: Composite natural rubber based latex particles: A novel approach. Polymer, **46**, 1373–1378 (2005).
DOI: 10.1016/j.polymer.2004.11.074

[25] Okubo M., He Y., Ichikawa K.: Analysis of 'stepwise' heterocoagulation process of small cationic polymer particles onto large anionic polymer particles using dynamic light scattering. Colloid and Polymer Science, **269**, 125–130 (1991).
DOI: 10.1007/BF00660301

[26] Okubo M., Chaiyasat A., Yamada M., Suzuki T., Kobayashi H.: Influence of hydrophilic-lipophilic balance of nonionic emulsifiers on emulsion copolymerization of styrene and methacrylic acid. Colloid and Polymer Science, **285**, 1755–1761 (2007).
DOI: 10.1007/s00396-007-1770-1

[27] Chaiyasat A., Yamada M., Kobayashi H., Suzuki T., Okubo M.: Incorporation of nonionic emulsifiers inside styrene-methacrylic acid copolymer particles prepared by emulsion copolymerization. Polymer, **49**, 3042–3047 (2008).
DOI: 10.1016/j.polymer.2008.05.007